A study on the contributing factors to the surface radiation budget

Doctoral Thesis
博士論文

A study on the contributing factors to the surface radiation budget

地表面放射収支とその変動要因に関する研究

東北大学大学院理学研究科
地球物理学専攻

Kyohei YAMADA
山田　恭平

2015
平成 27 年

Acknowledgements

First, I would like to acknowledgements all the people who supported me during the course in Tohoku University.

I am grateful to Prof. T. Hayasaka for teaching me cloud-radiation problem and for many valuable discussions and enormous encouragements throughout the course for the graduate school. I thank to Prof. H. Iwabuchi for teaching me the radiative transfer calculation and operating computing. I appreciate Prof. M. Shiobara of the National Institute of Polar Research for valuable comments about polar research and encouragement to research in polar region. I would like to Dr. S. Katagiri for helpful comments on my study. I also appreciate to Prof. M. Sekiguchi for providing a radiative transfer code, "mstrnX" to calculate radiative transfer in plane-parallel atmosphere. Thanks are extended to Dr. M. Yoshioka of Nagoya University for teaching me the basis of reanalysis and model calculation and supplies. This thesis completed with the assistance by N. Takahashi.

Finally, special thanks are expressed to my parent, Kazuhiko and Masako Yamada, and all the friends of mine for their supports and hearty encouragement throughout my study in the graduate school.

Abstract

Surface downward radiation is important for understanding the climate change, energy budget, and water cycle at the Earth's surface. The present study estimates the contributions of cloud and the other environmental factors to the surface downward radiation at the various in-situ observatories. The inter-annual trends of downward radiation and the radiative contributions are also evaluated at six stations in mid-latitude and polar regions.

Target observatories are twelve stations belonging to the Baseline Surface Radiation Network, which was established to measure accurate in-situ measurement of radiative flux. Cloud existence is estimated by visual observation, lidar or ceilometer, humidity vertical profile of radiosonde observation, and satellite or reanalysis products. Contributions of cloud, water vapor, carbon dioxide, aerosol, and albedo to surface downward radiation are evaluated by the difference of radiative fluxes between observation and calculation.Individual contributions are evaluated by removing these factors one by one from the normal condition including all of the factors (removal method) and by removing all factors except for one particular factor (addition method). Radiative transfer calculation is performed with a plane-parallel two-stream radiative transfer model under clear-sky and overcast conditions. The clear-sky and overcast are classified by cloud fraction by visual observation and geometrical thickness of cloud estimated by radiosonde. When the geometrical thickness is enough large, the cloud is assumed to be optically thick in the calculation model. Vertical profiles of air temperature and concentration of water vapor are inserted by radiosonde observation. The other concentrations of gases are referred to the standard atmosphere profile. Only carbon dioxide concentration is corrected by the in-situ observation data. Aerosol optical depth and vertical distribution is obtained from reanalysis dataset and aerosol model. The result of calculation is good agreement with observed values both for longwave and shortwave radiation under clear-sky condition. Under overcast

condition, while calculated value of longwave corresponds to observation, calculation sometimes underestimates downward shortwave radiation.

Under clear-sky condition, contribution of water vapor by removal method is large both to longwave and shortwave by 60 to 71% and 3 to 29%, respectively. The longwave radiation has strong correlations with surface air temperature, humidity, and integrated amount of water vapor. Contribution of carbon dioxide to longwave radiation by removal method is 3 to 27% and not large except in polar region. Aerosol contributes to shortwave radiation from −4 to +24%, smaller than contribution of water vapor. Contribution of the surface albedo reaches −10%, and the large albedo on the snow or ice surface in polar region increases multiple-scattering up to 10% even if under clear-sky.

Under overcast condition, contribution of cloud to downward longwave radiation shows strong correlation with the difference of temperatures between cloud base height and the surface. Some day under overcast condition indicates larger 100% or smaller 0% contributions by becoming larger downward longwave radiation by removal cloud than normal condition. One of the reasons of larger 100% or smaller 0 % radiative contribution is error of observation and model parameters. The other reasons of exceed 100% or negative contribution is temperature inversion layer. In polar region, the larger 100% or smaller 0% contribution appear frequently.

Under all-sky condition, contribution of cloud to longwave radiation ranges from -2 to +28 % and generally shows negative correlation with cloud base height, however it shows large variability and it is more affected by cloud amount and amount of water vapor. Cloud fraction is a dominant factor of contribution of cloud to shortwave radiation under all-sky, and the contribution of cloud ranges from -5 to +85%. Under all-sky condition, cloud radiative contribution to the total radiative flux at the surface ranges from -71 to +27 %. Cooling effect is superior in sub-tropic and mid-latitude regions, while warming effect is superior in desert and polar regions.

To evaluate climate changes of recent decade, the inter-annual changes of radiation and the contributions of environmental factors are evaluated in mid-latitude and polar regions. The mid-latitude regions show no significant

trend for the surface downward longwave radiation on the annual means, but the surface downward shortwave radiation increases and the trend satisfy with 95 % confidence level in the eastern Asia station. The increasing trend of the surface downward shortwave radiation is caused by decreasing low or middle cloud mainly for spring season. In the European continental regions, the low or middle cloud fraction decreases for spring or autumn seasons, and the downward shortwave radiation increases.

In polar regions, Arctic coastal area shows significantly increasing the downward longwave radiation, which is caused by the increasing surface air temperature and precipitable water with 95 % confidence level. Low-middle cloud fraction in the Arctic area decreases as well as the mid-latitude regions, while variation of water vapor under dry condition in polar region makes much larger increasing the downward longwave radiation than mid-latitude. The two stations in Antarctica show different trends of radiation and cloud. Longwave radiation in George von Neumayer show decreasing trend, but total cloud fraction increases. The decreasing of longwave radiation is caused by decreasing of low and middle cloud fraction for winter season. Syowa station, which is located at east of George von Neumayer, shows different trend of total cloud fraction and cloud base height because of the circulation change. An increasing trend of the surface downward longwave radiation in summer season at Syowa, Antarctic coastal area is +6.75 Wm^{-2}/decade and very large. Because of small change of total cloud fraction and a very large increasing rate of precipitable water by +0.31 mm/decade, it is considered that the large increase in the surface downward longwave radiation for summer season is caused by the increasing amount of water vapor due to the humid wind from sea. The effect of humid wind for summer does not appear in Georg von Neumayer, which is also located at Antarctic coastal area. The surface downward shortwave radiation shows only slightly trend both in the Arctic and Antarctica on the annual means even if low or middle cloud fraction shows decreasing trend with 95 % confidence level. Low or middle cloud mainly show trend from autumn to spring season, and the long nighttime reduces an impact of cloud on the surface downward shortwave

radiation. In mid-latitude region, the surface downward shortwave radiation increases caused by a decreasing of cloud.

Contents

Chapter 1

Introduction

1.1 Global radiation budget

The Earth's surface energy budget is determined by the shortwave radiation emitted by the sun and longwave radiation emitted by the atmosphere and the Earth's surface. Downward radiation is important for climate change, the water cycle, and global warming because of the effect of the radiation on the surface energy budget.

Earth's atmosphere is opaque to longwave radiation. The atmosphere absorbs upward longwave radiation emitted from the surface and emits longwave radiation, which keeps the surface warm. This is called the greenhouse effect. Downward longwave radiation (L_D) is mainly controlled by water vapor (WV), air temperature, and cloud. WV has a large effect on L_D and the contribution is larger than 90% below 1000 m. Yamamoto and Sasamori (1954) investigated L_D in Sendai, Japan, and showed that up to 80% of L_D is emitted from WV below 900 hPa at night under clear-sky conditions. Philipona et al. (2004) showed that the 39% of L_D is emitted from WV below 10 m under clear-sky conditions. Perturbations of near-surface atmospheric conditions and cloud affect longwave radiation compared with the global average. Henderson et al. (2013) estimated the effects of the perturbations of air temperature, humidity, and cloud base height. When air temperature and humidity under 500 hPa vary by ±2 K and 25%, L_D changes by ±4 and ±9 W m^{-2}, respectively. Perturbations of cloud base height by ±240 m affect the surface L_D by ±1.5 W m^{-2}. Carbon dioxide (CO_2) is an important greenhouse gas (GHG) because of its long lifetime in the atmosphere. CO_2 is increasing because of anthropogenic activities such as burning fossil fuels and changing land use. The present amount of CO_2 in the atmosphere is approximately 1.4 times larger than that before the industrial revolution.

The mean rate of increase was 1.4 ppm/year from 1960 to 2005, and the rate increased to 1.9 ppm/year on average from 1995 to 2005 (IPCC, 2007; Solomon et al., 2007).

Wild et al. (2013) combined satellite observations with the energy balanced and filled dataset (Loeb et al., 2012), which contains a large number of in situ surface observations from the Global Energy Balance Archive (GEBA; Gilgen et al., 1998; Ohmura et al., 1989), and the Baseline Surface Radiation Network (BSRN; Ohmura et al., 1998) as the best estimate of the radiation budget for the Intergovernmental Panel on Climate Change 5th assessment report. The global means of surface L_D and downward shortwave radiation (S_D) are 342 and 185 W m^{-2}, respectively. The estimated L_D is larger than the previous studies by 10 to 20 W m^{-2} (Kiehl and Trenberth. 1997; Trenberth et al., 2009). Zhang et al. (2004) estimated the global mean L_D of 345 W m^{-2} by using the International Satellite Cloud Climatology Project (ISCCP)-FD product. They compared the ISCCP-FD product with the observed surface value from BSRN and found a small mean bias of 2.2 W m^{-2}. The value is in good agreement with Wild et al. (2013). It was proposed that the surface L_D estimation was improved by combining the latest calculation model and the updated surface observational record.

Wang and Liang (2009) parameterized the surface L_D under all-sky conditions for 1973 to 2008 at 3200 observatories with the method reported by Brunt (1932) and by Crawford and Duchon (1999) by using surface air temperature, WV pressure, and incident shortwave radiation. The accuracy of the method was checked by comparing the results with values observed at 36 sites. They showed that the surface L_D increases by 2.2 W m^{-2}/decade. Prata (2008) evaluated the rate of increase of L_D with the monthly means of air temperature and WV profiles at 136 locations of the National Center for Atmospheric Research. Without considering the effect of cloud, the calculation results from MODTRAN-3 (Berk et al., 1996) showed that the increase in L_D is obtained from 20 and 52 sites with confidence levels of 99% and 95%, respectively. The rate of increase was +1.67 W m^{-2}/decade compared with the global average. The equator region showed a larger increase than the mid-latitude and polar regions. To evaluate the rate of

increase of L_D from observations, Wild et al. (2008) collected data from 12 BSRN sites for 1992 to 2000 and estimated the rate of increase as 2.6 W m^{-2}/decade.

The earth atmosphere is mainly transparent to shortwave radiation, although WV, aerosols, and cloud affect S_D. Gilgen et al. (1998) estimated the trend in the surface S_D by using the observed value of GEBA on the monthly mean and they found a significant negative trend of 2%/decade in Africa, Asia, Europe, and North America. A significant positive trend was found in small regions only. Hatzianastassiou et al. (2005) evaluated the increase of S_D at the surface for 17 years (1984 to 2000) on the monthly average, based on the radiative transfer calculation with 2.5° resolution. The input data was long-term climatological data from the International Satellite Cloud Climatology Project (ISCCP-D2). In contrast to Gilgen et al. (1998), the S_D showed a significant increasing trend of 2.4 W m^{-2}/decade from 1984 to 2000.

These studies are about the global average and are not related to the air temperature, amount of WV, and variation of GHGs, aerosols, and surface albedo at the in situ observatories. Cloud, one of the important factors to affect the surface radiation budget, has large variability. To evaluate the climate change, an investigation of cloud and its effects is essential.

1.2 Polar regions

In polar regions, because of the low temperature, small amount of WV, and strong inversion layer, the absorption band in the atmosphere related to the radiation is different from wet, hot regions. Although the amount of WV is small in polar regions, the effect of WV on L_D is dominant. Town et al. (2005) evaluated the contributions of WV and CO_2 to L_D at the South Pole for 2000. Under clear-sky conditions, 2/3 and 1/3 of L_D were attributed to WV and CO_2, respectively. In the Arctic, more than 92% of precipitable water is contained below 5000 m (Raddartz et al., 2013). Ishida et al. (1998) analyzed microwave radiometer, radiosonde, and L_D data from Inuvik (68.32°N, 133.50°W) and Kiruna (67.88°N, 20.25°E). They pointed out the importance

of the effect of vertical variation of air temperature and WV on L_D. Doyle et al. (2011) investigated an increase in the effect of WV on L_D at Eureka, Ellesmere Island (80°N, 86°W) from 9 to 11 February 2010. The inversion intensity showed a linear relationship with net longwave radiation (Yamanouchi & Kawaguchi, 1984). Raddartz et al. (2013) reported the correlation between the increase of WV with height caused by the temperature inversion and the inversion intensity by observing the vertical distribution of WV with microwave radiometer in Arctic, the southeastern Beaufor Sea-Amundsen Gulf. The WV inversion has a large effect on L_D; however, observing the concentration of near-surface WV is difficult by satellite retrieval, especially under cloudy conditions.

Clouds play an important role in the Arctic climate system. Intrieri et al. (2002a) evaluated the cloud effect on the surface radiation budget by using Surface Heat Budget of the Arctic Ocean (SHEBA) data from November 1997 to October 1998. They estimated that the annual mean effects of Arctic cloud are -10, +38, and -6 W m^{-2} on the shortwave radiation, longwave radiation, and heat budget, respectively. Clouds generally warmed the surface, except for in late summer and early autumn. Dong et al. (2010) estimated the 10-year climatology of the cloud fraction in the Arctic, and they showed that cloud fraction increased substantially in spring and decreased in winter. Intrieri et al. (2002b) investigated cloud in the Arctic by using SHEBA lidar and radar data. In the Arctic, the cloud frequencies are large in summer and small in winter. Cloud base height does not show seasonal variation. The number of cloud layers is generally 1–2, and multiple clouds appear frequently in summer. Over a year, 73% of the cloud contains water. The frequency of water clouds reaches a maximum of 95% in July and a minimum of 25% in December.

The surface warming in the Arctic is greater than the global average and this is an important region for climate change. However, only the Antarctic Peninsula shows clear warming of +0.5 K/decade in Antarctica. Air temperature in eastern Antarctica has not increased over the last 50 years according to records from 19 stations since the 1950s (Turner et al., 2005). However, Steig et al. (2009) investigated the air temperature change in the

Antarctic and they reported the warming of the Eastern Antarctic. The sea ice loss in Arctic in 2007 of -22% compared with 2005 is unprecedented. Kay et al. (2008) investigated the Arctic sea ice and concluded that the minimum sea ice extent is correlated with the small amount of cloud fraction and large shortwave radiation.

An important change in the Antarctic climate is the strengthening of the circumpolar westerly called the Southern Hemisphere annular mode (SAM; Thompson and Solomon, 2002; Gillett and Thompson, 2003), which is caused by stratospheric ozone depletion. The ozone hole over Antarctica strengthens the stratospheric polar vortex in spring, causing the stratospheric vortex to descend. The westerly flow streaming from the relatively warm waters west of the Drake Passage caused by SAM contributes to the surface warming over the Antarctic Peninsula and Patagonia.

High snow albedo and the low temperature of the surface make satellite retrieval difficult over the polar regions. Long-term polar night causes large uncertainty in the amount of cloud measured by visual observations. Therefore, information about the surface radiation budget and the variation of cloud in polar regions is insufficient, despite the importance of surface warming, melting snow, and circulation change.

1.3 Unsolved problems and objectives

To estimate the radiative contributions of WV and other factors quantitatively, Kiehl and Trenberth (1997) evaluated single forcing factors in satellite data by removing each factor from normal climate conditions. However, they estimated the radiative contribution for outgoing longwave radiation only because of difficulties in retrieving the surface downward radiation from satellite observations owing to uncertainties in the vertical cloud profile. Schmidt et al. (2010) applied the version of GISS ModelE used for the Fourth Assessment Report of the IPCC to calculate the contribution of a single factor to upwelling radiation by removing or adding the factor. However, these results were calculated for the global average.

Understanding of the variability of the factors affecting the surface downward radiation is limited, especially for the variation in vertical distribution with site or season.

Radiative flux observation has a long history. However, the comparison of the data observed in situ is not sufficient, especially in the polar regions. Some previous studies used different methods, instruments, and periods. Despite the importance of studying the polar region for global warming, information about cloud and its contribution to radiation is insufficient.

In this study, we estimate the contributions of cloud and the other environmental factors to L_D and S_D at various stations quantitatively. We also evaluate the inter-annual trends of L_D, S_D, and the contributions and compare the trends in polar and mid-latitude regions. In Chapter 2, surface measurement, satellite retrieval, and reanalysis product data are described, and the error of the in situ surface radiative flux observations is discussed. Methods for estimating the contribution of cloud, WV, CO_2, aerosols, and albedo are shown in this chapter. In Chapter 3 we discuss the contributions of atmospheric factors to the surface downward radiation for twelve observatories with hourly averages under clear-sky, overcast, and all-sky conditions. Chapter 4 presents the inter-annual variation of cloud and surface downward radiation, and the contributions of atmospheric factors to the radiation in mid-latitude and polar regions, which have observation periods longer than ten years. The summary of the study is presented in Chapter 5.

Chapter 2

Data and Analysis

In this chapter, we describe the datasets, observation instruments, instrument accuracies, and radiative transfer models.

2.1 Dataset

2.1.1 BSRN

The Baseline Surface Radiation Network (BSRN; http://www.bsrn.awi.de/; Ohmura et al., 1998) by the World Climate Research Program (WCRP) is an in situ observation network for high-quality, high-accuracy, long-term surface radiation budget studies. The BSRN stations are located to avoid the heat-island effect and air pollution. The WCRP recommends that observatories are located within 50 km of the weather station. The basic measurement programs, which are conducted at all BSRN stations, include observations of downward longwave radiation (L_D), downward shortwave radiation (S_D), and direct and diffuse shortwave radiation. BSRN aims to achieve radiative flux observations with an error of less than 10 W m^{-2} or 5% (McArthur, 2005). The basic measurement program has a frequency of 1 Hz and the 1-min averages are archived.

Data used in this study are mainly collected at 12 stations belonging to BSRN. We used surface downward radiation, vertical temperature, and relative humidity profiles from radiosonde observations, and the corresponding meteorological observation data. Table 2.1 provides descriptions and mean climate parameters of the observation stations. Figure 2.1 shows the locations of the target stations. Ishigaki Island (ISH), Japan is the hottest, wettest target station. The annual averages of the

surface air temperature (T_S) and precipitable water (PW) are 297 K and 43 mm, respectively. The annual average L_D and S_D are 404 and 177 W m^{-2}, respectively. The South Pole Observatory (SPO) in Antarctica is the coldest, driest station. The annual averages of T_S, PW, L_D, and S_D are 224 K, 0.3 mm, 113 W m^{-2}, and 129 W m^{-2}, respectively. We categorize stations into four types by annual mean PW and T_S. The sub-tropic region is defined as having a PW greater than 25 mm, and includes Fukuoka (FUA), Bermuda (BER), and ISH. The mid-latitude region has PW of 10 to 25 mm, which includes Payerne (PAY), Lindenberg (LIN), Sapporo (SAP), and Tateno (TAT). The desert region has PW less than 10 mm and T_S larger than 280 K, and includes Tamanrasset (TAM). The polar region has PW of less than 10 mm and T_S lower than 280 K, and Ny-Ålesund (NYA), Syowa (SYO), and SPO are in the polar region.

BSRN observation data are separated into subsets. We use 0100 basic observation data (L_D, S_D, direct shortwave radiation, and diffuse shortwave

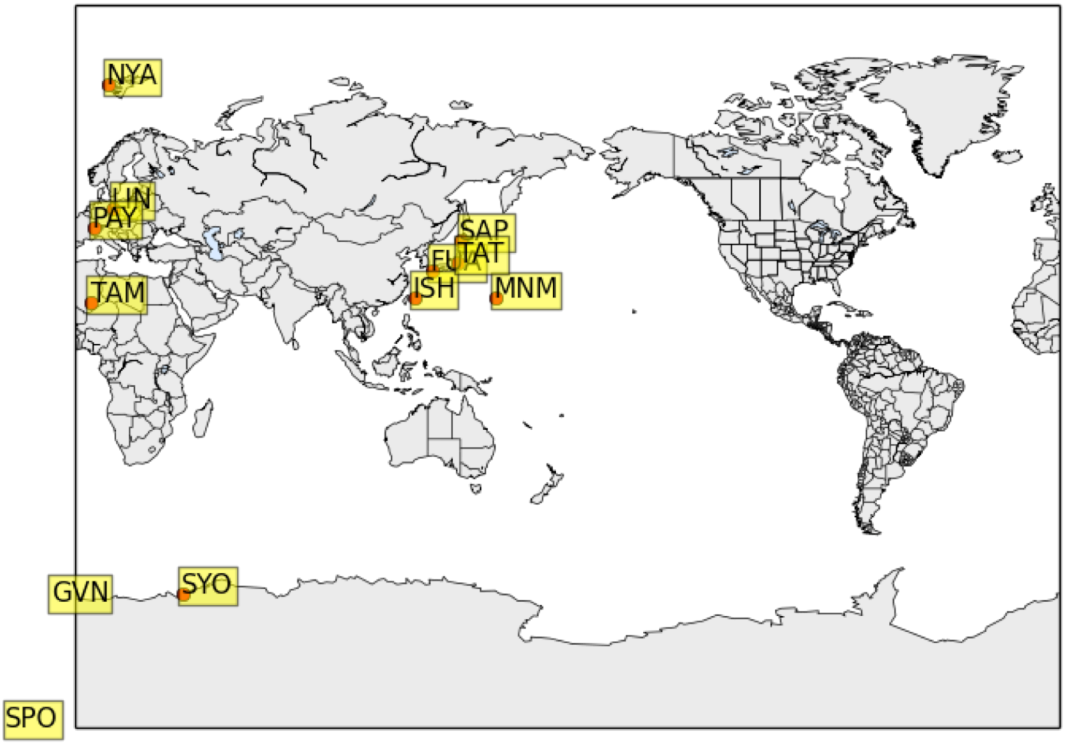

Figure 2.1. Locations of BSRN observation sites.

radiation), 1000 meteorological data (T_S, surface humidity, cloud fraction by visual observation, wind speed, and wind direction), and 1100 radiosonde data (vertical distributions of air temperature and relative humidity). The instruments are described in Section 2.2.

Table 2.1. Descriptions and annual mean climate parameters of BSRN observation sites.

Station	Abbr.	Area	Lat. [°E]	Lon. [°N]	Alt. [m]	L_D [W m^{-2}]	S_D [W m^{-2}]	T_S [K]	PW [mm]	Period
Ishigakijima	ISH	Japan	24.34	124.16	6	403.4	176.9	297.5	42.9	2010-2014
Minamitorishima	MNM	Minami-Torishima	24.29	153.98	7	398.9	221.7	298.6	38.9	2010-2014
Fukuoka	FUA	Japan	33.58	130.38	3	350.4	154.0	290.4	25.0	2010-2014
Tamanrasset	TAM	Algeria	22.79	5.53	1385	328.2	268.9	296.1	5.8(*1)	2008-2014
Tateno	TAT	Japan	36.05	140.13	25	337.6	160.2	287.4	24.4	1997-2014
Sapporo	SAP	Japan	43.06	141.33	17	311.5	144.1	282.5	16.3	2010-2014
Lindenberg	LIN	Germany	52.21	14.12	125	311.0	124.5	282.5	14.9	1994-2007
Payerne	PAY	Switzerland	46.82	6.94	491	315.0	142.1	282.8	14.8	1996-2007
Ny-Ålesand	NYA	Ny-Ålesund, Spitsbergen	78.93	11.93	11	254.3	76.8	268.7	6.3	1994-2014
Syowa	SYO	Cosmonaut Sea	-69.01	39.59	18	218.9	127.6	262.6	3.1	1998-2013
Georg von Neumayer	GVN	Dronning Maud Land, Antarctica	-70.65	-8.25	42	218.5	126.1	257.1	3.0	1992-2014
South Pole	SPO	Antarctica	-89.98	-24.80	2800	113.0	129.0	223.8	0.3	2005-2006 2010-2014

2.1.2 Mooring buoys

Mooring buoys are useful for observing the surface radiative budget at the sea surface. The Kuroshio Extension Observatory (KEO), National Oceanographic and Atmospheric Administration (NOAA; Cronin et al., 2008) and Japan Kuroshio Extension Observatory, JAMSTEC (JKEO; Kubota et al., 2008) are normally moored at 32.4°N, 144.6°E, and 37.9°N, 146.6°E, respectively (Figure 2.2).

The mooring buoy is the second generation of the Autonomous Temperature Line Acquisition System (ATLAS), which has improved data quality, temporal resolution, and cost compared with the previous system. ATLAS observes L_D and S_D at the sea surface with Eppley Precision Infrared Radiometer (PIR) and Precision Spectral Pyranometer (PSP) radiometers,

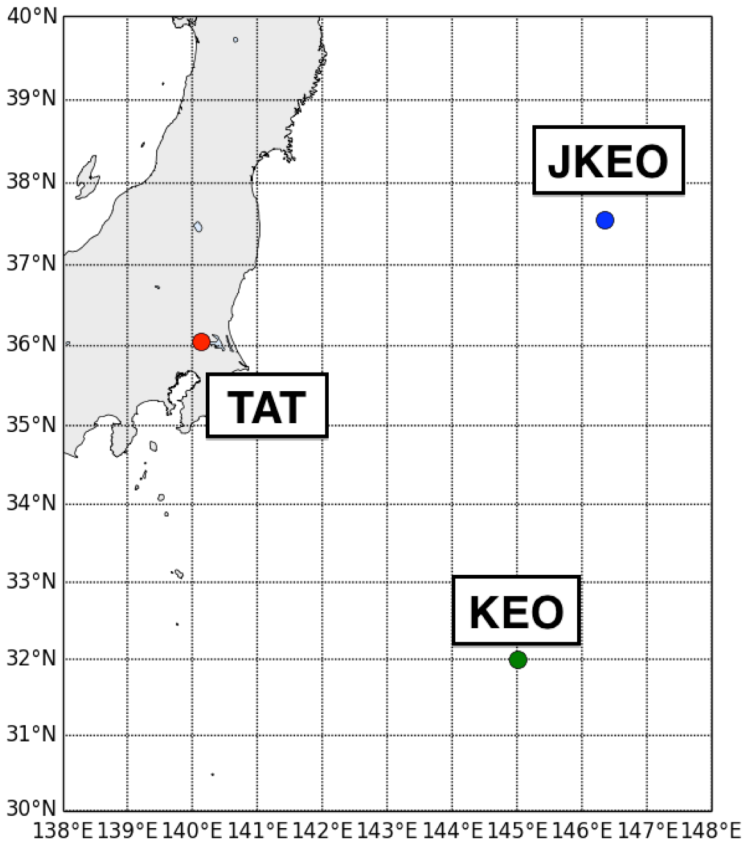

Figure 2.2. Locations of KEO and JKEO.

respectively. These radiometers are optimized for observations at the marine-surface and are resistant to corrosion. The optimized radiometers have a smaller error range than conventional instruments and a higher accuracy for laboratory measurements. However, the accuracies of the radiometers do not consider the effects of environmental factors. The optimized radiometers do not have ventilation systems or shading from direct solar radiation, which would assist maintaining a stable dome temperature. The radiometers are described in Section 2.2. The ATLAS system also observes meteorological parameters, such as wind speed and precipitation levels. Wind speed is determined with Gill Windsonic (ultrasonic) and Visalia WXT 520 (sonic wind speed) devices, and rainfall is measured with RM Young 50203-34 and Vaisala WXT520 devices.

2.1.3 Atmospheric data in Japan

In Japan, some observatories have been recording radiosonde, weather, and cloud fraction measurements for longer than 50 years. The data that are more than 50 years old are archived in the Aerological Data in Japan (ADJ) provided by the Japan Meteorological Agency (JMA).

To evaluate the long-term trend in downward radiation in Japan, we used the ADJ data at TAT, which is the same as the BSRN station. To consider the effect of the upper atmospheric temperature, the integrated air temperature (IAT [hPa K]) is defined by Eq. (2.1) in the same way as PW, as

$$IAT = \sum_{i=0:\,Surface}^{TOA-1} \frac{T_i - T_{i+1}}{2}(P_{A,i} - P_{A,i+1}), \tag{2.1}$$

where T_i and $P_{A,i}$ are air temperature and air pressure in layer i, respectively. Unlike relative humidity, the air temperature in the troposphere and stratosphere does not reach zero. IAT increases with the radiosonde altitude. Therefore, IAT is suitable as an indicator of upper air temperature, if the temperature is integrated from the surface to the radiosonde altitude. Thus, *TOA* in Eq. (2.1) is the uppermost altitude where

the radiosonde cannot detect relative humidity.

2.1.4 Satellite retrieval

Satellites are useful for monitoring the geographical variation of radiative fluxes, cloud microphysics, and surface conditions. In this study, we use satellite data mainly to compare the surface radiative fluxes and cloud with in situ observations. Table 2.2 shows general information related to the satellite retrievals.

The FD-SRF data product of the International Satellite Cloud Climatology Project (ISCCP; Rossow and Zhang 1995; Zhang et al., 2004) is a product of radiative flux profiles, calculated using cloud, surface properties, and climatology products of the ISCCP D1 dataset. The climatology products of temperature and gases are provided by the Television and Infrared Observation Satellite Operational Vertical Sounder (TOVS) product, the Total Ozone Mapping Spectrometer product, and the National Centers for Environmental Prediction of the first reanalysis product. Cloud particle size climatology is provided by Han et al. (1995; 1999). Aerosol climatology is

Table 2.2. Descriptions of satellite retrievals.

Satellite	ISCCP	MODIS		MTSAT-1R	CloudSat-CALIPSO
Products	FD-SRF	L2 Joint Atmosphere	L3 Daily Global	CEReS gridded data	2B-GEOPROF-LIDAR
Spatial Resolution	2.5° (280 km equal-grid)	5 km at nadir	1°	0.04°	1km for along track 0.3km for across track below 8.2km
Temporal Resolution	3h	10:30/13:30 local time	Daily	1h	10:30/13:30 local time
Target	All-sky L_D & S_D Clear-sky L_D & S_D Cloud mask	Clear-sky L_D & S_D Cloud mask	Cloud mask	Cloud mask	Cloud mask

provided by the Stratospheric Aerosol and Gas Experiment-II and the Goddard Institute for Space Studies (GISS) climate model. The climatology of surface type, albedo, spectral dependence, and infrared emissivity are provided by the GISS climate model. The ISCCP-D series datasets are better than the old ISCCP-C series datasets, particularly for ice clouds. Compared with surface radiative flux measurements, ISCCP FD-SRF products showed biases of less than 10 W m^{-2} for longwave and shortwave monthly averages. FD-SRF shows good correlation with observations in the Northern Hemisphere, but poor correlation in the Southern Hemisphere because of the small land area and number of observatories.

The Moderate Resolution Imaging Spectroradiometer (MODIS) level 2 Joint Atmosphere product contains vertical air temperature and humidity profiles at 20 pressure levels with 5-km spatial resolution at the nadir. The data are retrieved at 10:30 and 13:30 local time from the Terra and Aqua satellites, respectively. The air temperature and humidity profiles are retrieved by using algorithms adapted from the International TOVS Processing Package (ITPP) using MODIS channels 25, 27 to 29, and 30 to 36. We use vertical profile data from the MODIS L2 Joint Atmosphere product near in situ observations around 0.1° to calculate L_D and S_D. Because the MODIS retrieval is instantaneous at 10:30 and 13:30 local time, MODIS L2 retrieval is not used for daytime averages. In this study, we calculated MODIS L2 and a two-stream radiative transfer model, mstrnX (Sekiguchi and Nakajima, 2008) under only clear-sky conditions, defined as conditions in which the cloud mask is 0.0.

MODIS level 3 daily global data contains surface statistical datasets derived from the level 2 dataset. The spatial resolution is a 1° equal-angle grid cell. The data is used for comparing cloud fraction with the other satellite retrieval and in situ observation methods.

The Multi-functional Transport Satellite 1R (MTSAT-1R) is operated by the JMA and the Japan Civil Aviation Bureau of the Ministry of Land, Infrastructure and Transport. MTSAT-1R is a geosynchronous orbit at 140°E. It provides five spectral bands of radiance data over the Asia–Pacific region. The visible and IR data of MTSAT 1R is revised by JMA, the Weather

News, the Biohybrid System Laboratory of Tokyo University, and published by the Center for Environmental Remote Sensing Chiba University (CEReS). In the present study, MTSAT-1R data are used for cloud detection to compare clear-sky surface downward radiation over the land and buoy observatories in Section 2.3.3. "Clear-sky" estimated by MTSAT-1R refers to conditions satisfying all of the following requirements. 1) The difference between the brightness temperature of the IR1 channel (11 μm) and the IR2 channel (12 μm) is smaller than 2 K. 2) IR1 is higher than −20 °C. 3) Surface albedo, as estimated by using a visible wavelength (0.73 μm), is smaller than 10% only over buoy observatories. 4) Cloud fraction, estimated by visual observations by the JMA, is 0 okta only for observatories in Japan. Requirements 2)–4) mainly target low clouds, which show high albedo and are optically thick. Requirement 1) targets high clouds using the split-window method (Inoue, 1987). If the conditions do not satisfy the requirements, the cloud mask is estimated as the probability of clouds. Cloud mask estimation by MTSAT-1R is not performed at night. The frequency of missing clouds calculated by using the combined method is determined as less than 5% from comparison with the MODIS level 2 Joint Atmosphere product. Misses are probably caused by differences in temporal resolution between MTSAT-1R and MODIS L2. The combined method is sufficient for identifying completely clear-sky conditions; therefore, we use this method in Section 2.3.3.

CloudSat and CALIPSO are satellites with active sensors, Cloud Profiling Radar with a 94 GHz microwave sensor and Cloud-Aerosol Lidar with Orthogonal Polarization (CALIPSO) with wavelengths of 532 and 1064 nm. These active sensors, unlike passive sensors such as MODIS or MTSAT-1R, emit electromagnetic waves and retrieve the vertical profiles and optical properties of objects by measuring the backscatter. Because of the difference in wavelength between radar and lidar, the targets are different. Radar detects thick cloud, although the wavelength is too long to retrieve aerosols and optical thin cloud with small particles. In contrast, lidar detects small particles and thin cloud, but optically thick cloud prevents the laser from penetrating the atmosphere below the cloud (Winker

et al., 2010). The present study uses cloud base height (CBH) and frequency of cloud existence as cloud fraction from the 2B-GEOPROF-LIDAR product (Mace et al., 2009). For comparison with in situ observations and the other satellite, the cloud fraction and CBH retrieved by CloudSat and CALIPSO are used in the average of all data within 1° from the target observatory.

2.1.5 Reanalysis products

Reanalysis products provide long-term and global physical quantities. In this study, the reanalysis product is used to obtain aerosol optical depth (AOD) for radiative transfer calculations and for comparing the surface radiative flux at the sea surface with the other estimation methods. Table 2.3 shows the descriptions of the reanalysis products.

The Monitoring Atmospheric Composition and Climate (MACC) of the European Centre for Medium-Range Weather Forecast (ECMWF) is the European Union's Global Monitoring of Environment and Security program and an atmospheric chemical composition dataset with 1.125° resolution (Inness et al., 2013). Sources and sinks of trace gases are supplied by the chemical transport models coupled with the Integrated Forecast System by using the OASIS4 coupler (Redker et al., 2010). The MACC produces the total AOD for 550 nm of the atmospheric daily temporal resolution. The AOD forecasts for MACC show good agreement with observations for the total

Table 2.3. Descriptions of reanalysis products.

Reanalysis	JRA55	ECMWF
Products	fcst_phy2m125	MACC
Spatial Resolution	1.25°	1.125°
Temporal Resolution	3h	Monthly
Target	All-sky L_D & S_D Clear-sky L_D & S_D	Aerosol Optical Depth

column, although there are discrepancies in the boundary layer values.

The Japanese 55-year Reanalysis Project (JRA55) is a 55-year global atmospheric reanalysis product run by JMA. JRA55 is an improved version of the JRA-25 reanalysis product (Onogi et al., 2007; Ebita et al., 2011). JRA products have been used for numerical assimilation and forecast systems in Asia by JMA. The major data sources are JMA meteorological archives, ERA-40 observational data supplied by ECMWF, and level 1c TOVS and ATOVS radiance temperature data. The JRA-55 fcst_phy2m125 dataset contains two-dimensional diagnostic forecast values for radiative flux. There are 37 layers from 1000 to 1 hPa. The basic framework for computing radiative flux follows Sugi et al. (1990), which considers prognostic WV, three-dimensional daily ozone, CO_2, and oxygen as active gases. The concentration and optical properties of aerosols are continental and maritime background values are without seasonal variation. The effective radius of cloud particles provided for the cloud scheme is fixed at 15 μm for liquid and 20 to 150 μm for ice. Comparing upper air temperatures with radiosonde observations at 18 Japanese stations shows that the JRA product has a large negative bias above 100 hPa. The present study targets the surface radiative flux and the effect of upper air is negligible.

2.2 Surface observation

2.2.1 Pyranometers and pyrgeometers

Radiometers are a basic instrument for estimating the surface radiative fluxes and have a long history. Radiometer observations contain errors of 3 to 4 W m^{-2} for L_D (Philipona et al., 2001; Marty et al., 2003), and 3% to 5% for S_D, although the error can be reduced to 5 W m^{-2} or 2% by using periods longer than 1 day (Michalsky et al., 1999). BSRN aims to obtain high-accuracy, high-temporal resolution, and high-quality data. We consider that the surface observation data in BSRN stations are usually reliable. The instrument errors caused by rain, low temperatures, and the sea-surface are described in Section 2.3.

The surface S_D is estimated by pyranometers for global or diffuse radiation, and by pyrheliometers for direct radiation. Stations and periods for pyranometer data are shown in Table 2.4 and for pyrheliometer data in Table 2.5. Tables 2.6 and 2.7 show the pyranometer and pyrheliometer properties, respectively. Recent pyranometers and pyrheliometers use a thermopile sensor to output electromotive force proportional to the incident shortwave radiation.

S_D contains direct solar radiation. Therefore, the incident angle of the solar radiation affects the pyranometer error (the cosine effect). The error caused by the cosine effect depends on the pyranometer properties and generally becomes large at a large solar zenith angle (SZA) (Nast, 1983). For example, the cosine error of the Eppley PSP is a ±1% deviation from the ideal value from 0° to 70° and ±3% from 70° to 80°. The cosine errors of CM21 and CM22 (Kipp & Zonen) are ±2% and ±1% at a SZA of 60° and ±6% and ±3% at SZA of 80°, respectively. Because of the cosine effect, the pyranometer is unreliable at SZA larger than 80°. Therefore, the radiative contributions of cloud and the other factors to S_D are not calculated with SZA larger than 80° in Chapter 3 and 4.

Some stations do not collect visual observations of cloud amount. To evaluate cloud amount without visual observations, we use the shortwave diffusivity index (SDI; Long and Ackerman, 2000) in Chapter 3. SDI is defined as

$$SDI = \frac{DIF}{DIR \times \mu + DIF}, \tag{2.2}$$

where μ is the cosine of SZA. DIR and DIF are direct and diffuse shortwave radiation, respectively. We use only daytime data to estimate the SDI.

Table 2.4. Data periods of the pyranometers.

Site	Instrument	Period
ISH	CMP-21, Kipp&Zonen	2010-2014
	CMP-22, Kipp&Zonen	2010-2014
MNM	CMP-21, Kipp&Zonen	2010-2014
	CMP-22, Kipp&Zonen	2010-2014
FUA	CMP-21, Kipp&Zonen	2010-2014
	CMP-22, Kipp&Zonen	2010-2014
TAM	PSP, Kipp&Zonen	2000-2014
TAT	MS-801, EKO	1996-1997
	CM-21, Kipp&Zonen	1996-2010
	CM-22, Kipp&Zonen	2003-2011
	CMP-21, Kipp&Zonen	2011-2014
	CMP-22, Kipp&Zonen	2011-2014
SAP	CMP-21, Kipp&Zonen	2010-2014
	CMP-22, Kipp&Zonen	2010-2014
LIN	CM-22, Kipp&Zonen	2003-2007
	CM-21, Kipp&Zonen	1994-2003
PAY	CM-21, Kipp&Zonen	1992-2011
	CM-22, Kipp&Zonen	2006-2011
NYA	CM-11, Kipp&Zonen	1992-2010
	CM-22, Kipp&Zonen	2011-2014
	CMP-22, Kipp&Zonen	2014-2014
SYO	MS-801, EKO	1998-1999
	CM-21, Kipp&Zonen	1998-2013
GVN	CM-11, Kipp&Zonen	1992-2009
	CM-22, Kipp&Zonen	2009-2012
	CMP-22, Kipp&Zonen	2011-2013
SPO	PSP, Eppley	1992-2014

Table 2.5. Data periods of the pyrheliometers.

Site	Instrument	Period
ISH	CHP-1, Kipp&Zonen	2010-2014
MNM	CH-1, Kipp&Zonen	2010-2011 2012-2013
	CHP-1, Kipp&Zonen	2010-2014
FUA	CHP-1, Kipp&Zonen	2010-2014
TAM	NIP, Eppley	2000-2014
TAT	CH-1, Kipp&Zonen	1996-2011
	CHP-1, Kipp&Zonen	2011-2014
SAP	CHP-1, Kipp&Zonen	2010-2014
LIN	CH-1, Kipp&Zonen	1998-2007
PAY	CH-1, Kipp&Zonen	2002-2011
	NIP, Kipp&Zonen	1993-2001
NYA	CHP-1, Kipp&Zonen	2011-2013
	NIP, Eppley	1992-2011
SYO	CH-1, Kipp&Zonen	2001-2013
	CHP-1, Kipp&Zonen	2011-2013
GVN	CHP-1, Kipp&Zonen	2010-2013
	NIP, Eppley	1992-2009
SPO	NIP, Eppley	1992-2014

Table 2.6. Pyranometer properties.

Developer	Kipp&Zonen			Eppley	EKO
Instrument	CM-11	CM-21 CMP-21	CM-22 CMP-22	PSP	MS-801
Wavelength [nm]	285-2800	285-2800	200-3600	295-2800	300-3000
Sensitivity [$\mu V/Wm^{-2}$]	7-14	7-14	7-14	~8	~7
Response Speed [sec]	5 (95%)	5 (95%)	5 (95%)	5 (95%)	2.5 (1/e)
Temperature Dependency [%]	<1 (-10 to +40℃)	<1 (-20 to +50℃)	<0.5 (-20 to +50℃)	0.5 (-30 to +50℃)	~1 (-20 to +40℃)
Environmental Temperature [℃]	-40 to +80	-40 to +80	-40 to +80	-50 to +80	-40 to +80(*1)

(*1). For MS-802, the next generation of MS-801. Environmental temperature of MS-801 is nonpublic information.

Table 2.7. Pyrheliometer properties.

Developer	Kipp&Zonen	Eppley
Instrument	CH-1 CHP-1	NIP
Wavelength [nm]	280-4000	200-4000
Sensitivity [$\mu V/Wm^{-2}$]	7-14	~8
Response Speed [sec]	5 (95%)	1 (1/e)
Temperature Dependency [%]	±0.5 (-20 to +50℃)	±1 (-20 to +40℃)
Environmental Temperature [℃]	-40 to +80	-20 to +40℃

L_D is observed with the CG-4, CGR-4 (Kipp & Zonen), and PIR (Eppley) pyrgeometers. Table 2.8 shows the data period for the pyrgeometers. FUA, ISH, SAP, and Minamitori Island (MNM), Japan, use CG-4 or CGR-4 pyrgeometers; TAM, PAY, NYA, Georg von Neumayer Station (GVN), and SPO use PIR pyrgeometers; and TAT, LIN, and SYO use both types. Performance differs between PIR and CG-4 (or CGR-4) pyrgeometers in terms of properties such as wavelength range. Payne (2004) compared these two types of pyrgeometers for 9 months in 2002 in Massachusetts. They found that the difference in L_D measurements was less than 5 W m^{-2} in the 1-min average over the observation period. In the present study, L_D observations from PIR pyrgeometers are not distinguished from those from CG-4 or CGR-4 pyrgeometers. To reduce the effects of small perturbations and instrumental error, radiation data is used with an average longer than hourly.

Table 2.8. Period of Pyrgeometer.

Site	Instrument	Period
ISH	CGR-4, Kipp&Zonen	2010-2014
MNM	CGR-4, Kipp&Zonen	2010-2014
FUA	CGR-4, Kipp&Zonen	2010-2014
TAM	PIR, Eppley	2000-2014
TAT	PIR, Eppley	1996-2007
	CGR-4, Kipp&Zonen	2008-2014
SAP	CGR-4, Kipp&Zonen	2010-2014
LIN	CG-4, Kipp&Zonen	2005-2005
	PIR, Eppley	1994-2005 2006-2007
PAY	PIR, Eppley	1992-2011
NYA	PIR, Eppley	1992-2014
SYO	PIR, Eppley	1998-2000
	CG-4, Kipp&Zonen	2001-2013
GVN	PIR, Eppley	1992-2013
SPO	PIR, Eppley	1993-2014

Table 2.9. Characteristics of pyrgeometer

Developer	Kipp&Zonen	Eppley
Instrument	CG-4 CGR-4	PIR
Wavelength [μm]	4.5 to 42	4 ~ 50
Sensitivity [μV/W/m^2]	~10 5 to 10	~5
Response speed [sec]	6 (63%]	2 (1/e)
Temperature Dependency [%]	<1	<1
Environmental Temperature [℃]	-40 ~ +80	-20 ~ +40

Pyrgeometers measure longwave radiation by absorbing the radiative flux transmitted through the dome, which reflects shortwave radiation. The absorbed longwave radiation produces a temperature difference between the top and bottom of the thermopile and produces a voltage, which is proportional to the difference in fluxes entering and emitted by the photosensitive area. By subtracting the net longwave radiation from the upward longwave radiation emitted from the photosensitive area, the pyrgeometer estimates the longwave radiation. If the dome of the pyrgeometer absorbs shortwave radiation rather than reflecting it, the secondary radiation from the dome causes a measurement error called window heating offset. To reduce the error, some pyrgeometers measure the temperature of the dome and correct the data by using the difference in temperature between the dome and thermopile. The thermopile of CG4 and CGR4 pyrgeometers connects to the dome and reduces the window heating error to less than 4 W m^{-2} (Kipp & Zonen, 2006). Table 2.9 shows the description of pyrgeometers used in the target BSRN stations.

2.2.2 Radiosonde

Radiosonde is a valuable instrument for observing vertical structures of temperature and humidity in the troposphere and the inside of clouds. Because some stations have radiosonde observation periods longer than 10 years, the radiosonde estimation method for CBH and geometrical thickness is used to evaluate the inter-annual variation of cloud and the effect. Wang and Rossow (1995) estimated the CBH and cloud top heights with radiosonde observations by using the following criteria. 1) From the surface to the top, the base of the lowest moist layer is detected as the level that has either relative humidity (RH) ≥ 87% or RH ≥ 84% that increases ≥3% from the lower level or the surface level. 2) The next levels above the base are temporarily assumed to be inside the moist layer if RH ≥ 84% until reaching a level with RH below 84% or reaching the top of the profile. 3) The levels within the moist layer are tested from the highest level down to the base. The top of the moist layer is detected as the level where either RH ≥ 87% or RH ≥ 84% and

RH increases ≥3% from the higher level or the top level of profile. 4) If the top of the layer is found in 3), the moist layer is a cloud layer. In the method reported by Wang and Rossow (1995), RH is calculated with respect to water at all temperatures; however, in this study, we calculate RH with respect to ice at temperatures below −20 °C. From 0 to −20 °C, RH is calculated with respect to mixing water and ice.

Table 2.10. Data periods of the radiosondes.

Site	Instrument	Period
ISH	RS-06, Meisei	2010-2014
MNM	RS-01, Meisei	2010-2012
	RS-06, Meisei	2012-2013
	RS-11G, Meisei	2013-2014
FUA	RS92, Vaisala	2010-2013
	RS11G, Meisei	2013-2014
TAM	RS92, Vaisala	2007-2014
TAT	No Information	
SAP	RS92, Vaisala	2010-2013
	RS11G, Meisei	2013-2014
LIN	No information	
PAY	SRSCH, Meteolabor AG	1996-2011
NYA	No information	
SYO	RS280, Meisei	1994
	RS291, Meisei	1994-2007
	RS01, Meisei	2008-2013
	RS06, Meisei	2013-2013
GVN	No information	
SPO	Unknown manufacture	1992-2014

The air temperature sensor is affected by solar heating or heat cooling (Gaffen, 1994). The radiosonde measurements have been improved by reducing the heating and cooling errors with correction algorithms, changes in instrument shape, and advances in materials. These improvements may make long-term analysis difficult and detect small changes in climate. The present study considers these factors resulting from improved instrumentation, although the data are treated with no correction. Table 2.10 shows the data periods for the radiosondes at the target BSRN stations.

2.2.3 Synoptic observations

BSRN records the ground-based surface meteorological data with the synoptic observations (SYNOP). The visually observed cloud fraction ranges from 0 (clear sky) to 8 oktas (overcast) in this study; no measurements of 9 oktas (sky obscured) are used. The visually observed cloud fraction is converted to values from 0 to 1.

Some stations report cloud fraction divided into total (CF_{Total}) and low-middle cloud ($CF_{Low\text{-}Middle}$). The low, middle, and high heights for visual observation are normally 0 to 6500 ft, 6500 to 20,000 ft, and above 20,000 ft, respectively (Grant, 1944). These ranges are guides rather than absolute values. To compare visual observation of $CF_{Low\text{-}Middle}$ with the other estimation methods, altitudes of low and middle cloud are defined as from 0 to 2 km (approximately 6500 ft) and 2 to 6 km (approximately 20,000 ft), respectively.

Weather conditions are classified by the SYNOP visual report and cloud fraction in Chapter 3. Clear-sky conditions are defined as a cloud fraction by visual observation of 0, whereas overcast conditions are defined as CF_{Total} of 1 and no rain, which indicates the present weather code of SYNOP is smaller than 30. All-sky conditions with no precipitation are defined as conditions with a weather code equal to or larger than 30, to prevent the rain droplet error in pyrgeometers, as discussed in Section 2.3.3.

2.2.4 Lidar and ceilometer

Lidar and ceilometers are active remote sensors that emit laser pulses and detect backscattered radiation. These instruments are used to observe CBH. The cloud fraction estimated by lidar and ceilometer is the frequency of cloud detection. Of the 12 BSRN stations, GVN and LIN have a ceilometer made by Vaisala that observes CBH. Ceilometers in GVN were LD-WHX, LD-CL31, and LD-CL51 ceilometers from January 1995 to January 2009, February 2009 to December 2010, and since January 2011, respectively. LD-WHX with a wavelength of 911 nm is an old type of ceilometer and the range is limited to 3600 m (Kupfer et al., 2006). LD-CL31 and CL51 are the successors to LD-WHX. LD-CL31 and CL51 have a detection range of 8 to 13,000 m, although their operation period is insufficient. In this study, CBH measured by lidar at GVN is used for only LD-WHX, which cannot detect high cloud, for long-term observation periods. The model name of the ceilometers at LIN is not recorded from January 1996 to May 2003; therefore, CBH for this period is unreliable. Only the Vaisala LD-40 ceilometer at LIN is used for June 2003 to February 2007. The wavelength of LD-40 is 855 nm, the temporal resolution is 15 s, and the spatial resolution is 8 m. The ceiling range is between 8 and 13,000 m with a measurement deviation of ±23 m (for solid objects).

The National Institute for Environmental Studies (NIES) has Mie lidars, two of which are located near the SAP (NIES lidar at 43.1°N, 141.3°E) and TAT (NIES lidar at 36.05°N, 140.12°E) BSRN stations. Because the locations are close to the BSRN stations, we use the Mie lidar data as the observations from SAP and TAT. The Mie lidar observes the attenuated backscattering coefficient (ABC) with 532 and 1064 nm wavelength lasers every 15 min. CBH is estimated from the 1064 nm wavelength signal (Shimizu et al., 2010). CBH is estimated as the height at which the increase of ABC for 1064 nm is larger than 4×108 sr^{-1} m^{-1}. The vertical resolution of the ABC is originally 6 m, whereas the vertical resolution of CBH is 30 m because five data segments are averaged to improve the signal-to-noise ratio. In the low atmosphere, the small ratio of overlap between backscattering light and the field of view (FOV) of the telescope makes the accuracy of cloud detection

unreliable. Thus, the Mie lidar does not provide CBH below an altitude of 120 m.

NIES Mie lidars observe every 15 min; the cycle is 5 min of observation and 10 min of break. The ABC, β', is defined by Eq. (2.3) as

$$\beta'(r) = \beta(r) \times \exp(-2\tau), \tag{2.3}$$

where $\beta(r)$ is the atmosphere volume backscattering coefficient at distance r, and τ is the optical depth at distance r defined by Eq. (2.4) as

$$\tau = \int_0^r \sigma(R) dR, \tag{2.4}$$

where $\sigma(r)$ is the atmospheric volume extinction coefficient.

The lidar equation for Mie scattering is expressed in Eq. (2.5) as

$$P(r) = \frac{C_L P_{in,li} \Delta r}{r^2} \times \beta(r) \times exp\left\{-2 \int_0^r \sigma(R) dR\right\}, \tag{2.5}$$

where $P(r)$ is the receiving signal intensity in range r, C_L is a lidar calibration coefficient, $P_{in,li}$ is the emission signal intensity, and Δr is the vertical distribution. If these parameters are written as C, the ABC can be expressed in Eq. (2.6) by the distance and receiving signal intensity as

$$\beta'(r) = \frac{P(r) \times r^2}{C}. \tag{2.6}$$

CBH is evaluated by using the 1064 nm signal. CBH is the altitude, at which the rate of increase of the ABC is larger than 4×10^8 sr^{-1} m^{-1} and the ABC above CBH must exceed 5×10^8 sr^{-1} m^{-1} (Shimizu et al., 2010).

Micro pulse lidar (MPL) is an eye-safe, low-cost lidar that uses microjoule pulse energies of 523 nm from a diode-pumped Nd:YLF laser. The technique was developed in the National Aeronautics and Space

Administration (NASA) Goddard Space Flight Center (GSFC) (Spinhirne, 1993). MPLNET is a worldwide network of MPL run by NASA/GSFC. In this study, we use data from MPLNET at NYA and SYO. These MPLs are designed by Science & Engineering Service Inc., USA (Lee et al., 1997). The observation is operated with WMPL software. WMPL's method of estimating CBH is based on empirically determined factors. The National Institute of Polar Research promotes atmospheric research and runs an MPL system at the French and German Arctic research bases (the German Alfred Wegener Institute for Polar and Marine Research, and the French Polar Institute Paul Emile Victor) at NYA (Shiobara et al., 2006). In Antarctica, SYO has an MPL system. Data are averaged for 1 min and 30 m range resolutions.

CBH is estimated by a threshold-based detection algorithm (Welton and Campbell, 2002; Campbell et al., 2002; Campbell et al., 2008). Equation (2.7) gives the raw MPL count rate as

$$P_{raw}(r) = \frac{CEO(r)[\beta_M(r)+\beta_P(r)]T_M^2(r)T_P^2(r)}{D(P_{raw})r^2} + \frac{A_{raw}(r,E)}{D(P_{raw})} + \frac{B_{raw}}{D(P_{raw})}, \quad (2.7)$$

where $P_{raw}(r)$ is the measured signal per shot at range r, C is a calibration value, E is the pulse energy (μJ), $O(r)$ is the overlap function, $D(P_{raw})$ is the detector dead time factor, $A(r, E)$ is the detector after-pulse per shot, B is the solar background signal per one short, and β_M and β_P are the backscatter cross-section terms. $T^2_M(r)$ and $T^2_P(r)$ are the transmission terms given by Eq. (2.8) as

$$T_i^2(r) = \exp\left[-2\int_0^r \sigma_i(r')dr'\right], \quad (2.8)$$

where $\sigma(r)$ is the extinction coefficient, and subscript i denotes either a molecular or particle quantity. The signal resulting from the correction process is called the normalized relative backscatter (NRB; unit: photoelectrons km^{-2} μs^{-1} μJ) signal and is defined as Eq. (2.9) as

$$P_{NRB}(r) = C[\beta_M(r) + \beta_P(r)]T_M^2(r)T_P^2(r). \quad (2.9)$$

The level 1.0 MPLNET contains the NRB product, and CBH is estimated by the NRB vertical profile.

2.2.5 All-sky imager

All-sky imager observation is used to record cloud conditions similar to visual observation. Among the BSRN polar stations, NYA and SYO have all-sky imagers, PSV-100 (PREDE). The FOV is 160° and the images are recorded in 8-bit JPEG format. In this study, we use the Yabuki method (Yabuki et al., 2014). The Yabuki method classifies each pixel (averaged 3 × 3) of an image as clear-sky, optically thick cloud, optically thin cloud, and no classification. If SZA is larger than 85°, the picture is not classified. The Yabuki method compares the pixels of the target image and the clear-sky image that has the same SZA as the target image. The clear-sky picture is called the virtual clear-sky image.

The Yabuki method algorithm is described in Figure 2.3. R_1, G_1, and B_1 are the red, green, and blue intensities of the target image, respectively. R_2, G_2, and B_2 are red, green, and blue intensities of the virtual clear-sky image, respectively. 1) A pixel with an image zenith angle smaller than 70° is not classified. 2) If [($B_1 > \delta_1$) and ($B_2 < \delta_2$) and ($|1 - B_1/B_2| < \delta_3$) and ($|1 - G_1/G_2| < \delta_4$) and ($B_1/R_1 > \delta_5$)], the pixel is clear-sky. 3) If [(SZA < 70°) and ($B_1 < \delta_1$)] or [($B_1/R_1 < \delta_6$) and ($|1 - R_1/R_2| > 0.1$ or $|1 - G_1/G_2| > 0.1$ or $|1 - B_1/B_2| > 0.1$)], the pixel is optically thick cloud. 4) If [($B_1/R_1 < \delta_7$) and ($1.03 \times B_1/R_1 < B_2/R_2$) and ($1.03 \times G_1/R_1 < G_2/R_2$)] or [($STD(R_1)/R_1 > 0.06$) and ($STD(G_1)/G_1 > 0.06$) and ($STD(B_1)/B_1 > 0.06$)], the pixel is optically thin cloud. 5) Otherwise, the pixel is clear sky. δ_1 to δ_7 are criteria that depend on the station (Table 2.11). $STD(R_1)$, $STD(G_1)$, and $STD(B_1)$ are the standard deviations of 3 × 3 pixels. In this study, virtual clear-sky images are selected by MPL and visual classification.

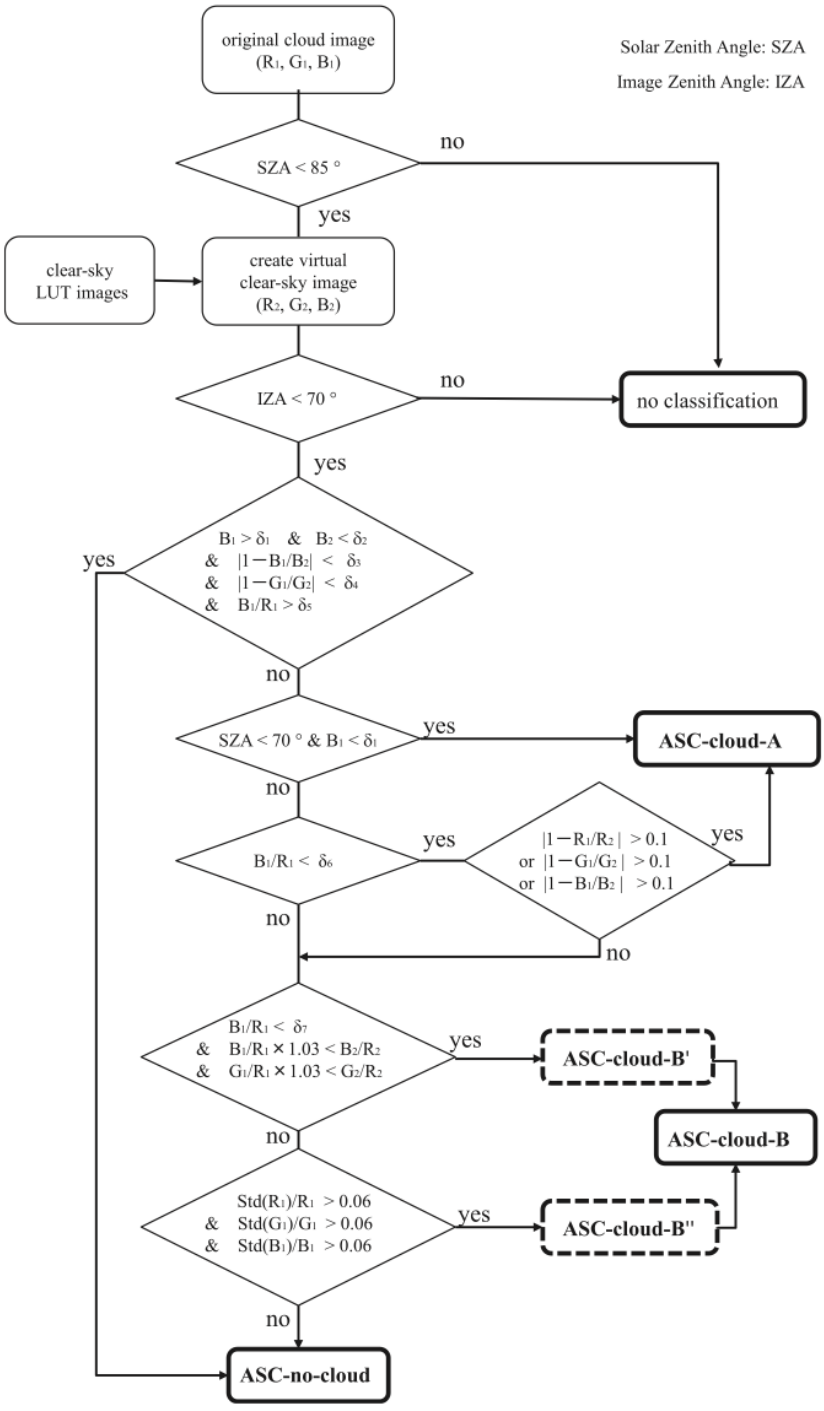

Figure 2.3. Flowchart of Yabuki's method (from Yabuki et al., 2014).

Table 2.11. Cloud detection threshold values at NYA and SYO (from Yabuki et al., 2014).		
Criteria	NYA	SYO
δ1	50	50
δ2	190	190
δ3	0.08	0.08
δ4	0.07	0.08
δ5	2.20	2.00
δ6	1.35	1.35
δ7	1.80	1.80

2.3 Accuracy of surface radiative flux observation

2.3.1 Error caused by rain

Because of the large absorption band, droplets attached to the dome make the pyrgeometer overestimate the amount of longwave radiation. To estimate the range of the overestimation, we compared L_D observed by a CG4 pyrgeometer in rain and with artificial rain applied with a spray gun under overcast conditions. After spraying, the water droplets on the dome were wiped off immediately. The experiments were conducted on the rooftop of Tohoku University, Japan (38.257°N, 140.839°E) from 11:15 to 11:30 and 11:45 to 12:00 on November 11, 2011; from 11:10 to 11:30 and 11:40 to 12:00 on November 30, 2011; and from 15:25 to 15:40 on December 21, 2012 local time.

Figures 2.4 and 2.5 show the minutely mean L_D and S_D, respectively, from 11:00 to 13:00 on November 11, 2011. L_D with artificial rain was larger than that without rain by approximately 15 to 20 W m^{-2}. However, S_D with artificial rain was the same as that with no rain. S_D decreased immediately after the rain was wiped off the dome.

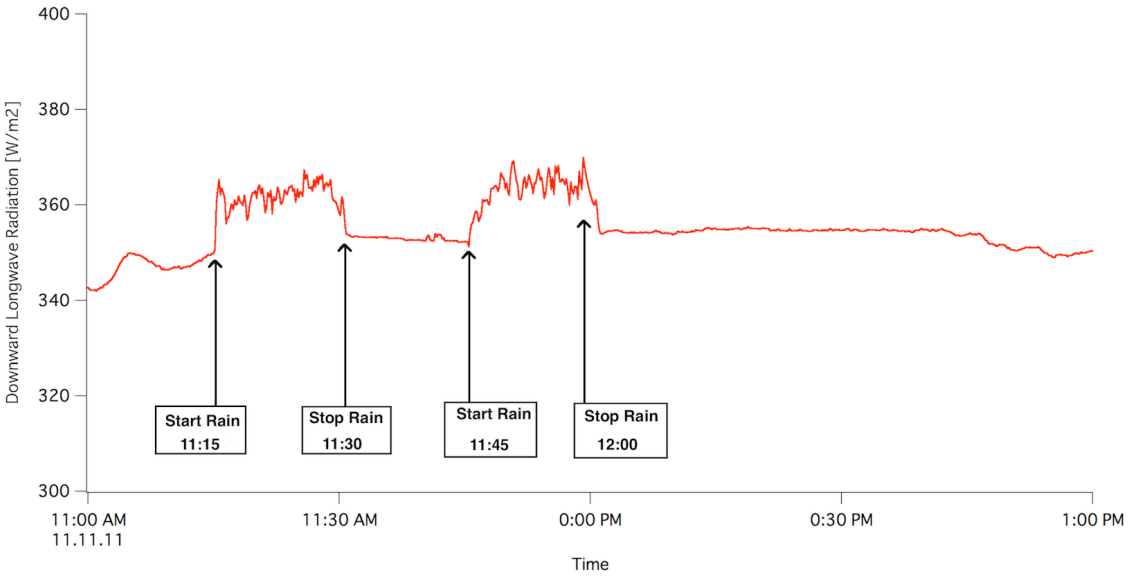

Figure. 2.4. L_D estimated by CG4 at Tohoku University from 11:00 to 13:00 (local time) at November 11, 2011. Artificial rain was applied from 11:15 to 11:30 and from 11:45 to 12:00.

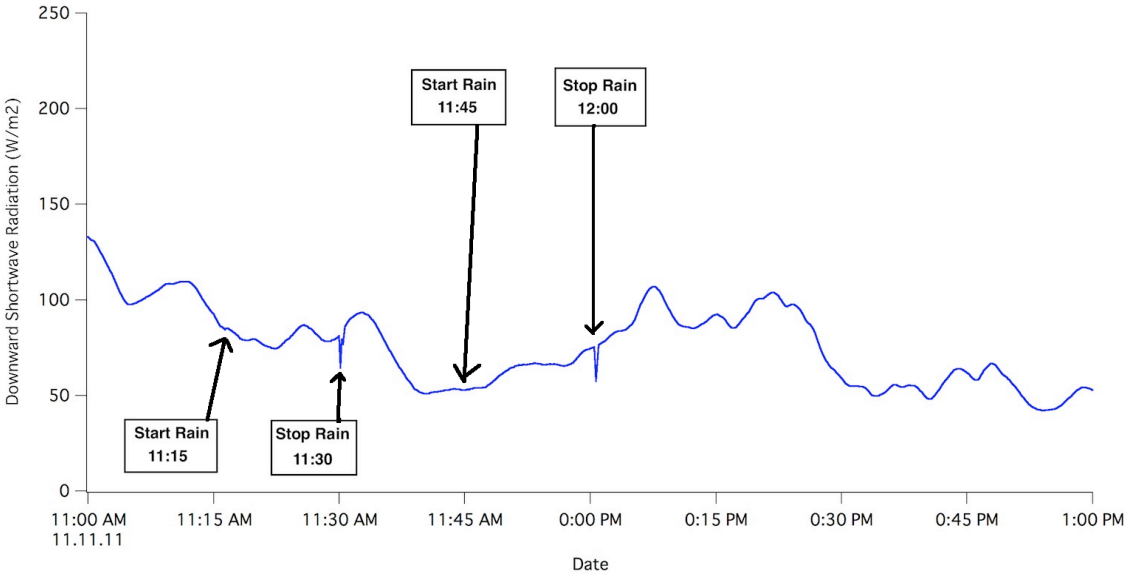

Figure. 2.5. S_D estimated by CMP22 at Tohoku University from 11:00 to 13:00 (local time) at November 11th, 2011. Artificial rain was applied from 11:15 to 11:30 and from 11:45 to 12:00.

2.3.2 Error caused by low temperature

Pyranometers and pyrgeometers provide accurate measurements with a small error range. However, the accuracy is guaranteed for only a temperature range from −20 to +50 °C.

Su et al. (2008) tested the dependences of the pyranometer and pyrgeometer on temperature. The pyranometer (CM21/22 pyranometer by Kipp & Zonen) and pyrgeometer (CG4 pyrgeometer by Kipp & Zonen) errors varied positively and negatively, respectively, with decreasing body temperature below −20 °C. The low-temperature error ranged from 4% to 6% for the pyranometer and was approximately 13% for the pyrgeometer at −60 °C (Figure 2.6). Air temperatures in polar regions (NYA, GVN, SYO, and SPO) are frequently below −20 °C, and the archive data may contain the low-temperature instrumental errors. The error should be corrected, although the sensor error under low-temperature conditions differs depending on sensors, and it is difficult to correct the error. Therefore, BSRN archived data are not corrected owing to low-temperature errors.

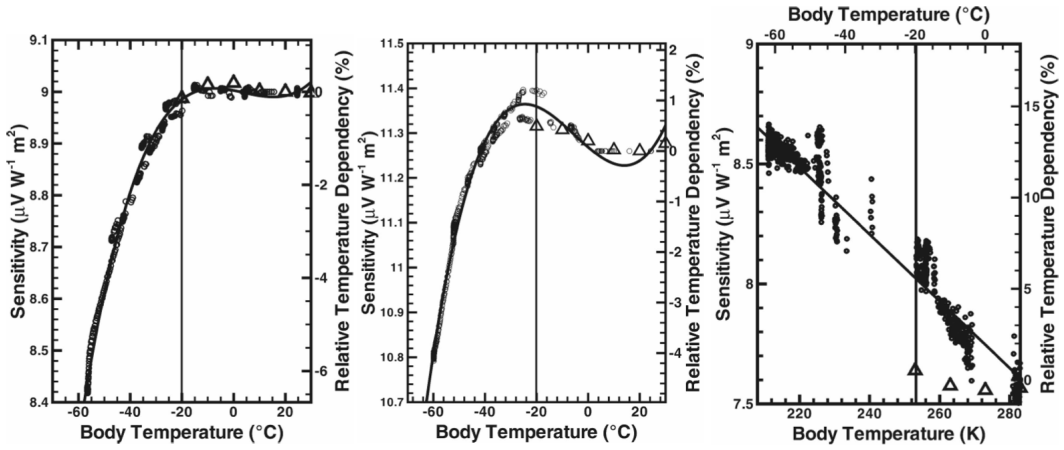

Figure. 2.6. Sensitivity changes of CM22 (left), CM21 pyranometers (middle), and CG4 pyrgeometer (right) with low body temperature (from Su et al., 2008).

2.3.3 Error on the sea surface

Mooring buoys are useful observatories for measuring the surface radiation in the ocean. The radiometers on buoys are optimized for sea surface observation, although the radiometer data contains observational errors caused by environmental factors (Yamada and Hayasaka, 2016). In this section, the radiometer errors on the sea surface are evaluated by comparing buoy and land observatories.

Pinker et al. (2009) compared the surface S_D obtained from satellite, buoy, and land observations. The satellite S_D was the MODIS level 3 product from 2003 to 2005. The buoy S_D was obtained from the Prediction and Research Moored Array in the Atlantic, Tropical Atmosphere Ocean project (TAO), and Triangle Trans-Ocean Buoy Network (TRITON). Land surface data were obtained from 18 BSRN observations. The biases and root mean square errors (RMSEs) for shortwave tropical Atlantic and tropical Pacific Ocean observations were calculated from the daily averages as 3 ± 25 and 1 ± 36 W m^{-2}, respectively. The bias and RMSE between land surface and MODIS was -3 ± 21 W m^{-2}. The biases and RMSE for ocean and land were similar. Niu et al. (2010) compared S_D from daily averages with estimated values from MODIS by using the method reported by Wang and Pinker (2009) for observed values from the KEO, JKEO, CLIVAR Mode Water Dynamic Experiment (CLIMODE) buoys, and the Pacific Marine Environmental Laboratory's mooring buoy (PAPA). The biases of KEO, JKEO, CLIMODE, and PAPA were −2.4, 4.5, 7.3, and −6.8 W m^{-2}, respectively. The RMSEs were 38.1, 29.6, 29.6, and 22.8 W m^{-2}, respectively. Kawai and Kawamura (2005) validated the estimation of S_D from the Geostationary Meteorological Satellite-5, and compared it with buoy and vessel observations. S_D derived from the satellite was calculated by using a parameterization method, and assumed a linear relationship between cloud absorption and cloud albedo (Tanahashi et al., 2001). The bias in the estimation from sea-surface observations was less than ±5 W m^{-2}, and the RMSE was ±11%–14% for daily average values.

Wang and Dickinson (2013) compared L_D obtained by ground-based, reanalysis and satellite retrieval methods. The 24 tropical marine buoys of

TAO and TRITON showed a positive bias for monthly averages compared with satellite retrievals and reanalysis by 3 to 4 W m^{-2}. They concluded that the reason for the positive bias was a lack of ventilation and shading from direct solar radiation. Alados-Arboledas et al. (1988) studied the effect of no ventilation or shading of buoy systems. The effect reached 30% to 40% under clear-sky conditions and no wind. The effect varied according to the position of the thermistor and the direction of the solar radiation. Pérez and Alados-Arboledas (1999) compared two pyrgeometers with and without shading from direct solar radiation at Almería (6.83°N, 2.42°W) in southeast Spain. The differences in dome temperature and L_D between the pyrgeometer with and without shading reached 0.8 K and 22 W m^{-2}, respectively, for April to July. The solar heating effect reached 40 W m^{-2} with no wind and a small SZA. Pascal and Josey (2000) reported a +5 to 7 W m^{-2} error for a pyrgeometer in the weekly mean measurements at the sea surface in the North Atlantic in late spring 1998.

In this section, we analyze the downward surface radiation data of buoy observations in the Kuroshio current of the western Pacific Ocean from March 2006 to December 2009. The surface radiative flux data of the buoy observatories is compared with the ISCCP, JRA55 reanalysis product, and the radiative transfer calculated with MODIS. To compare the ocean site and land surface, the surface radiative flux data at TAT, which is the BSRN observatory closest to the buoys, is used. Because the nearest BSRN station is TAT, archived data on the buoys are compared with TAT to evaluate the accuracy of the sea surface sensor errors.

Table 2.12 shows the details of the radiometers on the buoy. The data collection period is from March 2006 to December 2009. Buoy radiation data are recorded by using 2- or 10-min-averaged data, and this section deals with 3-h and daily averaged data.

Table 2.13 shows the results of the comparison of L_D between in situ observations and retrievals for 3-h and daytime (12-h) averages. Under all-sky conditions, buoy bias is slightly positive, being +5 to 7 W m^{-2} (about 1–2%) for both 3-h and daytime averages. The land station shows negative or small positive biases (–8 to +1 W m^{-2}; –2 to +1%). For both the buoys and the

land station, RMSE is around ±20 to 26 W m^{-2} (±5 to 7%) and ±16 to 20 W m^{-2} (±4 to 6%) for 3-h and daytime averages, respectively. The positive biases at the sea surface with high temporal resolution correspond to the previous studies with weekly and monthly mean averages (Pascal and Josey, 2000; Wang and Dickinson, 2013). In these previous studies, the positive bias was caused by the dome-heating effect.

Table 2.12. Properties of flux sensors on buoys.

	Buoy (JKEO & KEO)	
Target	L_D	S_D
Model	PIR-TAO, Eppley	PSP-TAO, Eppley
Range	200 Wm^{-2} (thermopile)	200-1000 Wm^{-2}
Accuracy for daily totals	±1%	±1%

Table 2.13. Bias and RMSE (in situ observation minus satellite/reanalysis retrieval) of L_D [Wm^{-2}].

		All-sky		Clear-sky	
Site	Products	3-hour	Daytime	3-hour	Daytime
Buoy	ISCCP	+5.08 ± 21.9	+5.86 ± 19.7	+34.12 ± 27.6	+19.85 ± 12.5
	JRA55	+4.93 ± 19.0	+6.90 ± 17.4	+22.23 ± 20.4	+13.01 ± 7.0
	MODIS			+16.85 ± 15.2	
Land	ISCCP	−4.68 ± 26.5	−7.68 ± 20.3	+0.56 ±17.1	−4.43 ± 10.9
	JRA55	−0.48 ± 21.2	+1.43 ± 16.9	−1.74 ± 16.3	+1.09 ± 11.6
	MODIS			−5.67 ± 13.4	
Δ(Buoy-Land)	ISCCP	+0.40	+13.54	+33.56	+24.28
	JRA55	+5.42	+5.47	+23.97	+11.92
	MODIS			+22.52	

Under clear-sky conditions, buoy observatories have a positive bias, the same as under all-sky conditions, although the bias increases. Buoy observatories show positive biases larger than +16 to 34 W m^{-2} (+5 to 10%) and +13 to 20 W m^{-2} (+4 to 6%) for 3-h and daytime averages, respectively. The land station under clear-sky conditions shows a good correlation with satellite retrieval and reanalysis products with biases less than 5 W m^{-2} (about 2%), except for the MODIS 3-h average. Without the uncertainty caused by clouds, most of the biases for L_D at the land observatory under clear-sky conditions are better than those under all-sky conditions. The biases at buoy observatories under clear-sky conditions are larger than those under all-sky conditions.

Comparing buoy and land observatories, the biases of L_D at the sea surface are larger than those at the land surface for all retrievals both under clear-sky and all-sky conditions. Under clear-sky conditions, the biases of buoys are larger than those of the land station by +23 to 34 W m^{-2} and +12 to 24 W m^{-2} for 3-h and daytime averages, respectively. The clear-sky biases are caused by differences in buoy and land observations or sensors. There are two main differences between the buoys and land sensors: buoy observations are not shaded from direct solar radiation and have no ventilation, and buoys are affected by waves, whereas land sensors are not.

Table 2.14 shows S_D for in situ observatories and satellite or reanalysis products obtained from buoys and land observatories. Under all-sky conditions, the biases of the buoy stations compared with ISCCP are small, less than 4 W m^{-2} (~1%). The biases of buoys compared with JRA 55 underestimate the 3-h and daytime averages by –10 W m^{-2} (–2%) and –48 W m^{-2} (–11%), respectively. The RMSEs under all-sky conditions are large, approximately +70 to 90 W m^{-2} (~+14%) and +50 to 85 W m^{-2} (+12 to 18%) for 3-h and daytime averages, respectively. The land observatory shows similar biases to the buoy observatories under all-sky conditions; the bias for ISCCP is small and that for JRA55 is large.

Under clear-sky conditions, the negative biases of buoys for 3-h and daytime averages are –7 to –25 W m^{-2} (–1 to –4%) and –32 to –47 W m^{-2} (–7 to –13%), respectively, except for the comparison with MODIS. The RMSEs

Table 2.14. Bias and RMSE (in situ observation minus satellite/reanalysis retrieval) of S_D [Wm^{-2}].

		All-sky		Clear-sky	
Site	Product	3-hour	Daytime	3-hour	Daytime
Buoy	ISCCP	+1.53 ± 72.9	-3.9 ± 53.3	-6.53 ± 58.3	-31.98 ± 31.0
	JRA55	-10.02 ± 91.2	-47.58 ± 84.3	-24.82 ± 69.6	-47.14 ± 37.1
	MODIS			-107.22 ± 71.9	
Land	ISCCP	+3.76 ± 70.2	+6.56 ± 59.5	+6.24 ±22.8	+7.81 ± 14.7
	JRA55	-22.19 ± 77.3	-44.55 ± 78.4	-12.02 ± 23.6	-14.9 ± 12.3
	MODIS			-55.91 ± 43.7	
Δ(Buoy-Land)	ISCCP	-2.23	-10.46	-12.77	-24.17
	JRA55	+12.17	-3.03	-12.80	-32.24
	MODIS			-51.31	

for clear-sky conditions were ±20 to 50 W m^{-2} (±4 to 14%) smaller than for all-sky conditions for the 3-h and daytime averages. The land observatory contains a small bias with daytime averages under clear-sky conditions. The pyranometer underestimates S_D by more than 55 W m^{-2} (7%) compared with MODIS at both buoy and land observatories. The differences in biases for S_D between buoy and land observatories under clear-sky conditions show negative values, and the 3-h averages of the difference in bias are –12 to –13 W m^{-2}, but compared with the MODIS daytime averages they are –24 to –32 W m^{-2}.

The overestimation of pyrgeometer at the buoy observatory is mainly caused by the lack of a shading system and incident solar irradiance. When solar radiation enters the pyrgeometer dome, the silicon dome should reflect all shortwave irradiance. However, part of the incident shortwave is absorbed and warms the dome (Philipona et al., 1995). Meloni et al. (2012) compared pyrgeometers (PIR, Eppley; CG4, Kipp & Zonen) with a shading system and no shading in Lampedusa, Italy (35.52°N, 12.63°E). They observed a dome-heating effect of 10 and 12 W m^{-2} for PIR and CG4,

respectively, for the unshaded pyrgeometer. Udo (2000) compared an Eppley PIR with dome-heating correction and no correction in Nigeria (8.53°N, 4.57°E), and they showed that the clear-sky diurnal error of the pyrgeometer was 12% and 10% for the hourly and monthly averages, respectively. These errors decreased to approximately 1% under cloudy conditions. The dome heating is also reduced by a ventilation system. Previous studies were conducted mainly for land observatories.

The other explanation for buoy observatories overestimating L_D is rain error. Rain droplets on the pyrgeometer dome affect the sensor (Section 2.3.2). On the sea surface, the dome is also affected by sea spray droplets. The strong winds may create large waves and have the effect same as rain.

S_D estimated by a pyranometer varies with the position of the platforms because direct solar radiation is a dominant factor for global S_D. When the buoy moves, the pyranometer tilts and loses the irradiance from part of the sky because the pyranometer detects a hemisphere. The effect of tilting varies depending on SZA, pyranometer angle, and sky conditions. Tilt is classified into two types. One is a rocking motion caused by wave action. When the rocking motion directs the sensor toward or away from the sun, the error becomes positive or negative. The average of the error is not always zero, although it is not large. When the rocking motion is perpendicular to the sun direction, the error becomes negative, on the order of 10% for a 1-h average at a 10° tilt and SZA exceeding 30°. The error exceeds 40% of S_D with a mean tilt of 10° at a large SZA under clear-sky conditions, and the error is decreased by increasing the average time (MacWhorter and Weller, 1991; Wailser et al., 1999). Under cloudy conditions with opaque cloud, the cloud obscures the direct solar radiation and weakens the tilting effect. These errors due to tilt effects generally cause pyranometers to underestimate measurements. Salt accumulation also causes pyranometers to underestimate measurements after the evaporation of droplets.

Environmental factors, including rain, wind speed, tilt, sea spray, solar heating, and salt accumulation, affect the errors in radiative flux measurements on buoys. Rain rate and wind speed can be measured directly, and the solar heating correlates to the intensity of S_D or SZA. Evaluating the

intensity of sea spray is difficult. For example, Serra et al. (2001) investigated the error of the rain gauges of the ATLAS buoys. The authors sampled the rain gauge data for 25 days with no rain events and strong wind conditions (average wind speed of about 8 m/s). The rate of rain accumulation by sea spray is 0.01 mm/day and it has little effect. Therefore, we assumed that wind speed is associated with natural ventilation, the tilting effect, and sea spray. In this section, to evaluate the contributions of environmental factors to the errors in radiative flux measurements, we compare the difference between the in situ observed values and the satellite or reanalysis product values associated with rainfall, wind speed, and SZA.

The positive or negative correlation is tested by the Mann–Kendall rank-correlation test (Mann, 1945; Kendall, 1948). This is a nonparametric test that needs no hypothesis about the distribution of the population. In comparison with the linear regression analysis, the Mann–Kendall rank-correlation test is not affected by outliers, and is robust. In this section, "positive/negative correlation" indicates that the bias of an in situ observation increases/decreases, respectively, as the environmental factors rainfall, wind speed, and SZA increase. "Reliable" is satisfied at the 95% confidence level by comparing with both ISCCP and JRA55.

Figures 2.7 to 2.8 and Table 2.15 show the frequency distributions of the relative biases of radiative flux and environmental factors under all-sky conditions for L_D. Relative bias is defined as the ratio of the difference between in situ observations of radiative flux from ISCCP or JRA55 and observed values. On both the sea and land surface, rainfall shows a positive correlation for L_D at the 95% confidence level, owing to increased L_D from rain droplets.

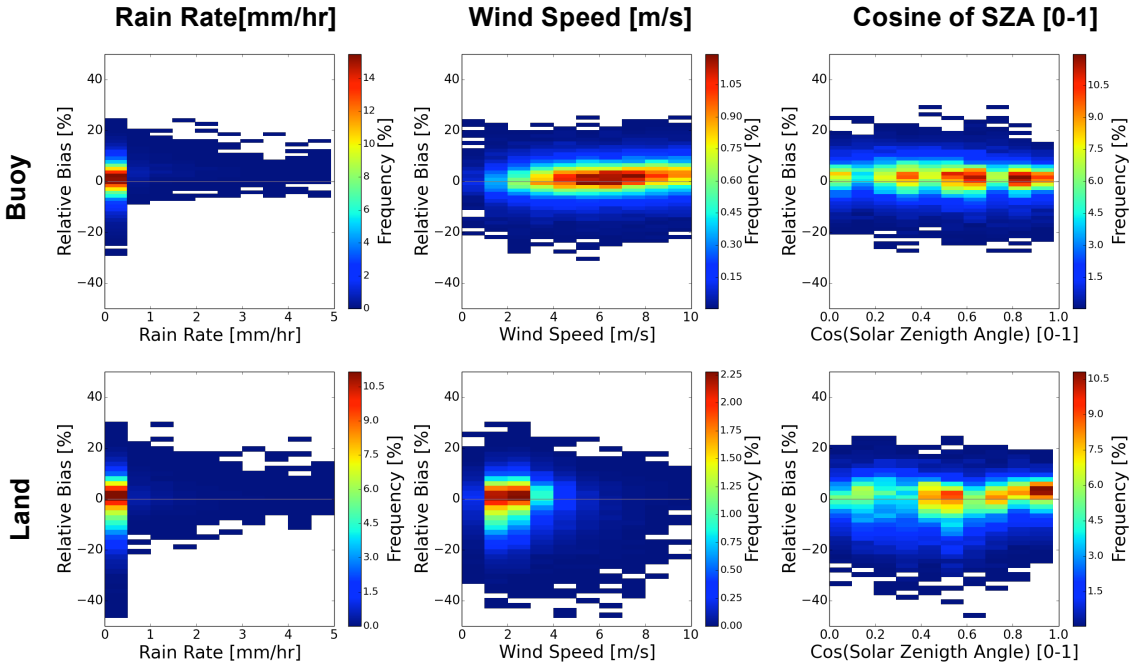

Figure 2.7. Frequencies of the relative bias of L_D and environmental factors (wind speed, cosine of SZA, rainfall, and cloud mask) at buoys (upper) and the land observatory (lower) under all-sky conditions for 3-h averages.

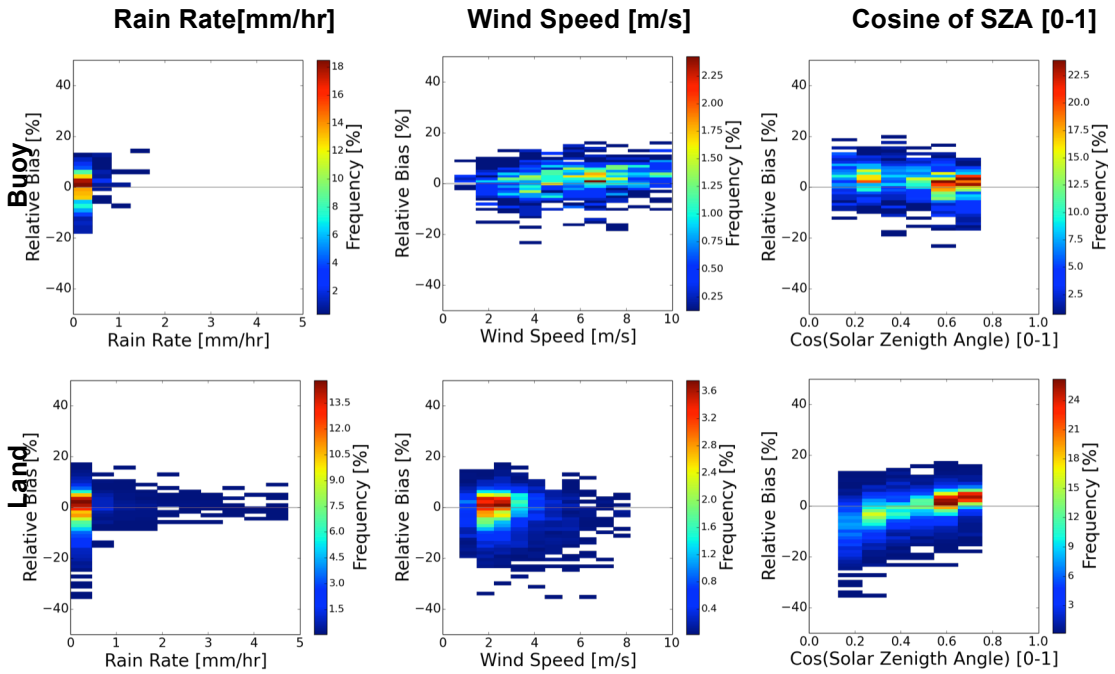

Figure 2.8. Frequencies of relative bias of L_D and environmental factors (wind speed, cosine of SZA, rainfall, and cloud mask) at buoys (upper) and the land observatory (lower) under all-sky conditions for daytime averages.

Table 2.15. Correlation of L_D by the Mann-Kendall rank correlation method. P or N indicates that increasing the factor increases the overestimation (positive correlation) or underestimation (negative correlation) of the buoy sensor at the 95% confidence level.

		All-sky		Clear-sky	
Factor	Site	3-hour	Daytime	3-hour	Daytime
Wind Speed	Buoy	P	P	P	P
	Land	-	-	-	-
Cosine of Solar Zenith Angle	Buoy	-	N	N	N
	Land	-	P	-	-
Rain Rate	Buoy	P	P		
	Land	P	P		

Under all-sky and clear-sky conditions, the overestimation of the pyrgeometer increases with increasing wind speed at the buoy observatory, whereas the land observatory does not show an increase. Perez and Alados-Arboledas (1999) investigated the effect of wind speed on solar heating at Almería (36.83°N, 2.42°W) in summer 1996. Under calm wind, Eppley PIR showed up to 40 W m^{-2} under large S_D conditions. The heating effect decreased as the wind speed increased by 8% per m s^{-1}. Our results show that wind speed under both all-sky and clear-sky conditions has a positive effect of 2.4% per m s^{-1}, which is not consistent with the results of the previous study. Sea spray is suspected to be a cause of the negative correlation; the sea spray on the dome of the pyrgeometer causes overestimation, similar to rain droplets. The continuous strong wind is probably caused by something else. At the land-surface observatory, the average wind speed is around 3 m s^{-1}, and wind speeds rarely exceed 5 m s^{-1}. Buoy observatories show average wind speeds of around 7 m s^{-1}, and sometimes exceed 15 m s^{-1}. Frequent strong winds provide natural ventilation, and reduce the dome-heating effect.

SZA is taken as a proxy for the intensity of solar radiation and solar heating. The cosine of SZA does not show a positive correlation with buoy L_D

values. In this work, the data with SZA larger than or equal to 70° are not used, and the effect of the difference in SZA is small.

Figures 2.9 and 2.10, and Table 2.16 show the frequency distributions of the relative biases of S_D and environmental factors under all-sky conditions. S_D observed at the buoy shows negative correlation with wind speed, whereas the land observatory shows a positive bias. The negative bias at the buoy is partly caused by the waves and tilting arising from strong winds. Tilting has two effects. When the tilting rocking motion is parallel to the sun direction, the effect is both overestimation (rocking toward the sun) and underestimation (rocking away from the sun). When the rocking motion is perpendicular to the sun direction, the effect is only underestimation (Katsaros and Devault, 1986). Because buoy tilting is a combination of the parallel and perpendicular rocking motion, the tilting of buoy observatories results in underestimation of S_D.

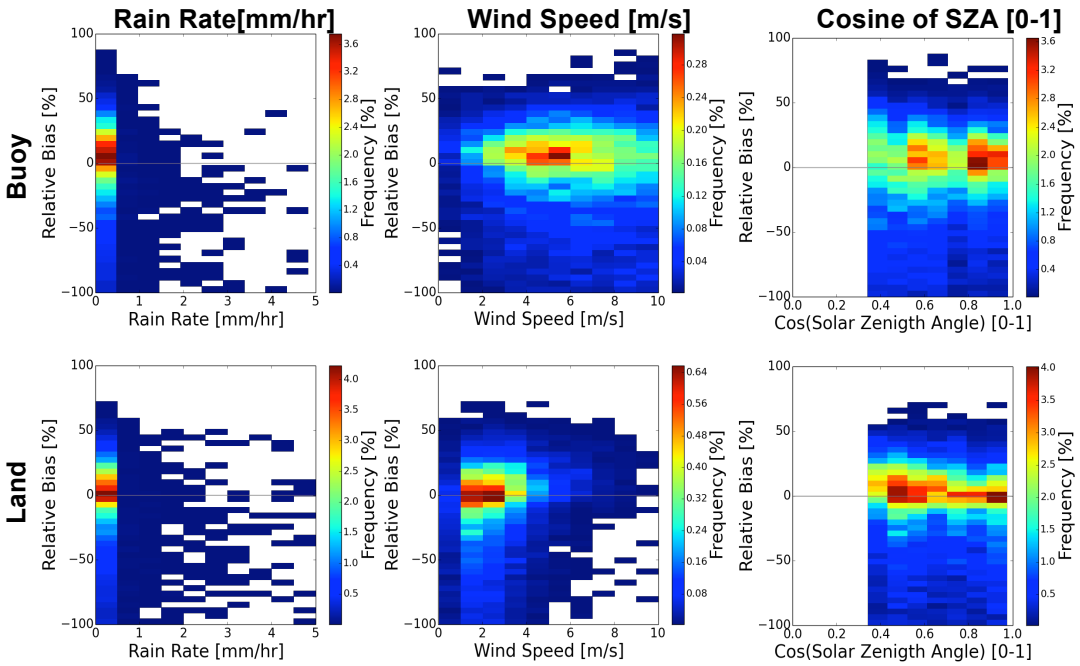

Figure 2.9. Frequencies of the relative bias of S_D and environmental factors (wind speed, cosine of SZA, rainfall, and cloud mask) at buoys (upper) and the land observatory (lower) under all-sky conditions for 3-h averages.

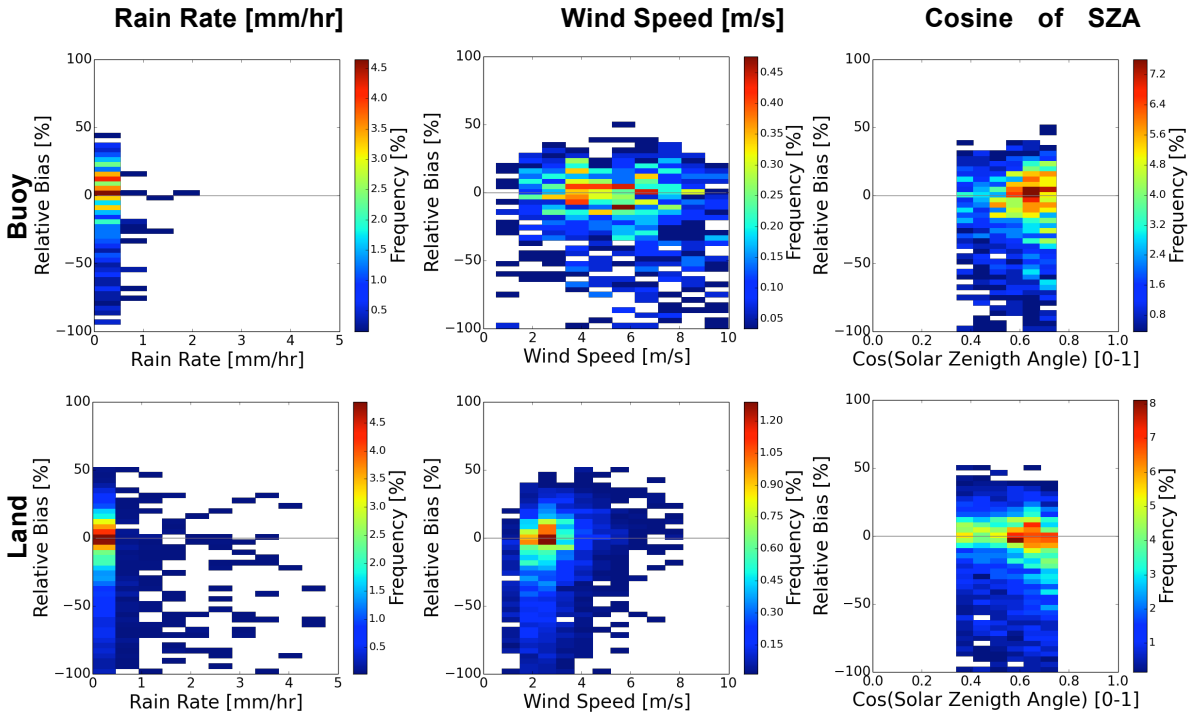

Figure 2.10. Frequencies of the relative bias of S_D and environmental factors (wind speed, cosine of SZA, rainfall, and cloud mask) at buoys (upper) and the land observatory (lower) under all-sky conditions for daytime averages.

Table 2.16. Correlation of S_D by the Mann-Kendall rank correlation method. P or N indicates that increasing the factor makes the buoy sensor increasingly overestimate (positive correlation) or underestimate (negative correlation) at the 95% confidence level.

		All-sky		Clear-sky	
Factor	Site	3-hour	Daytime	3-hour	Daytime
Wind Speed	Buoy	N	N	N	-
	Land	P	P	P	P
Cosine of Solar Zenith Angle	Buoy	P	-	P	-
	Land	N	N	-	-
Rain Rate	Buoy	-	-		
	Land	-	-		

Another reason for the negative correlation caused by wind is the salt accumulation on the dome. Medovaya et al. (2002) compared S_D between observation on buoys of the Woods Hole Oceanographic Institution and Pacific Marine Environmental Laboratory and calculation using the National Center for Atmospheric Research Community Climate Model version 3 (Kiehl et al., 1996) under clear-sky conditions. They found that most buoys showed good agreement with the model calculation, whereas in situ observations at some buoys were smaller than the model by about 40 W m^{-2} (10%). One of the reasons was the overestimation of model caused by insufficient estimation of the amount of aerosols. Another reason was considered for errors in the pyranometer observations. Aerosol and salt accumulation on the pyranometer dome affects observed shortwave radiation, especially in areas of high aerosol load or low rainfall frequency. In this study, the effect of wind on S_D is estimated to be around −2% per m/s. Rain may wash away the aerosol and salt accumulation and reduce the biases; however, S_D exhibited no correlation with the rain rate at the 95% confidence level in this study.

Based on these results, the accuracy of the surface radiation observations using pyranometers and pyrgeometers with no ventilation and solar shading systems on the ocean is insufficient. The biases of the radiometer at the buoy based on satellite data and reanalysis are larger by 23 to 34 W m^{-2} for L_D and smaller by 13 to 51 W m^{-2} for S_D than land observatories under all-sky conditions. The pyrgeometer errors on the buoy increases with increasing wind speed, and the pyranometer errors become more negative with increasing wind speed. The increase of errors results from strong winds creating sea-spray and causing tilting. SZA has a small effect on the target station. Rain has the same effect on the pyrgeometers on the buoy and at the land observatory.

2.4 Radiative transfer model

2.4.1 Estimation of contributions by using mstrnX

Broadband downward radiative flux was calculated by using mstrnX (Sekiguchi and Nakajima, 2008), a two-stream radiative transfer model. The model atmosphere is divided into plane-parallel layers, and the temperature and concentration of gases are constant in each layer. The layer thicknesses are 100 m (<10 km) and 1 km (10–100 km). The number of layers is 370.

The mstrnX considers 11 particle types and seven gases. Because the near-surface atmosphere is the dominant factor for L_D, we inserted the air temperature and concentration of WV from radiosonde observations into the vertical profile of mstrnX. The other concentrations of gases are from the US Standard Atmosphere (Anderson et al., 1986). Because the CO_2 concentration is different from the US Standard Atmosphere, the CO_2 concentration is corrected by the in situ observation data, which is adapted for the Arctic region (NYA) and Antarctic region (SYO, GVN, and SPO) by the data from the NYA and SYO stations (Nakazawa et al., 1991; Morimoto et al., 2003, Morimoto et al., 2006; http://tgr.geophys.tohoku.ac.jp/data), respectively, and for the other regions with the Mauna-Loa data from the Scripps Institution of Oceanography (Keeling et al., 2009; http://cdiac.ornl.gov/trends/co2/sio-keel.html). Aerosol amounts are taken from the rural model of Hänel (1976) for the troposphere and sulfuric acid (75% H_2SO_4) for stratosphere. AOD in the troposphere is from the ECMWF MACC Reanalysis. In the stratosphere, AOD is assumed to be constant and is given a value of 0.005 for 0.55 μm (Hess et al. 1998). Albedo is adapted from the monthly average data of CloudSat and CALIPSO from 2007 to 2009. In polar regions (NYA, GVN, SPO, and SYO), because the snow surface albedo is important to multiple scattering, albedo is evaluated by in situ observations under clear-sky conditions. In the months with no sunshine, the albedo is assumed to be the same as the highest albedo in the other months.

The model atmosphere is assumed to be under clear-sky and overcast conditions. Figures 2.11.a and b compare L_D and S_D, respectively, obtained by calculation and from all observed data at eight stations that have lidar or ceilometer measurements available under completely clear-sky condition

with the hourly average. Completely clear-sky conditions are defined as conditions with no cloud detected by visual, radiosonde, and lidar/ceilometer measurements. The RMSEs are -5.24 ± 4.3 and +21.24 ± 30.3 for L_D and S_D, respectively. Correlation coefficients both of L_D and S_D are larger than 0.99 and the calculation shows good correlation with the observations under clear-sky conditions.

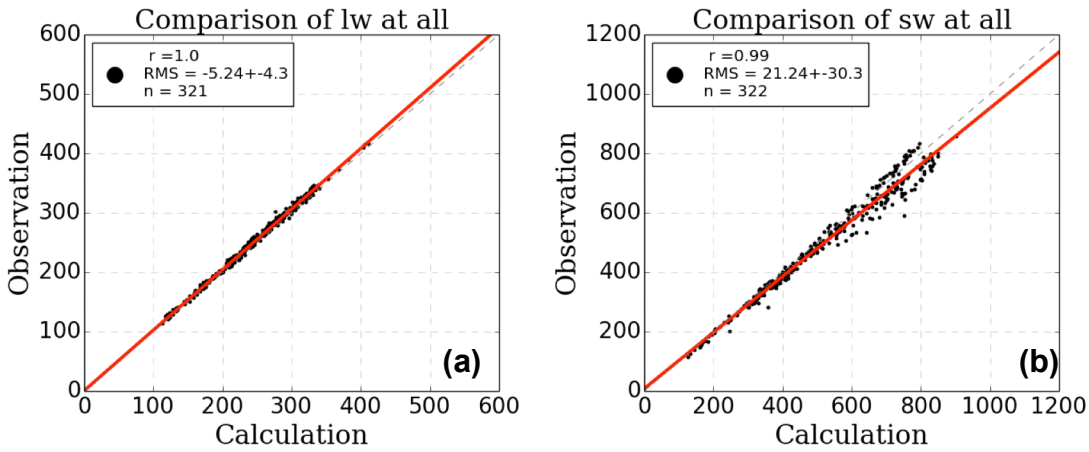

Figure. 2.11. Comparison of the surface radiative fluxes under clear-sky conditions.

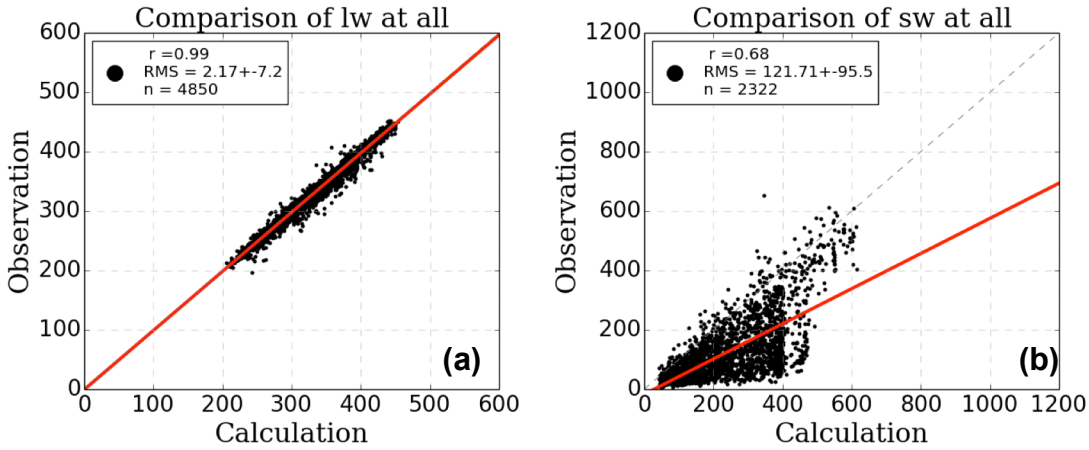

Figure. 2.12. Comparison of the surface radiative fluxes under overcast conditions, assuming cloud optical depth of 10 for 550 nm.

Overcast is defined as the conditions with CF_{Total} of 1.0 obtained by visual observation, radiosonde cloud geometrical thickness larger than 1.0 km, but no rain. Cloud optical depth is assumed to be 10 for 550 nm. Comparison of the calculations and observations under overcast conditions are shown in Figures 2.12.a and b. For L_D, the calculations have large variations. However, RMSE is 2.17 ± 7.2 W m^{-2} and they show good agreement with the observations, with a correlation coefficient larger than 0.99 also under overcast conditions. For S_D, RMSE is +121.71 ± 95.5 W m^{-2} and the calculations overestimate the surface radiative flux.

The large discrepancy is caused by the insufficient cloud optical depth assumed in calculation model. Figures 2.13.a, b are test-case calculations under US Standard Atmosphere conditions and SZA of 30° with cloud. CBH and cloud top height are 1.0 and 6.0 km, respectively. Cloud optical depth is 0 (no cloud), 1, 2, 5, 10, 20, and 30 for 550 nm. An increase in cloud optical depth increases the surface L_D; however, the increment ratio decreases for optical depths larger than 10 because the cloud behaves similar to a black body. However, S_D decreases with increasing cloud optical depths even larger than 20, because the cloud only scatters or absorbs sunshine and does not

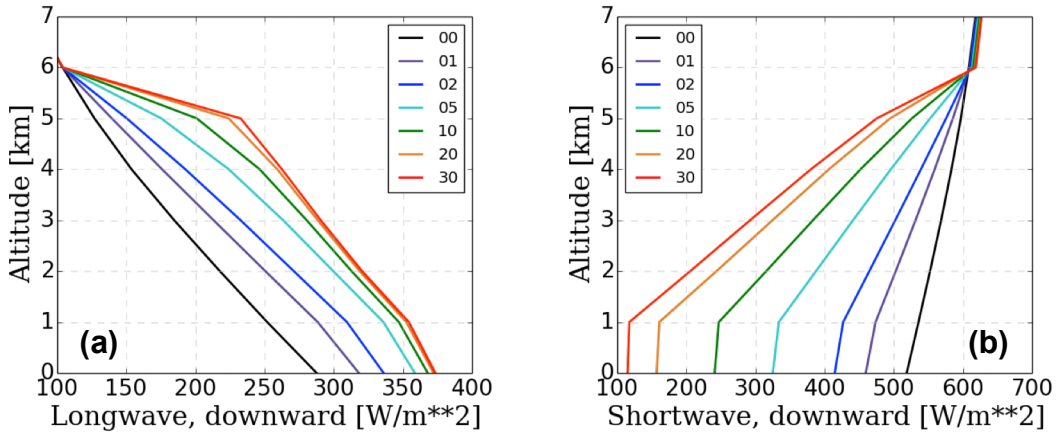

Figure. 2.13. Calculated downward longwave (left) and shortwave radiative fluxes. Atmospheric conditions are from the US standard model and SZA is 30°. CBH and cloud top heights are 3 and 6 km, respectively. Cloud optical depth is 0, 1, 2, 5, 10, 20, and 30 for 550 nm.

emit, unlike L_D; thus, it cannot be assumed that the optical depth is suitable for comparison with observations. The discrepancy in optical depth is frequently observed for PAY or LIN for spring and summer. An example of large overestimation of S_D is LIN, 12UTC, 5 May, 2001, with a calculated S_D of 412 and an observed S_D of 48 W m^{-2}. The CBH and cloud top height are 136 and 4000 m, respectively, and there is very thick cloud. Figure 2.14 shows the global, diffuse, and direct S_D around the target day. Direct S_D is near 0 W m^{-2} and is very small with a large albedo of thick cloud under completely overcast conditions. Based on these reasons, we do not estimate all radiative contributions to S_D and the total of longwave and shortwave downward radiation (T_D) under overcast conditions.

Radiative contributions to L_D by the removal method, REM_i, are evaluated by Eq. (2.10) as

$$REM_i = 1 - \frac{F_{Rem(i)}}{F_{Obs}} \ [\%], \tag{2.10}$$

where F_{Obs} is observed as the surface radiative flux and $F_{Rem(i)}$ is calculated by radiative flux removing factor i, such as WV or CO_2.

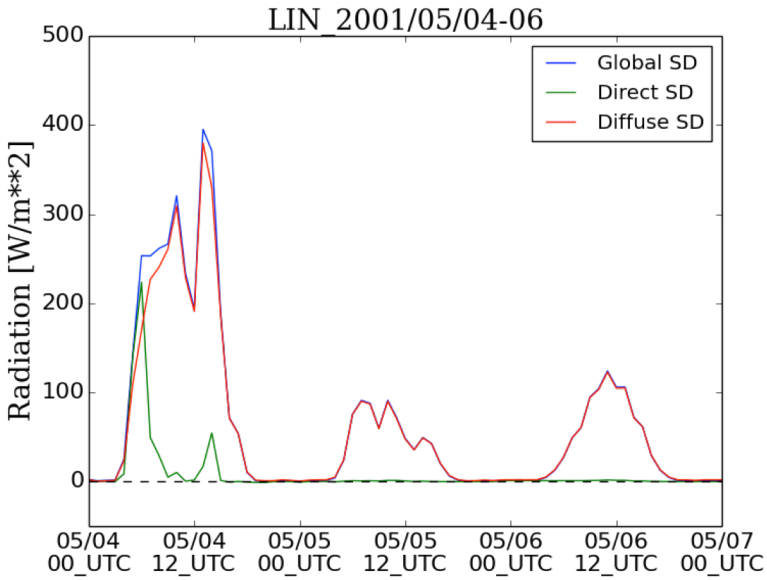

Figure 2.14. Observed global (blue), direct (green), and diffuse (red) S_D at LIN from May 4 to 6, 2001.

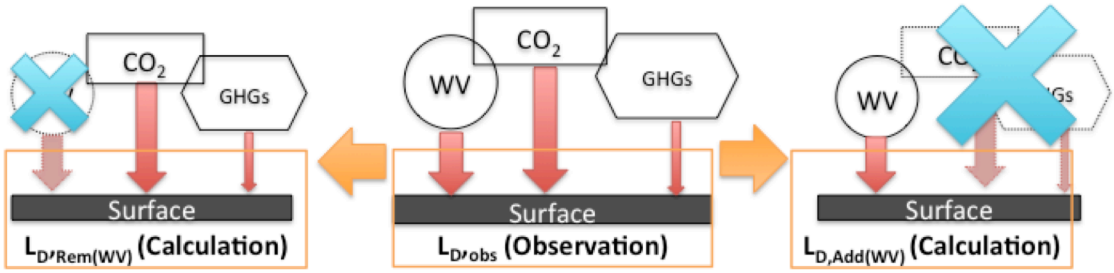

Figure 2.15. Contribution of WV by the removal method for L_D (left) and that by the addition method (right) to L_D.

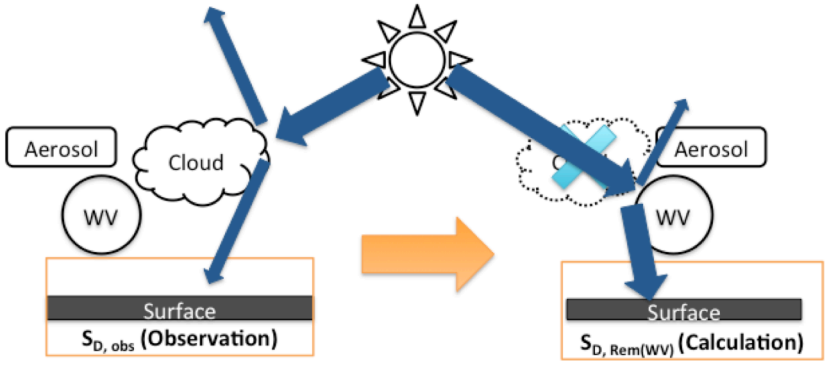

Figure 2.16. Contribution of cloud to S_D calculated by the removal method.

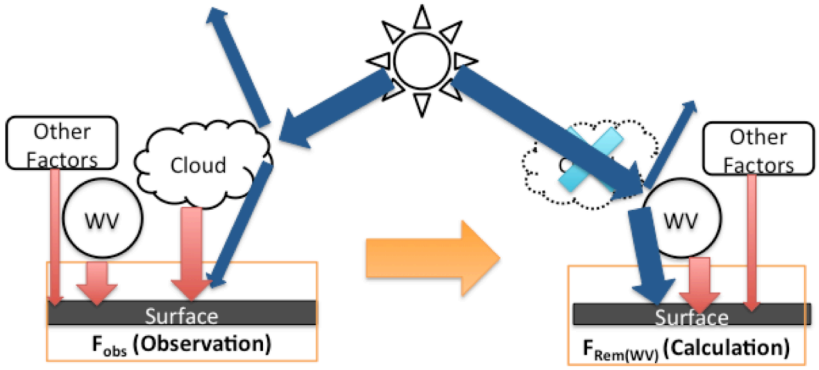

Figure 2.17. Contribution of cloud to T_D calculated by the removal method.

In the removal method, a single factor is removed from the atmosphere and the effect of the factor is evaluated. The method is affected by the interference between the removed factor and the remaining factors. For example, if WV is removed from the atmosphere, CO_2 or the other factors compensate for the absorption lines, reducing the effect of the removed WV. This is called the overlapping effect. To estimate the overlapping effect, we use the addition method, defined in Eq. (2.11) as

$$ADD_i = \frac{F_{Add(i)}}{F_{Obs}} \text{ [\%]}, \tag{2.11}$$

where $F_{Add(i)}$ is the calculated radiative flux with the removal all factors except factor *i*. Figure 2.15 shows a schematic of the removal and addition methods for L_D.

Radiative contributions to S_D by the removal method, REM_i, are evaluated by Eq. (2.12) as

$$REM_i = 1 - \frac{F_{Obs}}{F_{Rem(i)}} \text{ [\%]}. \tag{2.12}$$

The contribution to S_D calculated by the removal method indicates that the surface cools if *REMi* is positive. Figure 2.16 shows a schematic of the removal method for S_D.

Radiative contributions to T_D calculated by the removal method are evaluated to determine whether the factor is warming or cooling.

$$REM_i = \frac{(L_{D,Obs} - L_{D,Rem(i)}) + (S_{D,Obs} - S_{D,Rem(i)})}{L_{D,Obs} + S_{D,Obs}} \text{ [\%]}. \tag{2.13}$$

If REM_i for T_D is positive, the warming effect of cloud is larger than the cooling effect.

Under neither clear-sky nor overcast conditions, it is difficult to calculate radiative transfer accurately because of the difficulty in retrieving the cloud optical characteristics. REM_{Cloud} need only be valued by observation and clear-sky calculations. Therefore, under neither clear-sky nor overcast conditions, cloud radiative contribution is evaluated by the removal method. Figure 2.17 shows a diagram of the removal method for T_D.

2.5.2 RSTAR6b

To calculate the spectral properties of radiative transfer, we used RSTAR6b (Nakajima et al., 1986, 1988), which calculates the flux of a specific wavelength band with high resolution (<0.001 cm^{-1}) with a plain parallel atmosphere model. The RSTAR6b calculation is based on the discrete-ordinate method and the addition method. The layer thicknesses are 100 m from the surface to 15 km and 1000 m from 15 km to the top of the atmosphere. The maximum number of layers is 200. Vertical air temperature, WV, greenhouse gases, and aerosol profiles are taken from radiosonde observations, the US Standard Atmosphere, CO_2 surface observations, Hanel's model, and ECMWF MACC reanalysis, respectively, as they were for mstrnX. The absorption bands are defined as 20 to 550 cm^{-1} (500 to 18.2 μm) and 1375 to 1800 cm^{-1} (7.3 to 5.6 μm) for H_2O, 550 to 800 cm^{-1} (18.2 to 12.5 μm), and 800 to 950 cm^{-1} (12.5 to 10.5 μm) and 1100 to 1200 cm^{-1} (9.1 to 8.3 μm) for the window region (Town et al., 2005).

Chapter 3

Environmental Variations

In Chapter 3, the variation of surface radiative flux and the contribution of radiative factors to the surface downward radiation are compared with the contribution of surface air temperature (T_S), surface mixing ratio (M_S), and precipitable water (PW) to longwave downward radiation (L_D), and the cosine of solar zenith angle (SZA) to shortwave downward radiation (S_D) at 12 stations. The surface radiation data are averaged for 1 h around the time of the radiosonde observation. The target weather conditions are clear-sky, overcast, and all-sky conditions. Clear-sky conditions are defined as having a total cloud fraction (CF_{Total}) by visual observation of 0 and no cloud observed by radiosonde estimation. Overcast conditions are defined as having CF_{Total} obtained by visual observation of 1.0, and cloud geometrical thickness estimated by radiosonde larger than 1 km, and no rain. When it is overcast, the cloud optical depth in the radiative transfer model is 10 for 550 nm and the cloud base and top heights are estimated from radiosonde observations. It is assumed that cloud optical depth is insufficient for S_D calculations. Therefore, the cloud contributions to S_D and T_D are not estimated under overcast conditions. Because the Minamitori Island (MNM) and South Pole (SPO) stations in the Baseline Surface Radiation Network (BSRN) do not observe cloud fraction visually, these stations' data are not used for analyzing clear-sky and overcast conditions. All-sky conditions are defined as conditions without precipitation.

3.1 Longwave

3.1.1 Clear-sky

Figure 3.1 shows variations of the hourly mean observed L_D compared with T_S, M_S, and PW under clear-sky conditions at 10 stations. T_S, M_S, and PW show strong correlation with L_D under clear-sky conditions except for desert regions. The larger L_D in the desert region is caused by the smaller amount of water vapor (WV) and higher T_S than the other regions.

Figure 3.2 shows the radiative contributions of WV and CO_2 to L_D compared with T_S, M_S, and PW under clear-sky conditions at 10 stations. Teal, blue, orange, and red indicate REM_{WV}, ADD_{WV}, REM_{CO2}, and ADD_{CO2}, respectively. The maximum contribution obtained by the removal method for WV (REM_{WV}) is on 00UTC, July 18 2005 at Tateno (TAT) by 72.6% with T_S of 301.3 K, M_S of 18.4 × 10^{-3} g/g, and PW of 44.52 mm. This day also shows a minimum CO_2 contribution by the addition method (ADD_{CO2}) by 27.0%. Because the number of clear-sky days in tropical regions is small, TAT most frequently shows hot and humid atmospheric conditions. The minimum of REM_{WV} of 55.5% is found at 00UTC, September 8 2012 at Syowa (SYO) with T_S of 246.1 K, M_S of 0.15 × 10^{-3} g/g, and PW of 0.16 mm. The maximum of ADD_{CO2} is 44.4%. The maximum of radiative contribution of WV of 104.2% calculated by the addition method (ADD_{WV}) is found at 00UTC, July 19 1996 at TAT with T_S of 302.7 K, M_S of 17.5 × 10^{-3} g/g, and PW of 41.58 mm. This

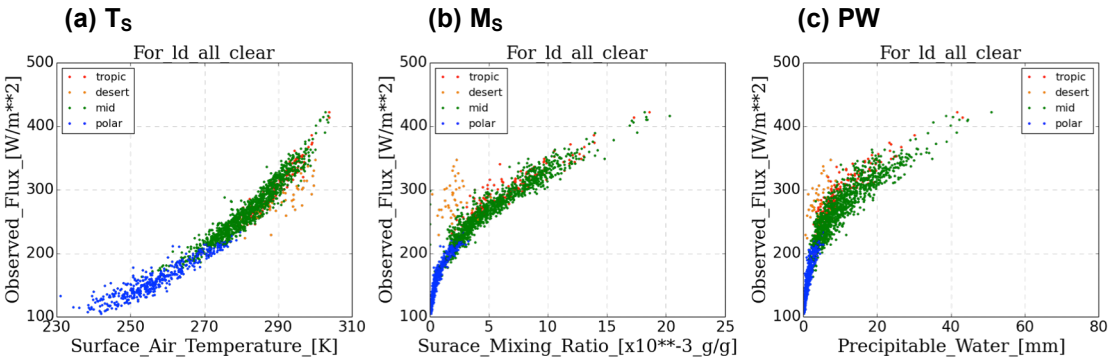

Figure 3.1. Relationships between L_D and T_S, M_S, and PW under clear-sky conditions at 10 stations. Red, orange, green, and blue indicate tropics, desert, mid, and polar regions, respectively.

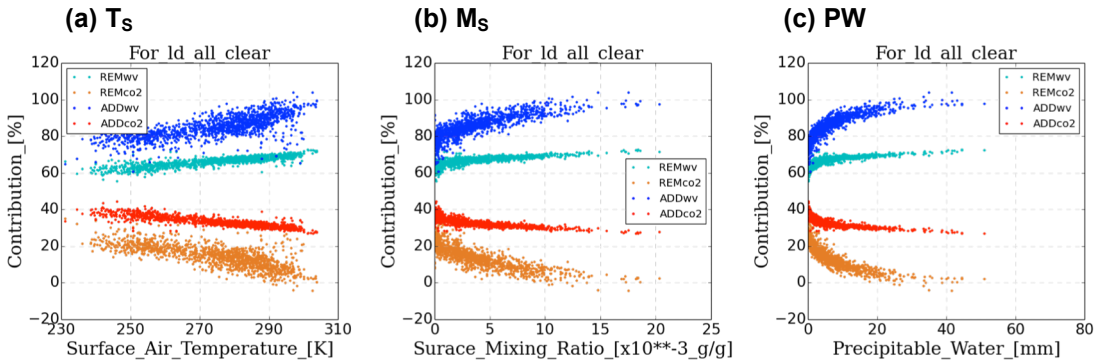

Figure 3.2. Relationship between radiative contribution of WV and CO_2 to L_D and T_S, M_S, and PW under clear-sky conditions at 10 stations. Teal, blue, orange, and red indicate REM_{WV}, ADD_{WV}, REM_{CO2}, and ADD_{CO2}, respectively.

day also shows the minimum contribution of CO_2 calculated by the removal method (REM_{CO2}) of -4.2%. The contribution sometimes exceeds 100% or is lower than 0%, because of the error of parameters in the radiative transfer model and in situ observations. ADD_{WV} reaches a minimum of 60.6% at 12UTC, September 1 2009 at SYO with 250.8 K of T_S, 0.36 × 10^{-3} g/g of M_S, and 0.60 mm of PW. This day shows the maximum of REM_{CO2} by 39.3%.

In all stations, radiative contributions of WV to L_D increase with increasing T_S, M_S, and PW. The contributions of CO_2 decrease with increasing air temperature and amount of WV. Most REM_{WV} (95% from the median of REM_{WV} at all stations by removing extremely large or small values) values range from +60% to 71%. REM_{WV} increases almost in proportion to the increase in T_S. In contrast, REM_{WV} increases exponentially with M_S and PW. Values 95% from the median of ADD_{WV} of +73 to +97% are very large. ADD_{WV} shows a greater change than REM_{WV}. Under humid conditions with PW larger than 40 mm, ADD_{WV} is larger than 95% and the radiative contribution of WV is dominant. The contribution of CO_2 is smaller than that of WV. Most REM_{CO2} values range from +3 to +27%. Except for the winter season in the polar region, REM_{CO2} is smaller than 20%. Values 95% from the median of ADD_{CO2} are from +29 to 40%. Table 3.1 shows the ranges of 95% of the radiative contributions from the median.

Table.3.1. Ranges of 95% contributions.

For L_D [%]		Clear	Overcast	All
Cloud	REM (CRC)		+6 to +29	−2 to +28
	ADD		+86 to +106	
WV	REM	+60 to +71	−6 to +11	
	ADD	+73 to +97	+61 to +93	
CO_2	REM	+3 to +27	−7 to +2	
	ADD	+29 to +40	+23 to +26	
For S_D [%]		Clear		All
Cloud	REM (CRC)			−5 to +85
WV	REM	+3 to +29		
Aerosol	REM	−4 to +24		
Albedo	REM	−11 to +16		
For T_D [%]				All
Cloud	REM (CRC)			−71 to +27

Both the air temperature and the amount of WV are important factors for L_D, although the effects are different. The variation of the radiative contribution with T_S is almost constant. When T_S increases by 70 K, the increases of REM_{WV} and ADD_{WV} are small and approximately 10 and 30%, respectively. However, the effects of M_S and PW depend on the WV amount. The variation of the radiative contribution changes rapidly under dry conditions, such as at Syowa (SYO) and Ny-Ålesund (NYA). If M_S and PW increase by 2.0×10^{-3} g/g and 5 mm in the polar region, REM_{WV} and ADD_{WV} increase by approximately 10%. The variations of REM_{WV} and ADD_{WV} are reversed compared with ADD_{CO2} and REM_{CO2}, respectively. Under clear-sky conditions, WV and CO_2 are the main factors emitting L_D, and the effects of the other factors are trivial.

WV has wide absorption bands, and some bands overlap with other gases strongly. For instance, the WV rotation band has a strong overlap with the 15 μm absorption band of CO_2. Therefore, when CO_2 is removed, the wide

overlapping absorption band of WV substitutes for the CO_2 band. The overlap causes the discrepancy in the maximum day between REM_{WV} and ADD_{WV}. In this study, the concentration of CO_2 is adjusted by the US Standard Atmosphere revised surface observed monthly mean values at Mauna-Loa (for mid-latitude and tropical regions), SPO (for Antarctica), and NYA (for the Arctic). The concentration of CO_2 in Mauna-Loa was 363.65 ppmv in July 1996 and 380.66 ppmv in July 2005. Because the addition method for WV is less susceptible to the overlapping effect of the other greenhouse gases (GHGs) than the removal method, the maximum REM_{WV} is at 00UTC, July 18 2005 with 44.52 mm PW, which is a larger PW than at 00UTC, July 19 1996 with 41.58 mm.

Because the removal method is performed by removing a single factor from the atmosphere calculations, the contribution to L_D calculated by the removal method is affected by the intensity of the overlap effect. However, because the addition method evaluates the radiative contribution by removing all factors without the target factor, the contribution by the addition method ignores the effect of overlapping. Therefore, the difference in the contributions calculated by the addition and removal methods ($\Delta CON_X = ADD_X - REM_X$) is an index of the overlap intensity. The overlap between WV and CO_2 is strong in bands 4 to 6 (18.9 to 13.3 μm) and bands 13 to 14 (7.14 to 4.0 μm). Table 3.2 shows the mstrnX integration bands.

Table.3.2. Integration bands of mstrnX for L_D.

Band	Wavelength[μm]	Major Absorber	Band	Wavelength[μm]	Major Absorber
1	200-40	H_2O	8	12.2-10.2	
2	40-25	H_2O	9	10.2-8.51	O_3
3	25-18.9	H_2O	10	8.51-8.16	
4	18.9-16.4	H_2O, CO_2	11	8.16-7.55	
5	16.4-14.9	CO_2	12	7.55-7.14	H_2O, CH_4, N_2O
6	14.9-13.3	CO_2	13	7.14-5.00	H_2O, CO_2
7	13.3-12.2	CO_2	14	5.00-4.00	H_2O, CO_2

Figure 3.3-5 shows the variations in the contributions to L_D in band 1 to 14 compared with T_S, M_S, and PW under clear-sky conditions. From band 1 to 3 (200 to 18.9 μm), the contributions of WV and CO_2 are always 100 and 0%, respectively. L_D in band 1 is nearly constant at 20 W m^{-2} except for polar regions. Bands 2 to 3 show large variations in L_D corresponding to changes in T_S and the amount of WV. Compared with cold, dry conditions, warm, wet regions show L_D values larger than 20 and 50 W m^{-2} in bands 2 and 3, respectively. These bands from 1 to 3 occupy approximately one-fifth of the total L_D. Therefore, the variation in the amount of WV has a large effect on the variation of the total L_D. However, the contribution of CO_2 is 0% and has no effect on these bands. The contribution of WV is smaller from band 4 to 6 (18.9 to 14.9 μm) than from band 1 to 3. Except for band 4, REM_{WV} is approximately 0%. In contrast, ADD_{WV} reaches nearly 100% for large PW and T_S. The difference in contributions between removal and addition is caused by the strong overlapping such as between the rotation band of WV and the 15 μm absorption band. The radiative contribution of CO_2 becomes very large in the polar region in bands 5 to 6. The bands show nearly 100% of the contributions of CO_2. Bands 7 to 10 (13.3 to 8.16 μm) show small ΔWV and overlapping effect. These wavelengths contains an atmospheric window, normally defined as 8 to 12 μm, and L_D in these bands are much smaller than 30 W m^{-2}, except for at T_S larger than 300 K. The variations in the contributions of the bands are small. Bands 11 to 12 (8.16 to 7.14 μm) show a small L_D of less than 20 W m^{-2}. The band contains strong absorption bands of CH_4 (7.6 μm), N_2O (7.8 μm), and GHGs other than WV or CO_2. Therefore, ΔWV is large, up to 50%, although the large overlapping is not caused by CO_2, and the CO_2 contributions calculated by both the removal and addition methods are very small. Band 13 (7.14 to 5.00 μm) is dominated by the WV effect. The contribution of WV to the band is 100% and the contribution of CO_2 is 0%. Band 14 (5.00 to 4.00 μm) has a large ΔWV and large overlaps, whereas the L_D of this band is smaller than 10 W m^{-2} and it has a small effect on the total L_D.

Based on these results, ΔWV is 50 to 100% in bands 4 to 6 and 50% in band 12 under warm, wet conditions. Bands 4 to 6 are affected by the overlap

between the WV rotation band and the CO_2 15 μm absorption band. Band 12 is affected by WV, CH_4, and N_2O. Town et al. (2005) calculated L_D from WV and CO_2 by using the line-by-line radiative transfer model in Antarctica. When only the temperature profile in the radiative transfer model is changed from summer to winter, the surface radiative flux emitted by WV decreases by 17 W m^{-2}. When only the mixing ratio in the model is changed from summer to winter, the surface radiative flux emitted by WV decreases by 12 W m^{-2}, which is smaller than the decrease caused by changing the temperature profile. This results from the large overlap between the WV rotation band and the 15 μm absorption band of CO_2.

Figure 3.6 shows the L_D calculated by RSTAR6b with typical vertical profiles of air temperature and humidity in sub-tropical, desert, mid-latitude, and polar regions constructed from the averages of radiosonde data under clear-sky conditions. WV bands are defined as 420 to 550 cm^{-1} (24.0 to 18.2 μm) and 1375 to 1800 cm^{-1} (7.3 to 5.6 μm). The CO_2 absorption band is 550 to 800 cm^{-1} (18.2 to 12.5 μm), and the window regions are 800 to 950 cm^{-1} (12.5 to 10.5 μm) and 1100 to 1200 cm^{-1} (9.1 to 8.3 μm) (Town et al., 2005).

The WV band makes a large contribution to the surface L_D, and up to 20 W m^{-2} μm^{-1} around 8 or 15 μm there are strong WV absorption lines. When WV is removed, the 8 μm absorption band has a large effect. In contrast, the 15 μm absorption band has a small effect. Figure 3.7 shows the differences in narrow-band L_D calculated under normal conditions and with the removal of WV or CO_2. The 15 μm absorption band in Figure 3.7.a is approximately 0 W m^{-2} μm^{-1} because of the overlap with CO_2. The effect of CO_2 around 15 μm is significant in desert regions (Figure 3.7.b) and it reaches 15 W m^{-2} μm^{-1} because of the small amount of WV and high T_s.

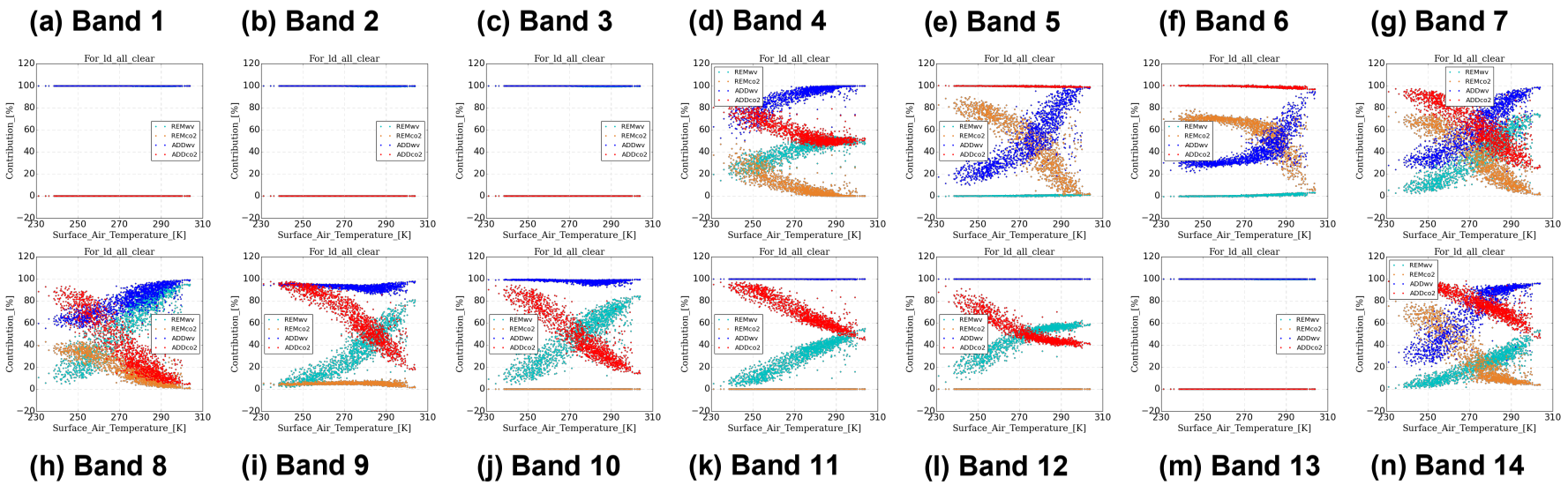

Figure 3.3. Relationship between T_S and contributions to L_D under clear-sky conditions.

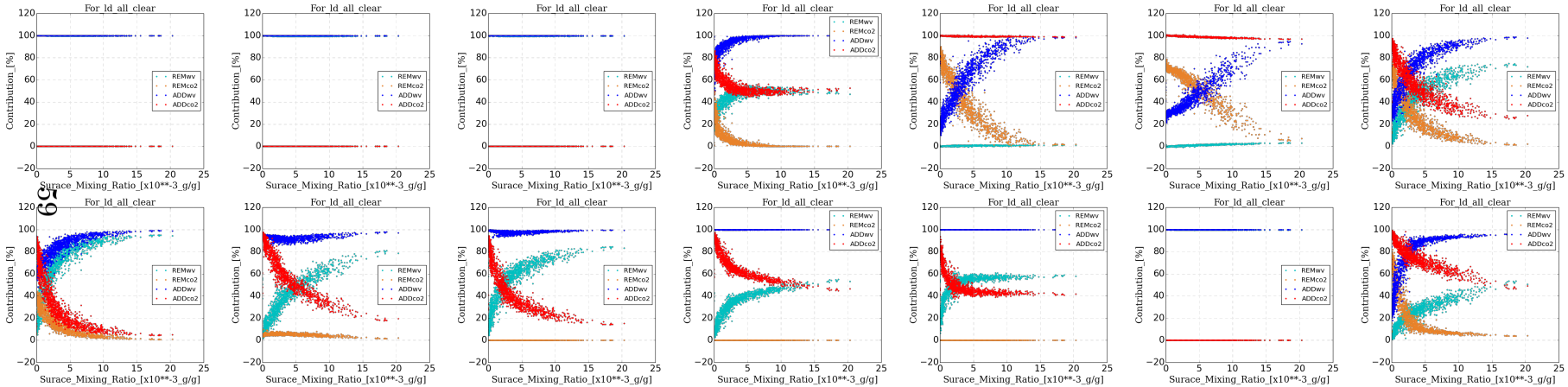

Figure 3.4. Relationship between M_S and contributions to L_D under clear-sky conditions.

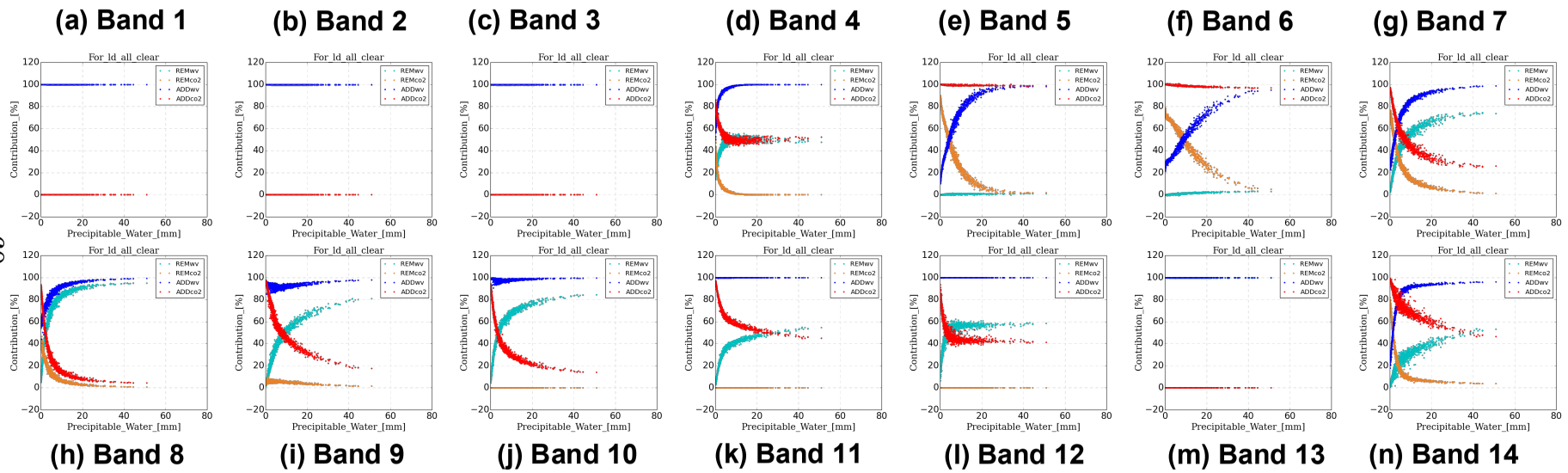

Figure 3.5. Relationship between PW and contributions to L_D under clear-sky conditions.

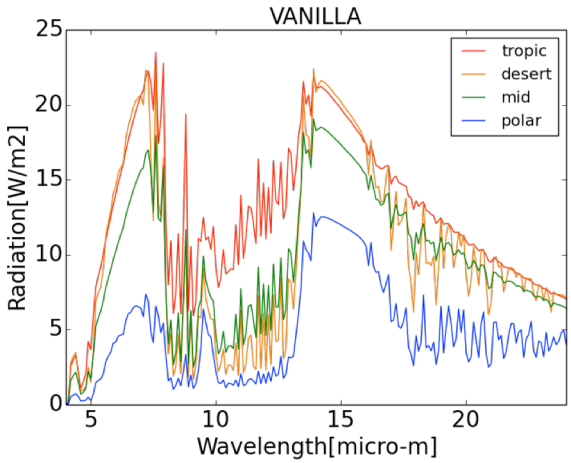

Figure 3.6. L_D calculated by RSTAR6b in sub-tropical (red), desert (orange), mid-latitude (green), and polar region (blue) under clear-sky conditions.

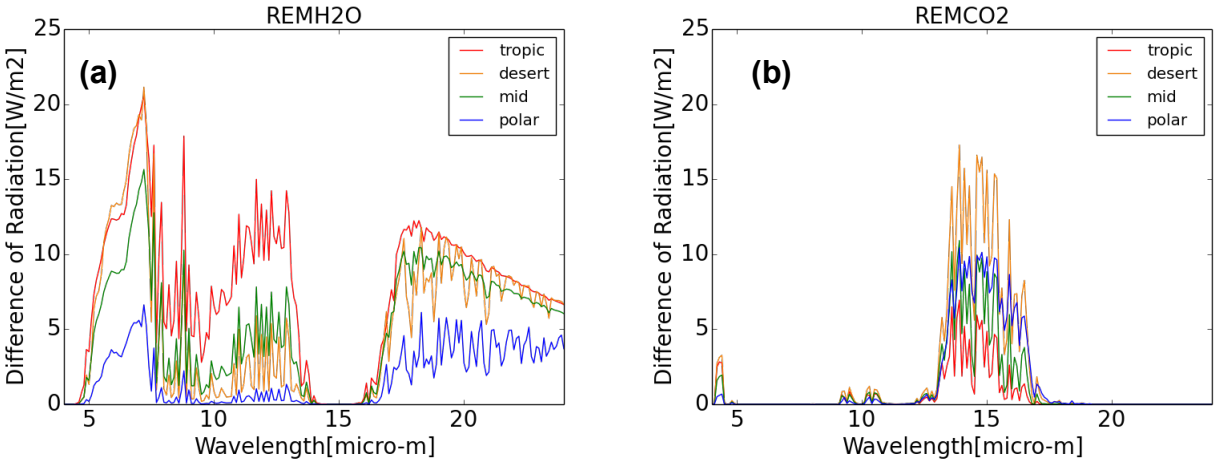

Figure 3.7. Difference in L_D between normal conditions and after removal WV or CO_2 in sub-tropical (red), desert (orange), mid-latitude (green), and polar (blue) regions under clear-sky conditions.

3.1.2 Overcast-Sky

Overcast in the present study is defined as conditions with visually observed CF_{Total} of 1 (sky is completely covered by cloud), cloud geometrical thickness larger than 1 km, and no precipitation. In the radiative transfer model, cloud optical depth is assumed to be 10 for 550 nm. Because the assumption shows good agreement with observations for only L_D, S_D and T_D are not calculated under overcast conditions. MNM and SPO do not record visual CF_{Total} observations. Therefore, overcast-sky analysis is only performed at the other 10 stations.

Figure 3.8 shows variations in L_D compared with T_S, M_S, and PW under overcast conditions. Similar to clear-sky conditions, L_D under overcast conditions has a strong correlation with T_S, M_S, and PW. Figure 3.9 shows the variations in the radiative contributions of cloud, WV, and CO_2 to L_D under overcast conditions. Because of thick cloud, the contributions of WV

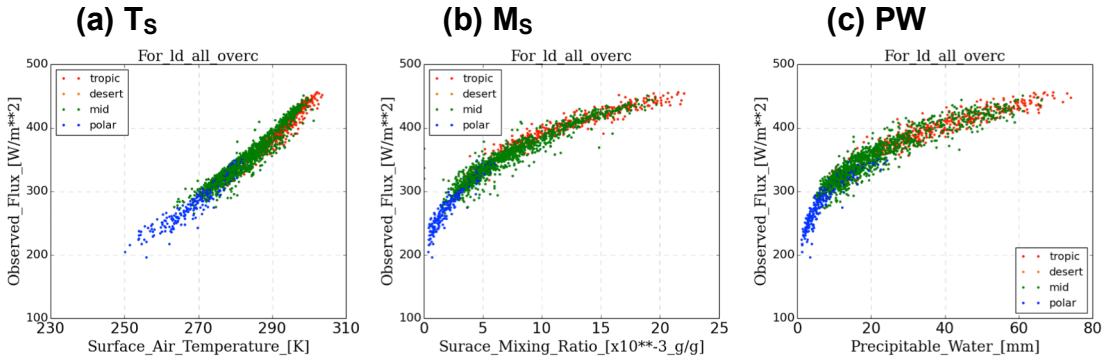

Figure 3.8. Relationships between L_D and the environmental factors (a) T_S, (b) M_S, and (c) PW, under overcast conditions at 10 stations.

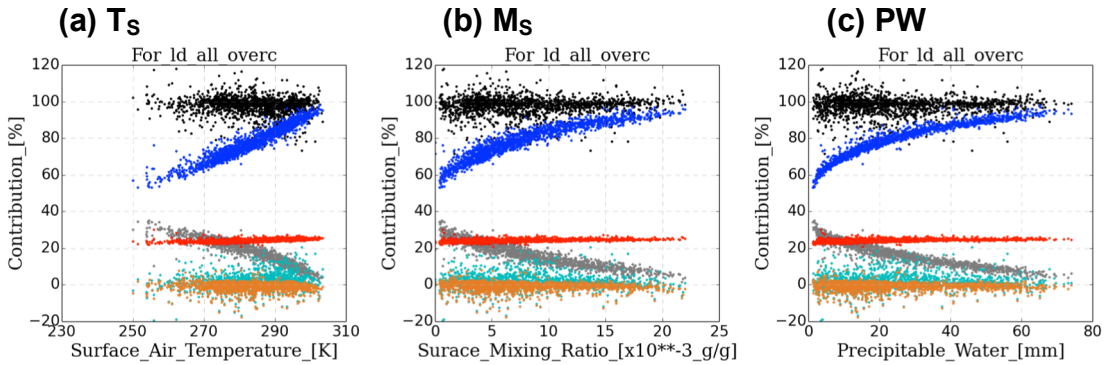

Figure 3.9. Relationships between the contributions of cloud, WV, and CO_2 to L_D and (a) T_S, (b) M_S, and (c) PW, under overcast conditions.

and CO_2 are smaller than under clear-sky conditions. In particular, REM_{WV} is small and ranges from -19.4 to +20.6%. Even under wet and warm conditions, REM_{WV} is generally smaller than 10%. ADD_{WV} is still large and remains from +53.2 to +98.0%. Under warm, wet conditions, ADD_{WV} exceeds 95%, whereas for the mid-latitude and polar regions ADD_{WV} indicates a contribution smaller by 10 to 30% than under clear-sky conditions. ADD_{WV} under overcast conditions shows a strong correlation with the temperature and amount of WV, the same as under clear-sky conditions. However, the variation in REM_{WV} is different from under clear-sky conditions.

Figure 3.10 shows that the relationship between the subtraction of the cloud base temperature from T_S and radiative contributions to L_D. REM_{WV} has strong correlations with the difference in temperatures between the surface air and cloud base. Under overcast conditions, optically thick cloud has a large effect on L_D. When WV is removed, the thick cloud replaces the absorption band of WV.

The contributions of CO_2 under overcast conditions are much smaller than under clear-sky conditions for the same reason as for WV. REM_{CO2} is from -17.8 to +8.2%. The wide absorption band of thick cloud overlaps with CO_2 and weakens effect of CO_2. ADD_{CO2} is from +20.9 to +30.3%, and is almost constant. Under overcast conditions assuming optical thick cloud, cloud makes the largest contribution.

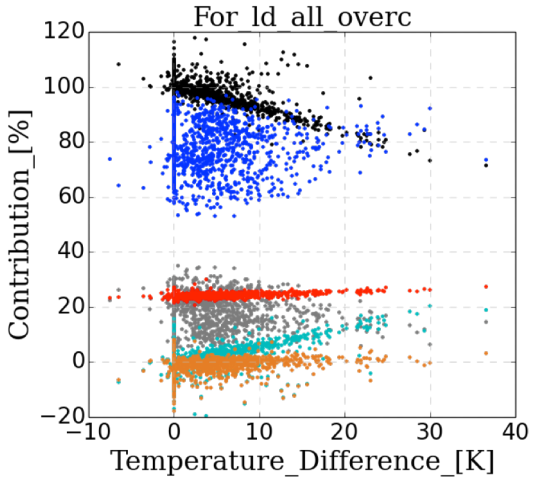

Figure 3.10. Relationship between the subtraction of cloud base temperature from T_S and the radiative contribution to L_D.

REM_{Cloud} and ADD_{Cloud} range from +1.5 to +35.0% and from +71.7 to +117.9%, respectively. ADD_{Cloud} does not show a correlation with T_S and the amount of WV. ADD_{Cloud} is correlated with the difference in air temperature between the surface and CBH, as it is for REM_{WV}, because the effects of gases except WV are much smaller than those of WV and cloud.

Some days under overcast conditions show contributions larger than 100% or smaller than 0% because L_D is larger than for normal conditions owing to the removal method or cloud. At 12UTC, 20 July 2001 in SYO, REM_{WV} and REM_{CO2} are -0.8% and -1.0%, respectively, and ADD_{Cloud} is

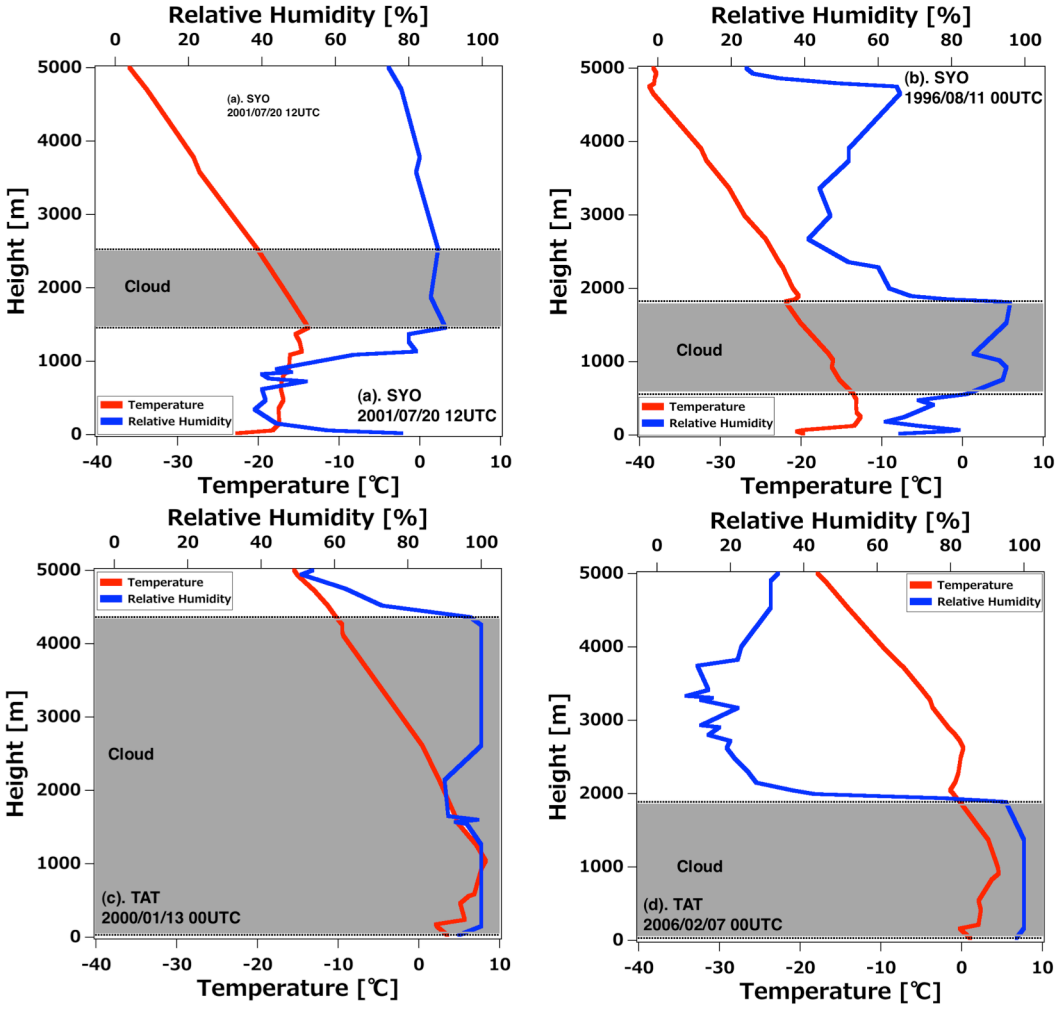

Figure 3.11. Vertical profiles of air temperature and relative humidity with a larger cloud contribution to L_D than 100%.

(a) 12UTC, 20 July 2001 at SYO. (b) 00UTC, 11 August 1996 at SYO.

(c) 00UTC, 1 January 2000 at TAT. (d) 00UTC, 7 February 2006 at TAT.

103.0%. At 00UTC, 11 August 1996 at SYO, REM_{WV}, REM_{CO2}, and ADD_{Cloud} are -0.6, -0.6%, and +101.1%, respectively. At 00 UTC, 13 January 2001 at TAT, REM_{WV}, REM_{CO2}, and ADD_{Cloud} are -0.5, -0.1, +100.7%, respectively. At 00UTC, 7 February 2006, 00UTC at TAT, REM_{WV} and ADD_{Cloud} are -0.1 and +100.1%, respectively. The values are negative and exceed 100% contributions because of errors in the radiative transfer calculation and L_D observations, and because of temperature inversion.

Contributions larger than 100% or smaller than 0% frequently occur in polar regions. Under very cold conditions, pyrgeometer data contain large errors because the sensitivity of the thermopile is low (see Section 2.3.2). The low-temperature error results in pyrgeometer overestimation; therefore, the radiative contribution both by removal and addition methods tends to be smaller from Eqs. (2.10) and (2.11). However, contributions larger than 100% and smaller than 0% also appear in mid-latitude regions. Figure 3.11 shows the vertical radiosonde profiles of air temperature and relative humidity of days with negative cloud contributions. The days with larger ADD_{Cloud} than 100% have a temperature inversion layer, and the emission from cloud after removing GHGs becomes strong.

3.1.3 All-sky

It is difficult to retrieve cloud optical characteristics with in situ observations and calculate the radiative transfer in the calculation model under all-sky conditions. Therefore, in this section, we calculate the radiative contribution of just cloud by the removal method, which can be estimated without cloud information. The variation in the cloud radiative effect (CRE) as absolute value, and the cloud radiative contribution (CRC) as relative value under all-sky conditions are analyzed compared with T_S and PW. Precipitation day is eliminated because of the rain error.

Figure 3.12 shows the variations in L_D, CRE, and CRC as a function of the shortwave diffusivity index (SDI) at the 12 BSRN stations during the day. CRC has a large variability from -6% to 38%. Values 95% from the median of CRC to L_D are from -5% to 35%. Cloud effects increase both

absolutely and relatively with increasing SDI. The Mann-Kendall rank correlation test (Mann, 1945; Kendall, 1948) shows that the increases are reliable at the 95% confidence level although there is large scattering.

PW is an important factor in evaluating cloud effect because WV is a strong absorber and emitter of longwave radiation. We classified the observation sites into regions: sub-tropical (Fukuoka, Ishigaki Island, and MNM), desert (Tamanrasset), mid-latitude (Sapporo (SAP), Lindenberg (LIN), Payerne (PAY), and TAT), and polar (NYA, Georg von Neumayer Station (GVN), SYO, and SPO). CRE shows small dependency on the regions, although the observed L_D is different in the four regions. Therefore, CRCs between the polar and sub-tropical regions show large differences with SDI larger than 0.4. When SDI is less than 0.4, CRC is hardly affected by humidity except for the desert region, which has a lower number of cloudy days than the other regions.

The standard deviation of CRC is larger in the polar region than that in the tropical region. In the polar region, the average CRC ranges from about 0% to more than 20%. In general, the average CRC decreases with increasing PW. The effect of cloud is large in the polar region because the effect of WV is small. Accordingly, differences in cloud physical characteristics (e.g., cloud thickness, altitude, and amount) are more important under dry conditions than under humid conditions, causing CRC to exhibit large variability.

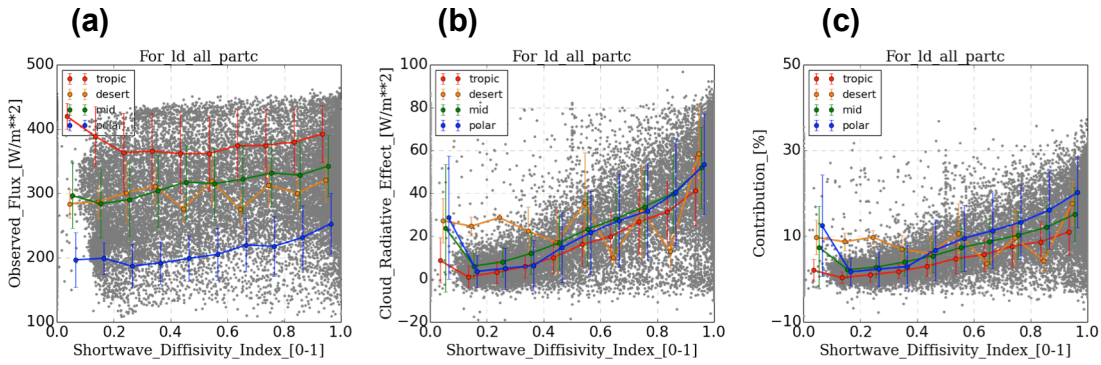

Figure 3.12. Daytime relationship between SDI and (a) L_D, (b) CRE, and (c) CRC under all-sky conditions with no precipitation. Red, orange, green, and blue lines indicate sub-tropical, desert, mid-latitude, and polar regions, respectively.

Figure 3.13 shows the variations in observed L_D, CRE, and CRC compared with PW. CRE shows large variability. The average of CRE shows a small correlation with PW. However, L_D increases strongly with PW because of the emission of large amounts of WV. The increase in L_D and the small decrease in CRE with the increase in PW result in CRC decreasing. In desert regions, the number of observations with PW larger than 20 mm is very small, and the variation of the average CRE is very different from mid-latitude and tropical regions. In polar regions, the amount of WV is very small. Thus, the cloud effect is larger than under humid conditions, and CRC sometimes reaches nearly 40%. CRE in polar regions is much larger than in mid-latitude and tropical regions with PW from 10 to 40 mm. The large discrepancy is caused by optically thick cloud with large PW, and the frequency of large PW values is small in polar regions.

Stephens et al. (2012) showed the relationship between CRE and column WV by using A-Train satellite data (Figure 3.14). The temporal and spatial resolutions of the data are 3 h and 1°, respectively; these resolutions are much coarser than those of the in situ data (1 h and 1 point). Our results show good agreement with those of Stephens et al. They found the three following relationships between CRE and column WV. In areas where the

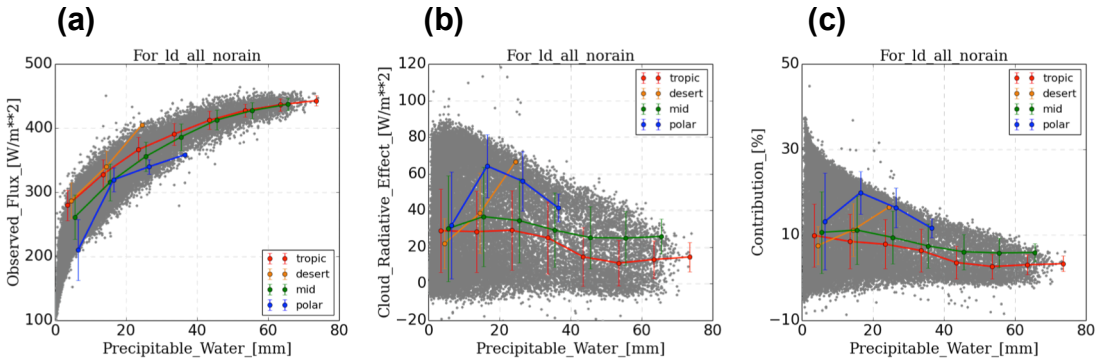

Figure 3.13. Relationship between PW and (a) L_D, (b) CRE, and (c) CRC under all-sky conditions with no precipitation. Red, orange, green, and blue lines indicate sub-tropical, desert, mid-latitude, and polar regions, respectively.

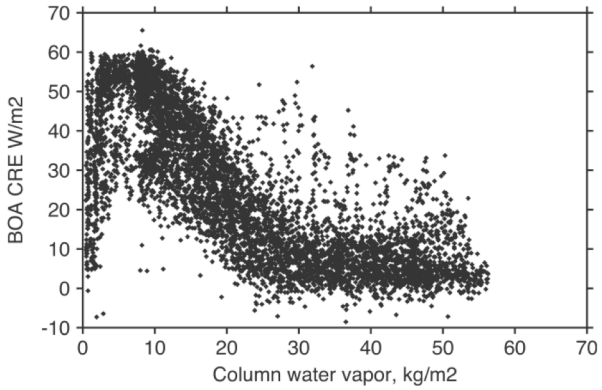

Figure 3.14. CRE as a function of column WV estimated by satellite retrievals (from Stephens et al., 2012).

amount of column WV is 0 to 10 mm, CRE increases with increasing WV. In areas where the amount of WV is 10 to 40 mm, CRE is inversely proportional to the amount of WV. In Figure 3.13.b, these increasing and decreasing trends are reliable according to the rank correlation test at the 95% confidence level, although scattering is large. Under very humid conditions, in which WV is larger than 40 mm, CRE is insensitive to changes in the amount of WV. However, Stephens et al. (2012) did not report details of the variation in cloud effect. There are two clear differences between the present study and that of Stephens et al. First, the present study shows a high incidence of a large negative cloud effect in very cold, dry regions. Second, the range for CRE is wider in the present study.

Cloud effect sometimes takes a negative value. In an Arctic study, Shupe and Intrieri (2004) suggested that negative values for cloud effect could be attributed to model or observation errors under clear-sky conditions. However, the negative cloud effect values tend to concentrate in the low-PW region in the scatterplots, suggesting that there may be another reason for the negative values. The temperature inversion layer causes the negative contribution under all-sky conditions, similar to overcast conditions. Figure 3.15 shows the relationship between PW and L_D, CRE, and CRC partitioned by a temperature inversion. The orange curve show data for a temperature inversion below 3000 m, that has an intensity (difference in temperature

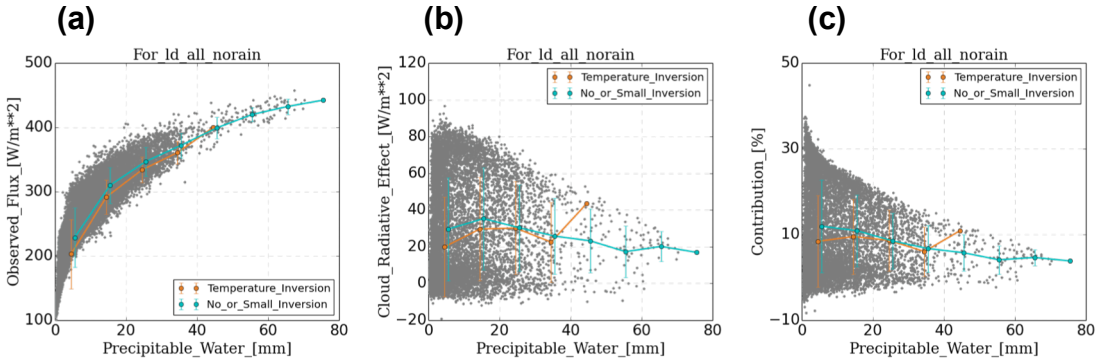

Figure 3.15. Relationship between PW and (a) L_D, (b) CRE, (c) CRC under a strong temperature inversion (intensity > 3 K) and no temperature inversion.

between maximum inversion layer and the surface atmosphere) greater than 3 K. Data for which there is no temperature inversion or the intensity is equal to or smaller than 3 K are plotted in teal. The two conditions show similar trends. Under dry conditions (PW is smaller than 10 mm), the average CRE with the temperature inversion is smaller than that with no inversion, although there is large variation in the values.

According to the Stefan-Boltzmann law, blackbody radiative emission is proportional to the fourth power of absolute temperature. L_D empirically exhibits more dependence on air temperature than is accounted for by this law; for example, Swinbank (1963) suggests that the flux is proportional to the sixth power of T_S. The reason for the strong temperature effect is that an increase in air temperature causes an increase in WV pressure at the surface, and thus an exponential increase in the column WV amount (Deacon, 1970). King (1996) showed that empirical parameterization at the Arctic yielded L_D at the surface proportional to the fourth power of air temperature or to the sixth power of cloud-base temperature. In polar regions, strong temperature inversions appear frequently because of the ice-covered surface. The inversion layer is strongest in winter, when the layer is sometimes warmer than the surface air by 30 K, and this affects the radiation budget (Phillpot and Zillman, 1970; Stone, 1993; Curry et al., 1996). The frequent occurrence of negative CRC values in the present study is attributed to the absorption of radiation from an upper-air temperature inversion owing to clouds.

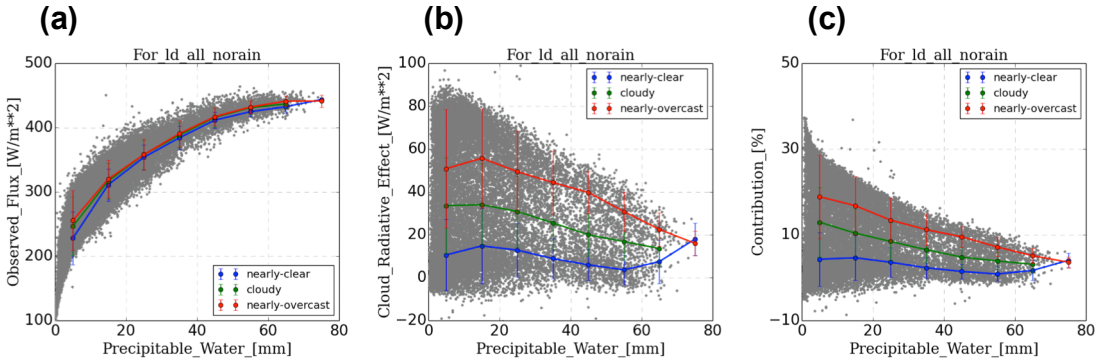

Figure 3.16. Relationship between PW and (a) L_D, (b) CRE, and (c) CRC under nearly clear (SDI < 0.5), cloudy (0.5 ≤ SDI < 0.9), and overcast (SDI ≥ 0.9) conditions.

Figure 3.16 shows the variations of observed L_D, CRE, and CRC as a function of PW under nearly clear (SDI < 0.5), cloudy (0.5 ≤ SDI < 0.9), and nearly overcast (SDI ≥ 0.9) conditions. Under nearly clear conditions, the average CRC (average of ±5 mm of PW every 10 mm) is near 0%. The scatterplot shows low dispersion, except in dry regions with PW of less than 10 mm. In contrast, average CRC under overcast conditions is large and roughly inverse to PW. Under cloudy conditions, CRC lies between these two extremes; the scatterplot shows a large dispersion from dry to wet climates. The distribution of data in present study is different from that in Stephens et al. (2012). They reported that CRE was scattered from -10 to 70 W m^{-2}, whereas we found that CRE was scattered from -20 to 90 W m^{-2}. In addition, they found that CRE was concentrated in a narrow curved band. In contrast, we found that CRE was scattered widely, instead of being concentrated. However, in Figure 3.15, the distribution of CRE under overcast conditions is similar to that reported by Stephens et al., although we observed a higher maximum value. This indicates that the A-Train product cannot detect clouds under nearly clear conditions and misses the effect of small clouds.

L_D is susceptible to local conditions. The small CRC when PW is 10 mm, reported by Stephens et al. (2012) is ascribed to the difficulty of observing the near-surface atmosphere with a satellite when cloud cover is present, because of the coarse spatial and temporal resolutions. Yamamoto and

Sasamori (1954) showed that 80% of L_D is emitted from WV below at pressures below 900 hPa; this finding was based on radiation chart data for Sendai, Japan. Philipona et al. (2004) calculated downward longwave flux with the MODTRAN software package (Version 4.2; Berk et al., 1989) for data from PAY, Switzerland. They found that more than 90% of L_D is emitted from the atmosphere below 1000 m and 39% is emitted from the atmosphere below 10 m. It is difficult for satellite observations to retrieve near-surface WV distribution, which has a disproportionately large effect on L_D.

The LIN and GVN stations measure CBH with ceilometers. NYA and GVN have micro pulse lidar. The SAP and TAT stations use Mie lidar instruments to measure CBH. In this section, we focus on data from these six stations to estimate the effect of CBH on the surface L_D. Because estimated errors in CBH are large for high-altitude clouds, data showing CBH higher than 10 km are discarded. Because the height range of the LD-WHX ceilometer in GVN is limited to 3600 m, GVN does not detect high cloud.

Figure 3.17 shows the variations in observed L_D, CRE, and CRC as a function of CBH at the six sites. CRE and CRC (averaged per 1000 m height) show generally inverse correlations with CBH, as expected. The decreasing trends are reliable at the 95% confidence level. Cloud effect varies widely because of other forcing parameters such as SDI or PW. For low clouds (CBH < 2000 m), the cloud effect is different among the six sites. CRE decreases with increasing CBH at almost all stations with CBH below 4000 m, although TAT shows a small change in CRE and an increase of CRC with increasing CBH below 2000 m.

Figure 3.18 shows the dependences of observed L_D, CRE, and CRC on CBH under nearly clear (SDI < 0.5), cloudy (0.5 ≤ SDI < 0.9), and nearly overcast (SDI ≥ 0.9) conditions. Under nearly clear conditions, the effect of CBH is large in LIN, NYA, SYO, and GVN. These stations show decreases in CRE and CRC with increasing CBH for low or middle clouds (CBH < 6 km). In contrast, SAP and TAT show a small CBH effect. Because these east Asian stations have a larger PW than other regions, the effect of CBH variation is smaller. Increasing amounts of cloud lead to the wide dispersion

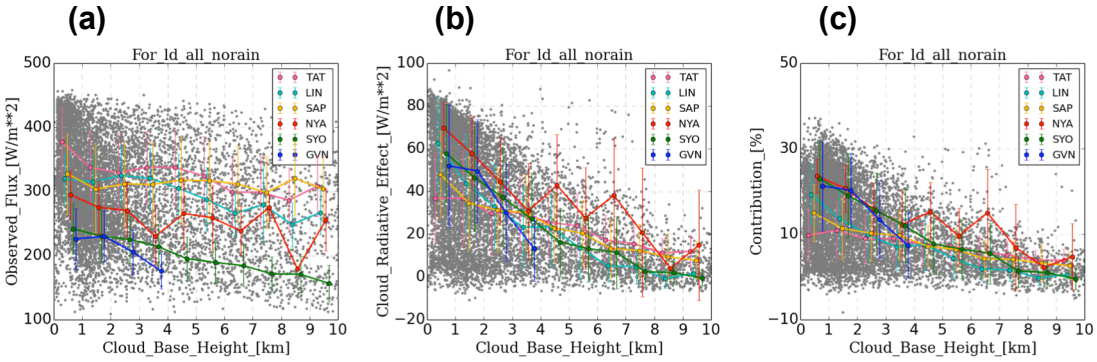

Figure 3.17. Relationship between CBH and (a) L_D, (b) CRE, and (c) CRC at TAT (pink), LIN (teal), SAP (yellow), NYA (red), SYO (green), and GVN (blue).

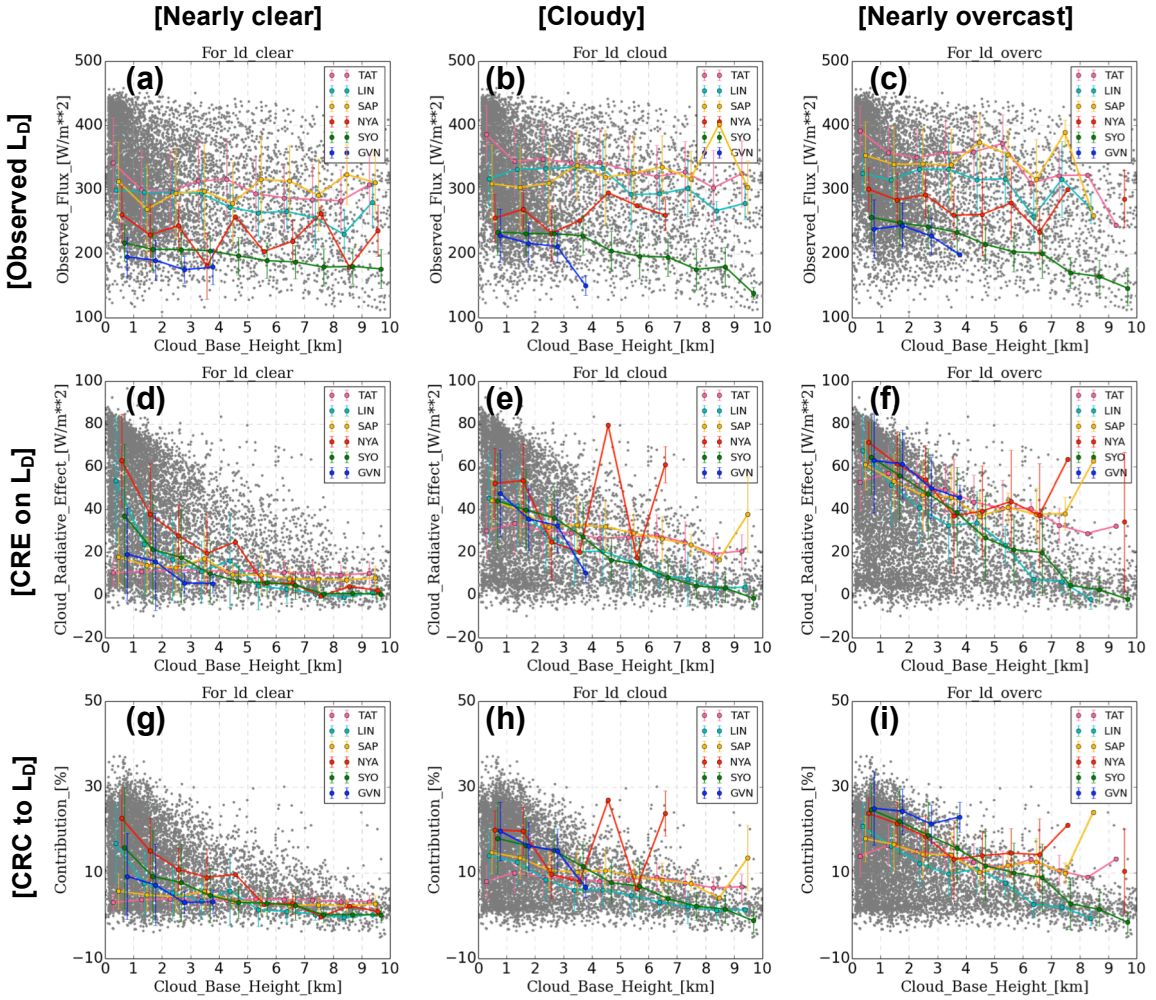

Figure 3.18. Relationships between CBH and (a–c) L_D, (d–f) CRE, and (g–i) CRC under (a), (d), (g) nearly clear (SDI < 0.5), (b), (e), (h) cloudy (0.9 > SDI ≧ 0.5), and (c), (f), (i) nearly overcast (SDI ≧ 0.9) conditions.

of CRE and CRC. Under cloudy and nearly overcast conditions, CRE and CRC generally decrease with increasing CBH from the surface to 6 km. The decreases are reliable at the 95% confidence level except for TAT, which has a small radiative effect for cloud below 1000 m, and NYA, which has a small frequency for middle-high cloud. High clouds are difficult to detect with lidar because of attenuation of the laser; therefore, the standard deviation of CRC for high cloud is large. Decreasing the radiative effect in TAT below 2000 m is the same as under all-sky conditions, which is contrary to the expectation that CRE should decrease with decreasing CBH.

Figure 3.19 shows the joint frequencies of the annual mean and seasonal variation of the relationship between CBH and CRC to L_D at GVN, LIN, NYA, SAP, SYO, and TAT. When CBH is low, low clouds are dominant at all stations for the annual mean (Figure 3.19.a). Large CRC occurs frequently at GVN, LIN, NYA, and SYO. When large CRC and low CBH have a high joint frequency, an inverse relationship between CBH and CRC is reasonable because of the gradual decrease in temperature with increasing altitude. In contrast, annual mean CRC is often both small and large at SAP and TAT stations. The low joint frequency of high CRC and low CBH weakens the inverse relationship between CBH and CRC, resulting in a directly proportional relationship.

Figure 3.19.b–e show seasonal variations in the relationship between CBH and CRE. Seasonal variations at LIN, NYA, SYO, and GVN are small. The bimodal characteristic may be caused by the distribution of the cloud fraction, which affects cloud effects directly. Generally, the distribution of cloud fraction is U-shaped rather than Gaussian, and the frequencies of very small and very large cloud fractions are high (Hogan et al., 2001, 2009).

At SAP and TAT, the joint distribution of CBH and CRC varies dramatically by season. High clouds are more frequent than low clouds during spring and summer at SAP and during autumn at TAT. During autumn and winter at SAP, low clouds occur frequently, although the distribution of CRC differs during spring and summer. The incidences of low clouds with small CRC and low clouds with high CRE are approximately the same.

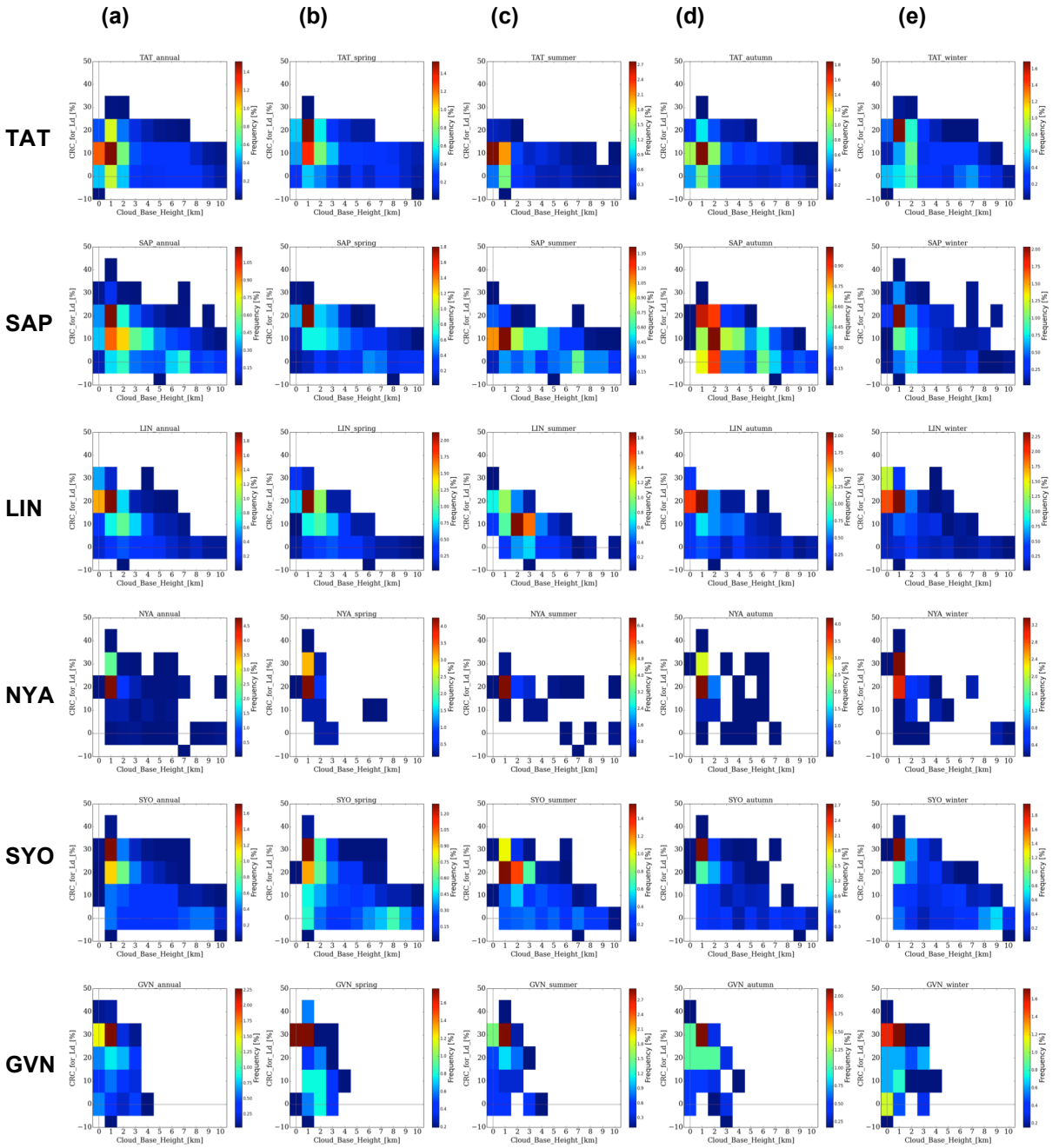

Figure 3.19. 2D CBH-CRC histogram against L_D for (a) annual, (b) spring, (c) summer, (d) autumn, and (c) winter measurements.

The relationship between CBH and CRC at TAT during summer and winter is different from the other stations and seasons. During summer, near-surface clouds (CBH < 1000 m) dominate and it is hard to detect clouds at other altitudes. The incidence of low clouds is high for CRC from near 0 to 70%. The incidence of clouds with low or middle altitude is high during

winter. In Figure 3.17, the annual average of CRE at TAT increases with increasing CBH when CBH is less than 2 km. This is attributed to the unusual relationship between CBH and CRE during summer and winter at TAT.

There is a positive correlation between CBH and CRC at TAT for low clouds. Because low clouds can be treated as an optically thick black body, and the positive correlation is not attributed to the effect of cloud properties (e.g., cloud optical depth or liquid water path) but to atmospheric moisture conditions.

Figure 3.20 shows the joint frequencies of CBH and PW at four stations for annual averages (Figure 3.20.a) and by season (Figures 3.20.b–e). At LIN, SAP, and TAT, clouds with CBH of less than 2000 m occur more frequently than any other type. Only NYA has high incidences of both low and high clouds. At LIN and NYA, 0 to 1000 m clouds are more frequent than 1000 to 2000 m clouds, whereas at SAP and TAT, 1000 to 2000 m cloud is more frequent than 0 to 1000 m cloud. This difference may account for the difference in cloud height seasonal characteristics among stations.

Although a high incidence of only low clouds is obtained for all seasons at LIN, the frequency distributions can be classified into two types. During autumn and winter, the CBH below 1000 m dominates. Compared with near-surface clouds, CBH in the 1000 to 2000 m range is more frequent during spring and summer.

At NYA, the relationship between PW and CBH is consistent throughout the year: low clouds occur frequently; during spring and autumn, high clouds with small PW occur slightly more often, as expected from the relationship between CRE and CBH. At SAP, the joint frequency between PW and CBH shows large seasonal variation. Middle- and high-altitude clouds are found frequently in spring and summer, similar to NYA during spring and autumn. In summer, high clouds appear more frequently than low clouds do. During autumn, low-altitude clouds appear during dry conditions, similar to the pattern at LIN. In winter, most clouds are detected below 2000 m and under dry conditions.

At TAT, the joint frequency between CBH and PW shows large seasonal

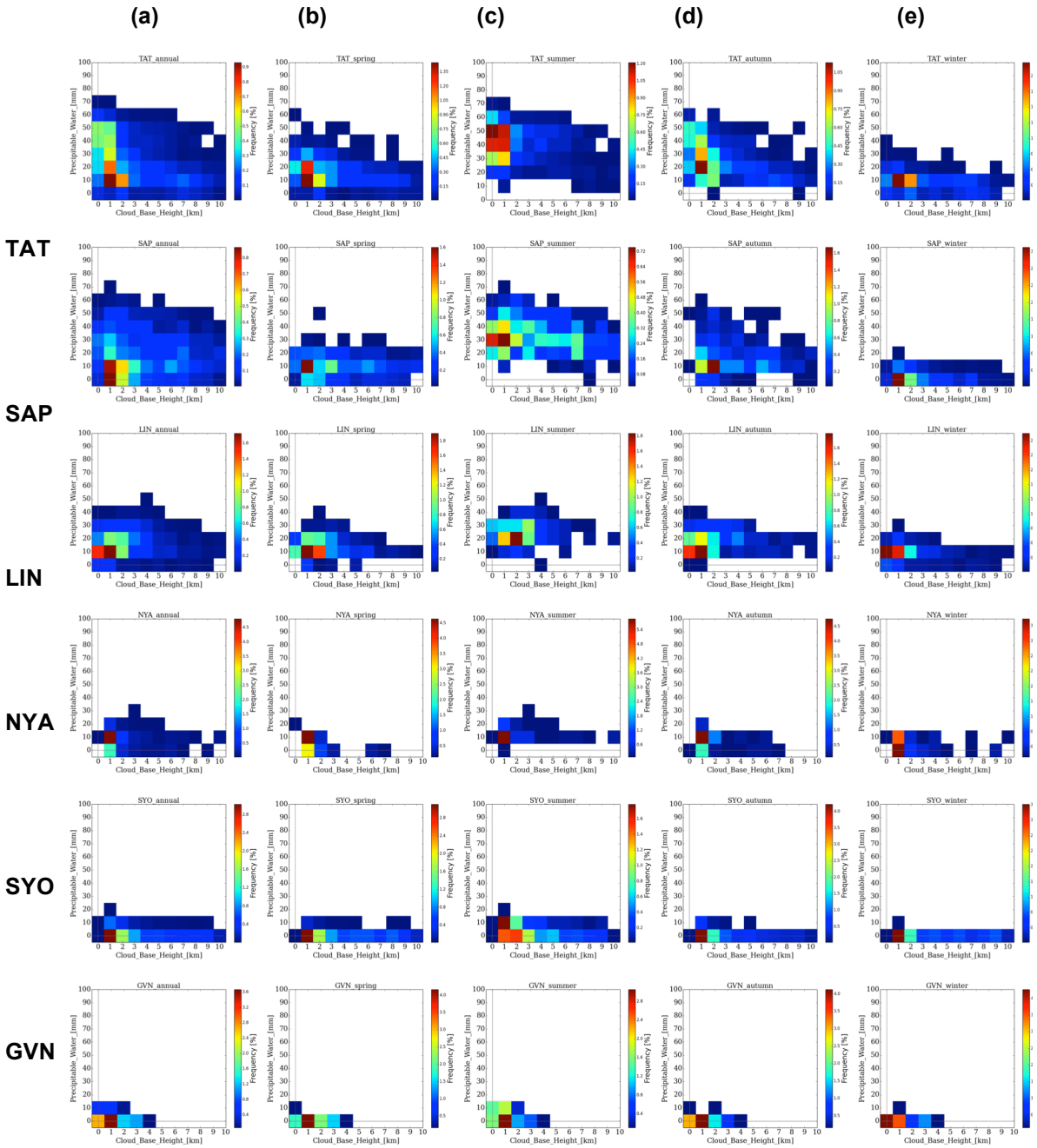

Figure 3.20. 2D CBH-PW histogram for (a) annual, (b) spring, (c) summer, (d) autumn, and (e) winter measurements.

variation. During spring, the incidence of low clouds is high, similar to all seasons at LIN and autumn at SAP. In summer, the incidence of near-surface clouds is high for PW from 20 to 60 mm. An incidence peak is observed under wet conditions. Both high and low clouds occur frequently at TAT during autumn, similar to NYA for spring and autumn and SAP for

spring and summer. When high clouds are present, PW is lower than when low clouds are present. One aspect of the joint frequency between CBH and PW at TAT is unusual for winter: although low clouds and low PW frequently co-occur at other stations and seasons, clouds of all heights frequently occur under dry conditions at TAT (Yamada et al., 2014).

Because TAT is located on the Pacific Ocean side of Japan and is affected by the East Asian monsoon, the wind direction changes with the season determining atmospheric conditions and cloud characteristics (Jhun and Lee, 2004; Hirano and Matsumoto, 2010; Wang and Ho, 2002). Figure 3.21 shows the relationship between CBH and surface wind direction at TAT for summer and winter from radiosonde observation data. During summer, the monsoon forms the Baiu Front, which causes heavy clouds and frequent rainfall on the Pacific Ocean side of the island, where TAT is situated. Figure 3.21.a shows frequent northeastern and southern winds, and near-surface clouds occur frequently regardless of wind direction.

In contrast to summer, the winter monsoon season causes heavy snowfall on the Japan Sea side of Japan, whereas the Pacific Ocean side of Japan is dry with low precipitation. This occurs because the mountains that extend from north to south in the center of Honshu Island, Japan, block humid winds. Figure 3.21.b shows that two wind directions frequently co-occur with clouds. When the wind direction is northern or northeastern, only low clouds occur frequently. When the wind direction is western or northwestern, clouds at all heights occur frequently. These results indicate that wind direction corresponds to atmospheric conditions and affects the incidence of clouds. This relationship is particularly strong during winter.

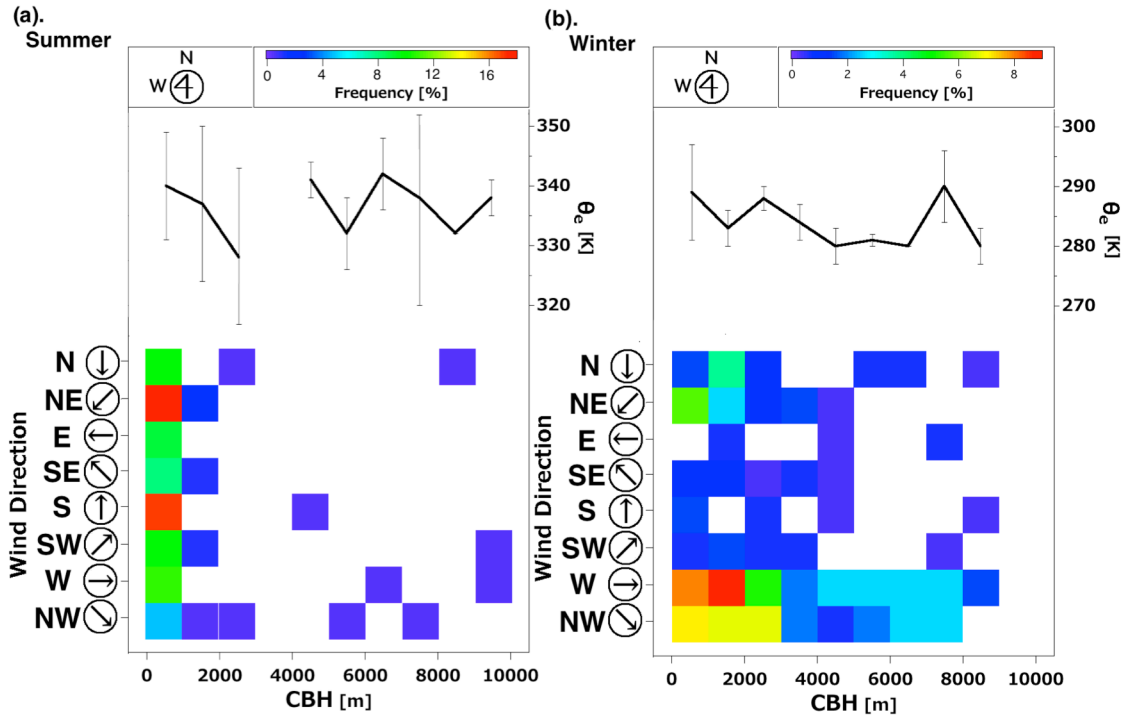

Figure 3.21. Joint frequencies between CBH and surface wind direction at TAT for (a) summer and (b) winter (from Yamada et al., 2014).

3.2 Shortwave

3.2.1 Clear-sky

Figure 3.22 shows the variation of S_D with PW and the cosine of SZA under clear-sky conditions. SZA is the dominant factor determining S_D at the surface. Figure 3.22.a shows a strong relationship between the cosine of SZA and S_D. The amount of WV, which has wide absorption band for L_D and S_D, also has an effect on S_D. The polar and desert regions, which contain less WV, have a larger S_D than mid-latitude and polar regions with the same SZA.

Figure 3.23 shows the variations in the radiative contributions of WV, aerosols, and the surface albedo to S_D calculated by the removal method compared with PW and the cosine of SZA under clear-sky conditions. To prevent a large cosine error, the contribution to S_D is calculated only with SZA below 80°. Under clear-sky conditions, the dependence of the contribution to S_D on SZA is small. Most (95% from the median) REM_{WV}, $REM_{Aerosol}$, and REM_{Albedo} values range from +3 to +29%, -4 to +24%, and -11 to +16%, respectively. The contribution of WV to S_D is larger than that from aerosols by 5 to 7%.

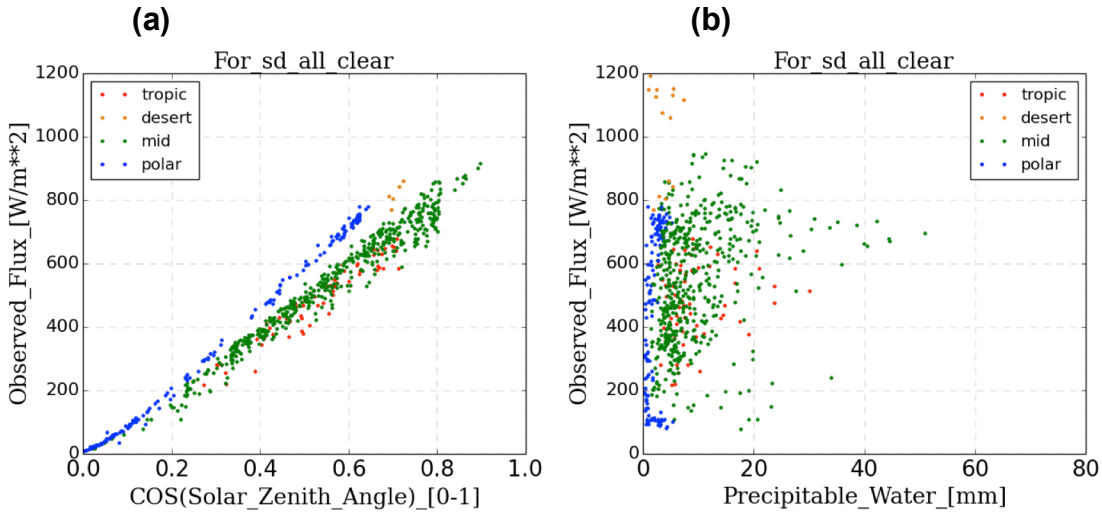

Figure 3.22. Relationship between S_D and (a) the cosine of SZA and (b) PW under clear-sky conditions.

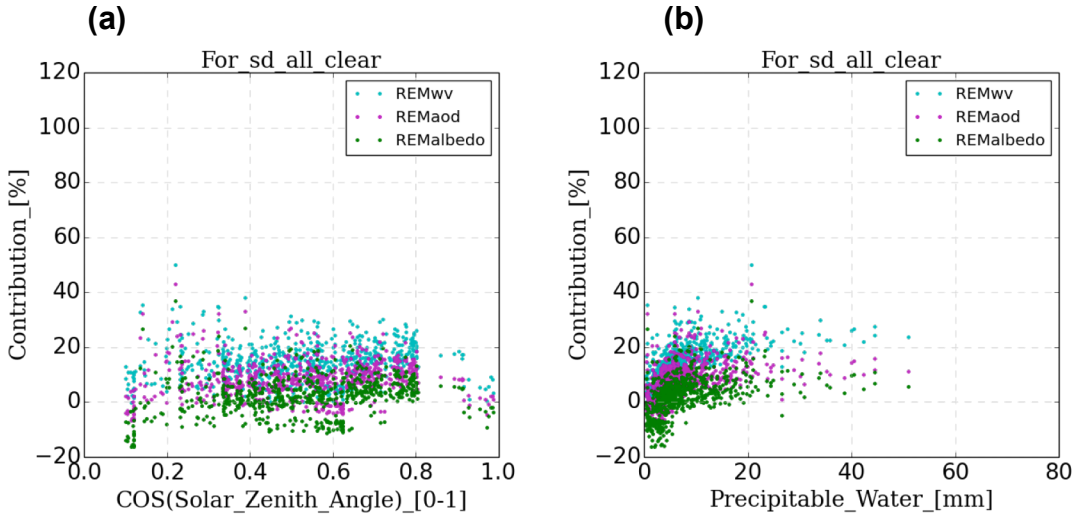

Figure 3.23. Relationship between contributions to S_D and (a) PW and (b) SZA under clear-sky conditions. Teal, magenta, and green indicate REM_{WV}, $REM_{Aerosol}$, and REM_{Albedo}, respectively (only with the cosine of SZA > 0.1).

The radiative contribution of albedo to S_D reaches up to -10%, which means that the albedo effects cause more downward radiation because of the multiple scattering between a snow or ice surface and the atmosphere or aerosols. The relationship between PW and REM_{Albedo} (Figure 3.23.b) shows that the large negative REM_{Albedo} contribution to S_D occurs only in the polar region with PW less than 5 mm. However, the large albedo increases upward radiation and does not contribute to heating the surface because most of the radiation is reflected by the albedo.

3.2.2 All-sky

Radiative transfer calculations for overcast conditions are problematic because of the difficulty in estimating cloud optical properties corresponding to observations. In this section, the CRC, which is equal to the REM_{Cloud} contribution to S_D, is estimated under all-sky conditions with no precipitation.

Figure 3.24 shows the relationships between SDI and S_D, CRE, and CRC

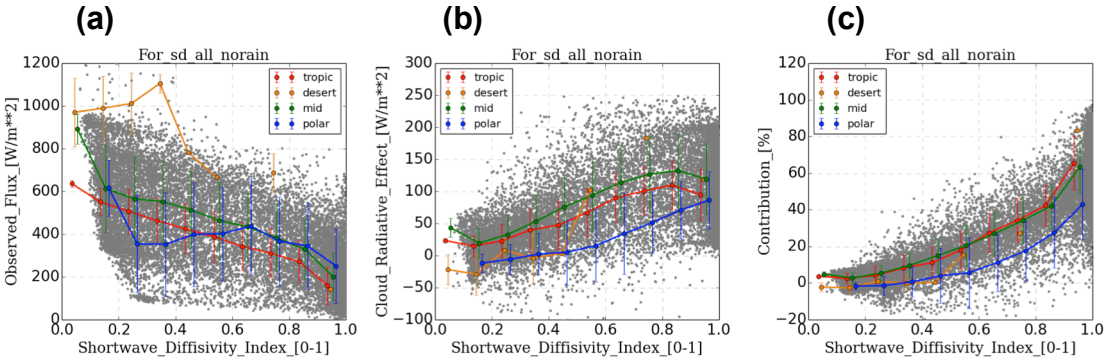

Figure 3.24. Relationship between SDI and (a) S_D, (b) CRE, and (c) CRC under all-sky conditions. Red, orange, green, blue lines indicate sub-tropical, desert, mid-latitude, and polar regions, respectively.

under all-sky conditions (no rain and only the cosine of SZA is larger than 0.1). In sub-tropical and mid-latitude regions, the observed fluxes are correlated with the SDI. The polar regions have a small S_D with an SDI of 0.3 to 0.6 because of the large SZA. The variation of S_D in polar regions is different compared with the other regions, because the polar regions rarely have cloud and the frequency of SDI larger than 0.2 is small. Except for desert regions, the averages of CRE and CRC show a strong relationship with SDI. CRC (95% from the median) varies from −5 to + 85%. The CRC has a larger effect on S_D than on L_D (from −2 to +28%) for a large SDI.

Figure 3.24.c shows that CRC in polar regions is smaller than in sub-tropical and mid-latitude regions by 10 to 20% at the same SDI. The averages of S_D with SDI from 0.7 to 0.9 are similar between mid-latitude and polar regions (Figure 3.24.a, b). CRE in polar regions is 30 to 50 W m^{-2} smaller than in mid-latitude regions. Therefore, CRC in the polar regions is smallest because of the smaller effect of cloud at the same SDI.

The other reason for the small CRC in the polar regions is the difference in scattering factors, namely WV or aerosols. Figure 3.25 shows the relationships between the cosine of SZA and S_D, CRE, and CRC. At the same SZA from 0.5 to 0.9, polar regions have a CRC 10 to 20% smaller than sub-tropical and mid-latitude regions. The difference is caused by the observed S_D (Figure 3.25.a) instead of CRE (Figure 3.25.b). Under the dry,

clear atmosphere in the polar regions, the larger S_D decreases CRC.

Figure 3.26 shows the relationships between SZA and S_D, CRE, and CRC under nearly clear, cloudy, and nearly overcast conditions. The average S_D shows a strong relationship with SZA, and the differences among the three SDI conditions increase as SZA decreases (Figure 3.26.a). There are small differences in average CRE under cloudy and nearly overcast conditions. Only the average for nearly clear conditions is smaller than those of the other conditions by 25 to 100 W m^{-2} at SZA from 0.2 to 0.8. Both S_D and

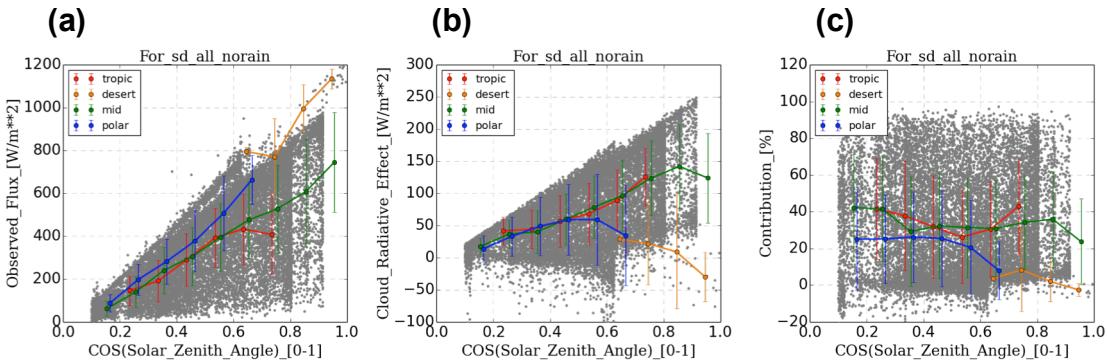

Figure 3.25. Relationships between SZA and (a) S_D, (b) CRE, and (c) CRC. Red, orange, green, blue lines indicate sub-tropical, desert, mid-latitude, and polar regions, respectively.

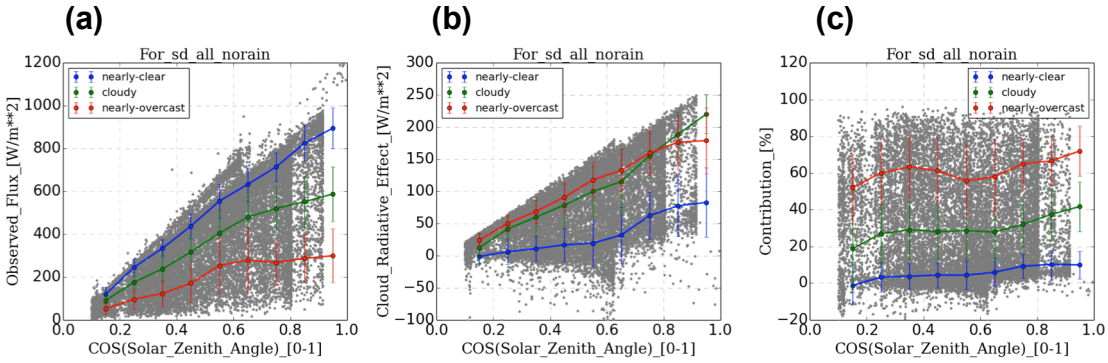

Figure 3.26. Relationship between SZA and (a) S_D, (b) CRE, and (c) CRC under nearly clear (SDI < 0.5), cloudy (0.5 ≤ SDI < 0.9), and near-overcast (SDI ≥ 0.9) conditions.

CRE correspond to SZA, and there is small dependency of CRC and S_D on SZA. The averages of CRC under nearly clear, cloudy, and nearly overcast conditions are 0 to 10%, 20 to 40%, and 50 to 70%, respectively.

The relationship between CBH estimated by active sensors and S_D, CRE, and CRC at six observatories is shown in Figure 3.27. GVN detects CBH only below 3600 m because of the ceilometer range. The averages of CRC with CBH (average CBH of ±500 m every 1 km) are different between stations. The average CRC at all stations except GVN and SAP decreases with increasing CBH because optically thinner clouds are more frequently middle or high clouds than low cloud. NYA shows large variability above 3 km, similar to the CRC to S_D, because of the small frequencies of middle or high cloud at NYA. The average at GVN with CBH from 0 to 3 km does not increase with increasing CBH.

The relationships under three SDI conditions are shown in Figure 3.28. Nearly clear conditions show a small average effect and variability at all stations. Cloudy and near-overcast conditions show small variability in average CRC.

Figure 3.29 shows the joint frequencies of the annual mean and seasonal variation of the relationship between CBH and CRC at GVN, LIN, NYA, SAP, SYO, and TAT. For the annual average, all stations show large

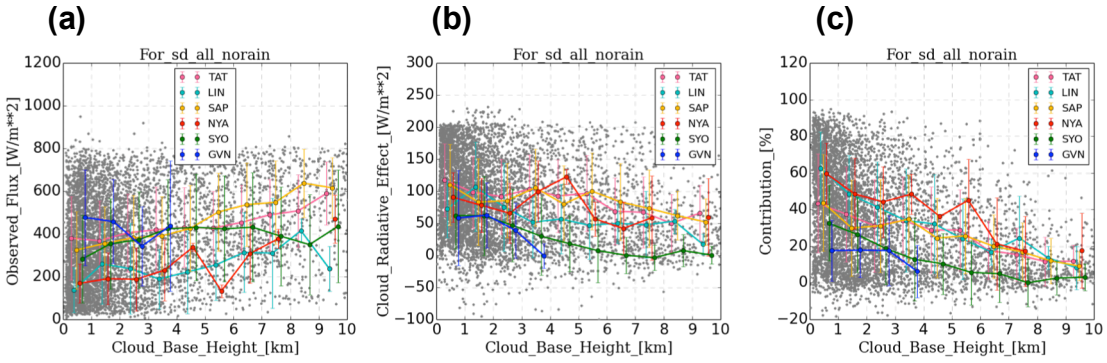

Figure 3.27. Relationship between CBH measured with active sensors and (a) S_D, (b) CRE, and (c) CRC at TAT (pink), LIN (teal), SAP (yellow), NYA (red), SYO (green), and GVN (blue).

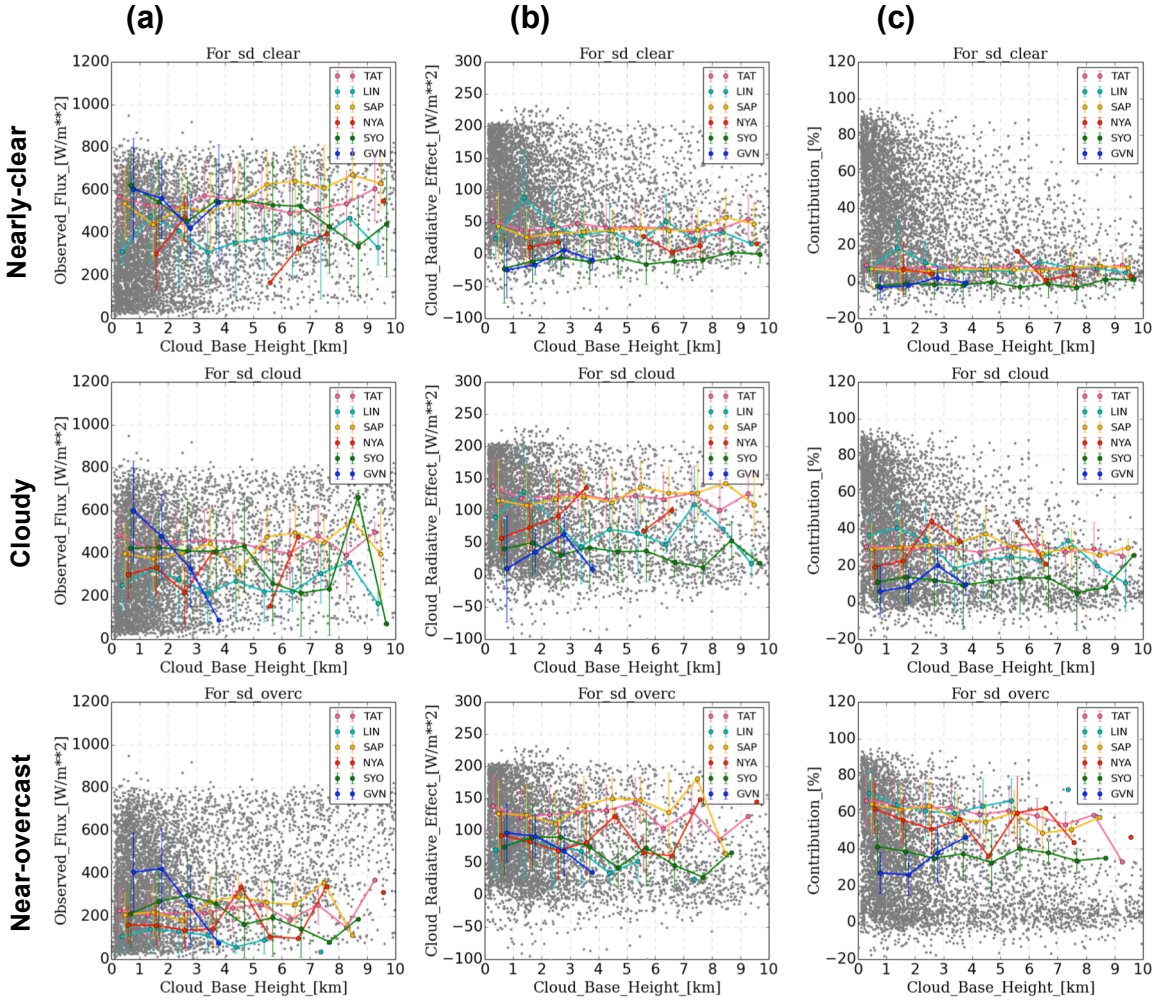

Figure 3.28. Relationship between CBH and (a) S_D, (b) CRE, and (c) CRC under nearly clear (SDI < 0.5; upper), cloudy (0.5 ≤ SDI < 0.9; middle), and overcast (SDI ≥ 0.9; lower) conditions at TAT (pink), LIN (teal), SAP (yellow), NYA (red), SYO (green), and GVN (blue).

frequencies of low-cloud, and, except for SYO, show small to large CRC. SYO shows only a small CRC to S_D, in contrast to the CRC to L_D. GVN, which shows small variability in CBH from 0 to 3000 m, shows large frequencies for 1000 to 2000 m, mainly during summer.

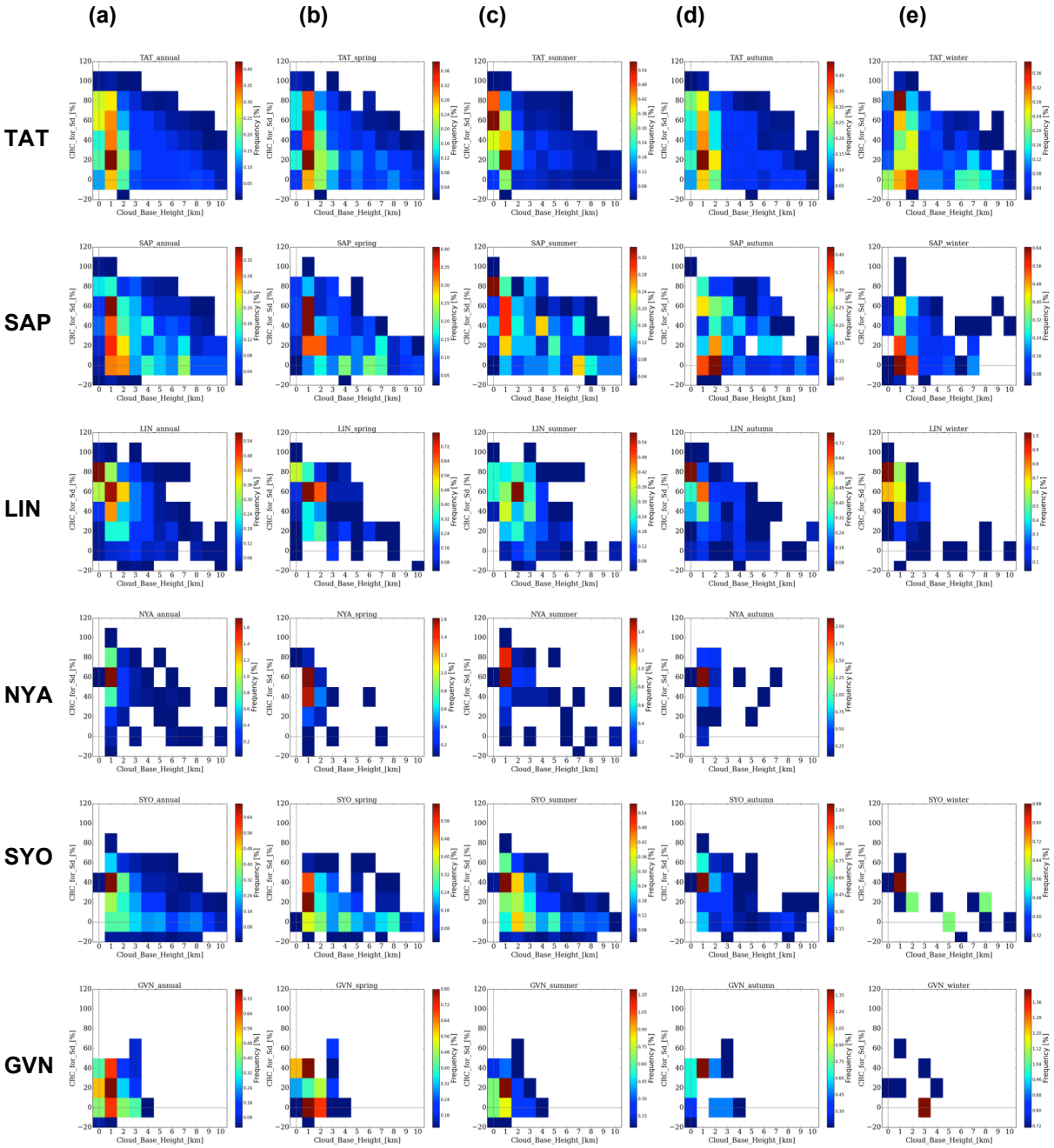

Figure 3.29. 2D CBH-CRC histogram for S_D for (a) annual, (b) spring, (c) summer, (d) autumn, and (e) winter averages.

3.3 Total

In this section, we evaluate the effect of CRC on total downward radiation (T_D) under all-sky conditions without precipitation. CRC is defined as affecting T_D when the radiative contribution to the surface radiation budget is positive. Figure 3.30 shows the variations of T_D, CRE, and CRC as a function of the cosine of SZA. Observed T_D shows a strong correlation with SZA, controlling S_D during the day (the cosine of SZA is smaller than 0) and reaches over 1500 W m^{-2}. CRE and CRC during the day show a positive correlation for SZA larger than 0.5. At small SZA, the cloud effects in sub-tropical or mid-latitude are different from in desert or polar regions, as for S_D (Figure 3.25). This is caused by the effect of shortwave radiation. At night, the effect of shortwave radiation is ignored and CRC is largest in polar regions. Values 95% from the median of CRC to T_D range from -71 to +27%.

Figure 3.31 shows the relationship between SDI and T_D, CRE, and CRC during the day. The variation of average T_D with SDI in the mid-latitude and sub-tropical regions are similar because sub-tropical regions have a slightly smaller S_D and larger L_D than mid-latitude regions. CRE and CRC are also similar for the sub-tropical and mid-latitude regions because of the observed flux. The averages of radiation and cloud contribution show a negative correlation with SDI. The average of CRC in polar regions is positive except for SDI larger than 0.9, and cloud warms the surface in polar regions except

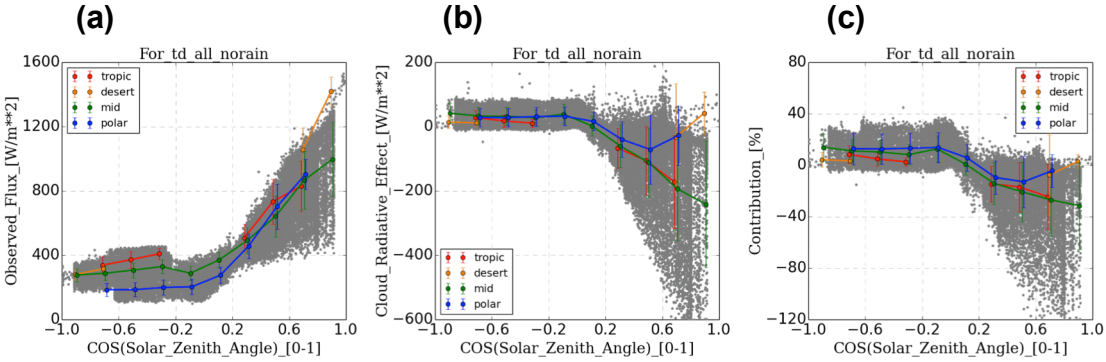

Figure 3.30. Relationship between the cosine of SZA and (a) T_D, (b) CRE, and (b) CRC. Red, orange, green, and blue lines indicate sub-tropical, desert, mid-latitude, and polar regions, respectively.

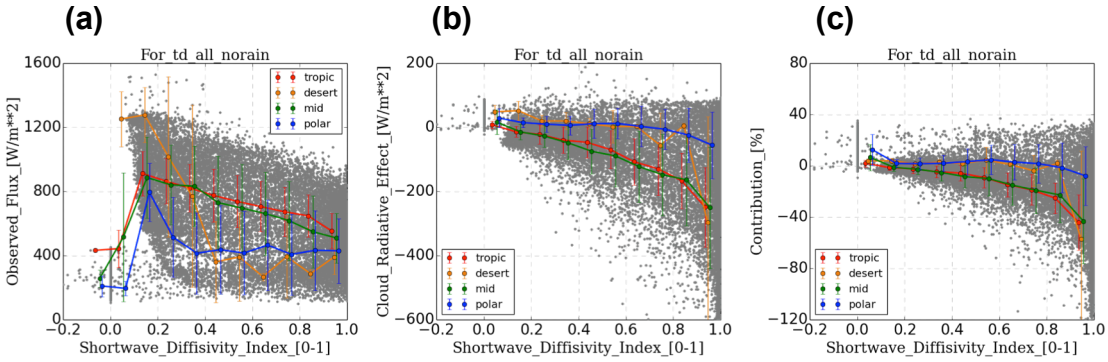

Figure 3.31. Relationship between SDI and (a) T_D, (b) CRE, and (c) CRC under all-sky conditions. Red, orange, green, blue lines indicate sub-tropical, desert, mid-latitude, and polar regions, respectively.

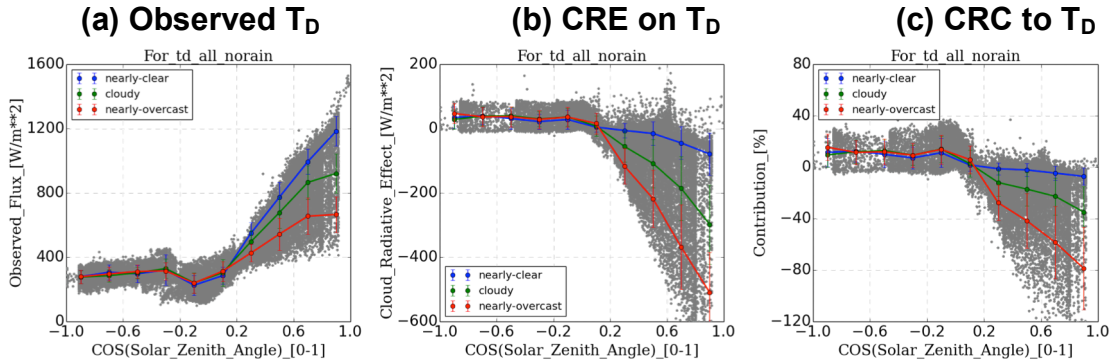

Figure 3.32. Relationships between SZA and T_D, the CRE, and CRC under nearly clear (SDI < 0.5), cloudy (0.5 ≤ SDI < 0.9), and overcast (SDI ≥ 0.9) conditions.

for nearly overcast conditions. However, the averages of CRC in mid-latitude and sub-tropical regions are negative with SDI larger than 0.1 and make the surface cool in daytime. Desert regions have the least amount of cloud with CRC averages of near 0%.

Figure 3.32 shows the relationship between the cosine of SZA and T_D, CRE, and CRC for SDI of nearly clear (SDI < 0.5), cloud (0.9 > SDI ≥ 0.5), and nearly overcast (SDI ≥ 0.9) conditions. The difference in T_D is approximately 300 W m^{-2} among the three SDI conditions during the day. The three SDI types at night (cosine of SZA < 0) show a much smaller difference than during the day. Under nearly clear conditions, the contributions of cloud to L_D and S_D are small and the daytime averages of CRC are around 5% even for SZA smaller than 0.2, and the absolute CRC value is smaller than the

average during the day. Under cloudy or nearly overcast conditions, the effect of shortwave radiation is greater and the CRC to T_D is larger than -10% with SZA larger than 0.6 during the day.

The relationship between CBH estimated by active sensors and T_D, CRE, and CRC during the day and night is shown in Figure 3.33. Because the CRC to L_D and S_D decreases with increasing CBH, the CRC to T_D has small variations in the averages of all SDI conditions.

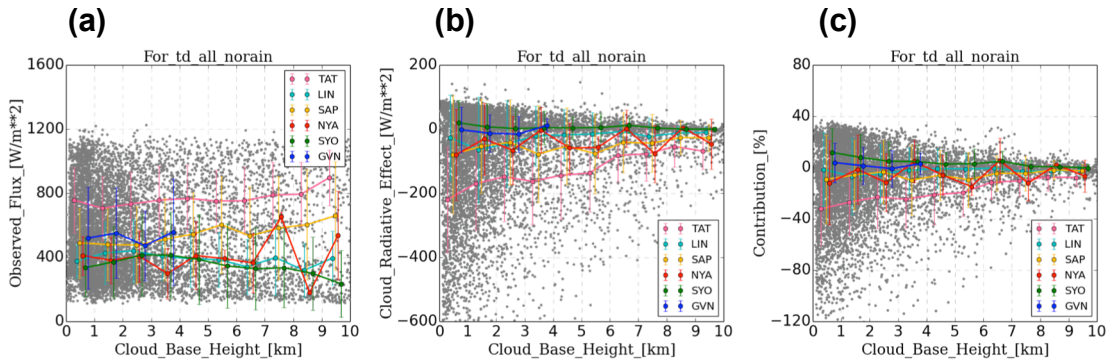

Figure 3.33. Relationships between CBH and (a) T_D, (b) CRE, and (c) CRC at TAT (pink), LIN (teal), SAP (yellow), NYA (red), SYO (green), and GVN (blue).

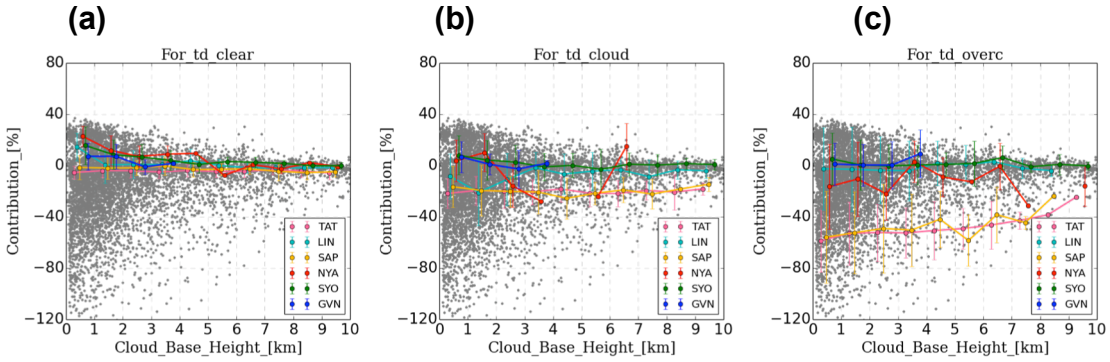

Figure 3.34. Daytime relationships between CBH and CRC under (a) nearly clear (0.0 < SDI < 0.5), (b) cloudy (0.5 ≤ SDI < 0.9), and (c) overcast (SDI ≥ 0.9) conditions at TAT (pink), LIN (teal), SAP (yellow), NYA (red), SYO (green), and GVN (blue).

The relationships between CBH and CRC during the day under nearly clear, cloudy, and nearly overcast conditions are shown in Figure 3.34. Except for TAT and SAP, which show a large contribution of cloud to S_D, the averages of CRC to T_D are positive and generally show a negative correlation with CBH below 4 km under nearly clear conditions. Increasing SDI decreases the strength of the correlation. Under near-overcast conditions, the averages of CRC are approximately constant with CBH except at NYA, which shows large variability.

In summary, for cloud under all-sky conditions, the effect of cloud warming on L_D and cloud cooling on S_D cancel each other, and sub-tropical and mid-latitude regions show large cooling effect and a similar CRC during the day. However, the warming effect is larger in polar and desert regions. The difference in SDI is an important factor in the average of all regions. Although CBH has a large effect on L_D and CRC even under nearly clear conditions, S_D is hardly affected by CBH.

Chapter 4

Inter-annual Variation

In this chapter, we discuss the inter-annual variations of the surface radiative fluxes, cloud, and radiative contributions of cloud at the BSRN stations that have observation periods longer than 10 years. The target stations are classified into four regions: mid-latitude continental (Lindenberg (LIN) and Payerne (PAY)), desert (Tamanrasset (TAM)), Arctic coastal (Ny-Ålesund (NYA)), Antarctic coastal (Georg von Neumayer Station (GVN) and Syowa (SYO)), and East Asia (Tateno (TAT)).

We evaluate trends in the monthly mean. The seasonal cycle is removed by subtracting the mean seasonal difference in observational periods from the monthly mean. The monthly mean value is calculated from daily averages. The daily mean observations, such as air temperature or downward radiation, are calculated from hourly mean values. The daily mean values of radiative transfer cannot be calculated directly because of the limited number of radiosonde observations. The daily mean is estimated by averaging 24 calculations obtained by adjusting for the amount of water vapor (WV) and air temperature in the troposphere by using the difference in air temperature and RH between the target time and radiosonde time. All trends are tested by the Mann-Kendall rank correlation test (Mann, 1945; Kendall, 1948) after seasonal correction. To reduce the effect of seasonal changes, the percentage increase or decrease and the trend are calculated after seasonal correction, which is performed by subtracting the monthly averages. In this chapter, reliable increasing or reliable decreasing trends are defined as having variation that satisfies the 95% confidence level tested by the Mann-Kendall trend test.

4.1 Mid-latitude region

4.1.1 Seasonal cycles in the mid-latitude region

Figure 4.1 shows seasonal cycles of the surface downward longwave radiation (L_D), downward shortwave radiation (S_D), downward total radiation (T_D), surface air temperature (T_S), precipitable water (PW), and visually observed total cloud fraction (CF_{Total}) at LIN from 1994 to 2007, PAY from 1996 to 2007, and TAT from 1997 to 2014. There are small differences in surface downward radiation between at LIN and PAY, because the locations are close and have similar surface air conditions. Only CF_{Total} at LIN is larger than PAY by 0.1 to 0.2 from February to March and from June to July. The effect of different CF_{Total} on the radiation budget is small. S_D at LIN is smaller than at PAY because PAY is slightly south of LIN.

TAT is on the opposite side of the Asian continent to LIN and PAY. The latitude of the Japanese station is lower than at the two European stations, and T_S is larger by 2 to 10 K. PW at TAT changes considerably because of the effect of the sea breeze during summer. The monthly PW reaches 20 mm for July to August. The humid sea breeze produces wet, cloudy conditions in east of Japan. Cloudy or rainy summer days are called “Baiu”, during which the monthly total cloud cover is up to 0.75 and the S_D becomes smaller than at LIN and PAY.

Figure 4.2 shows CF_{Total} at LIN, PAY, and TAT obtained by lidar or ceilometer, visual observations, radiosonde estimation, 2.5° International Satellite Cloud Climatology Project (ISCCP) FD-SRF product, 1° MODIS L3 Daily Global product, and 1° average 2B-GEOPROF-LIDAR of CloudSat-CALIPSO. The target period at TAT is 2007 to 2009 for comparing CloudSat-CALIPSO, which retrieved clouds from 2007, with others methods. Because in situ visual observation of CF_{Total} at LIN and PAY were taken until 2007, the period of comparison is from 2004 to 2006 at LIN and PAY.

At LIN, the monthly averages of CF_{Total} obtained by all instruments range from 0.5 to 0.9. Except for ISCCP for winter, the estimation methods show similar seasonal cycles; winter is large, and from spring to autumn is small. September is the minimum, which is 0.5 to 0.7. Radiosonde estimates show good agreement with ceilometer estimates. Visual observations are

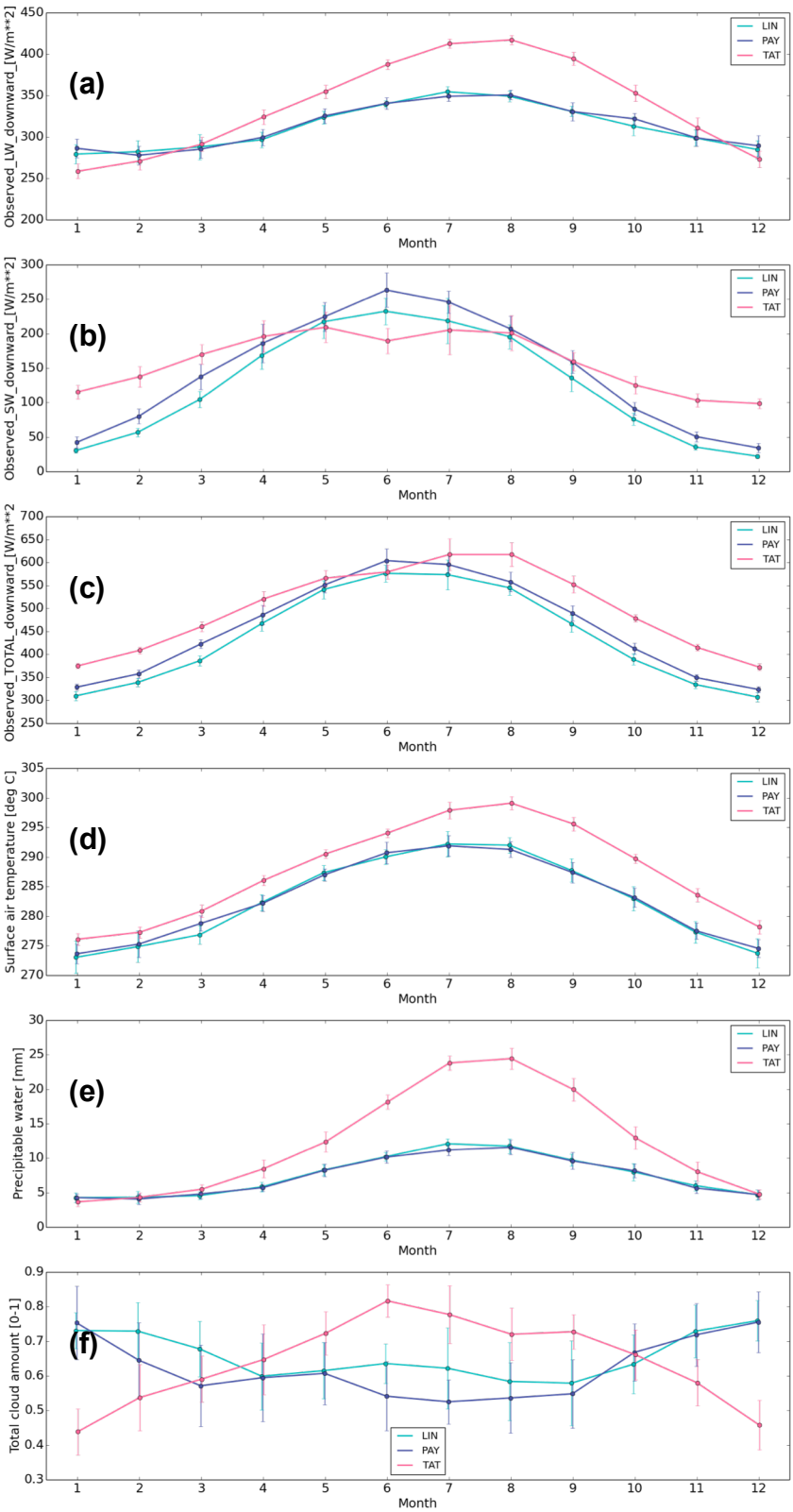

Figure 4.1. Seasonal variations of (a) L_D, (b) S_D, (c) T_D, (d) T_S, (e) PW, and (f) CF_{Total} obtained from visual observations at LIN (teal), PAY (navy), and TAT (pink).

smaller by about 0.1 for all seasons.

The PAY BSRN station has no active sensors such as lidar or ceilometers. Therefore, CF_{Total} is compared for visual, radiosonde, ISCCP, and MODIS observations. Monthly averaged CF_{Total} is 0.4 to 0.8, which is slightly smaller than LIN. CF_{Total} is at a minimum from June to July and at a maximum from December to January except for the ISCCP product. Radiosonde estimates are larger by 0.1 than in situ observations from autumn to winter and smaller by 0.1 for spring. Compared with LIN, the seasonal cycle of CF_{Total} at PAY shows the same maximum CF_{Total} for winter, although the minimum is two or three months earlier. Therefore, although PAY is near LIN, the seasonal cycle of cloud amount is different.

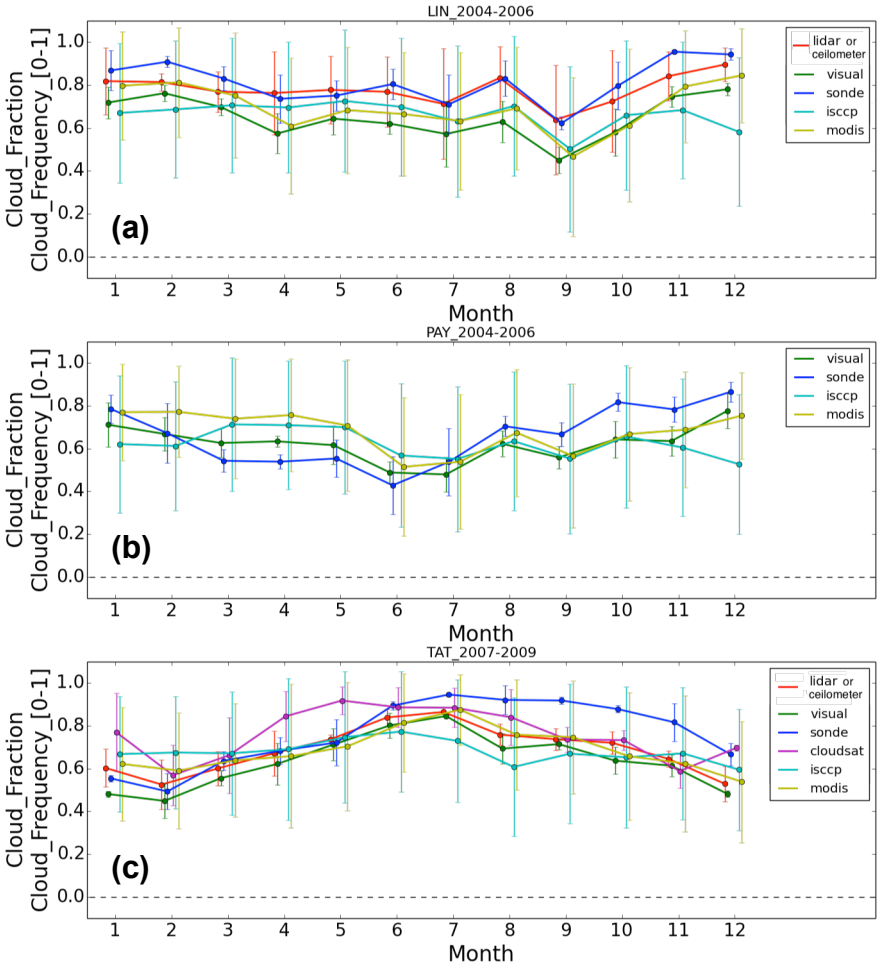

Figure 4.2. CF_{Total} obtained from lidar/ceilometer, visual observation, radiosonde estimation, CloudSat-CALIPSO, ISCCP, and MODIS at (a) LIN and (b) PAY for 2004–2006, and (c) TAT for 2007–2009.

Observations at LIN and PAY do not correspond to those obtained with the other estimation methods from November to October because of the low spatial resolution of ISCCP of 2.5°.

Figure 4.2.c is the seasonal cycle for CF_{Total} at TAT, which is located in the East Asian region. Therefore, the cycle at TAT is different from that at LIN and PAY. The monthly average CF_{Total} reaches its maximum in summer because of the Baiu Front, and reaches its minimum in winter because of the Siberian High. The active Mie-scattering lidar sensor results show good agreement with visual observations. Radiosonde observations overestimate CF_{Total} by 0.1 to 0.2 from June to December compared with lidar observations. The MODIS and lidar measurements agree, whereas CloudSat-CALIPSO measurements are overestimated for spring and ISCCP measurements are underestimated for summer.

In summary, radiosonde estimations of the cloud fraction at LIN show good agreement with lidar measurements. Visual observation underestimates CF_{Total} by 0.1 to 0.2 compared with lidar, although the cycle is similar to lidar. At TAT, visual estimation shows good agreement with lidar measurements. Visual observations and radiosonde estimations are similar at PAY, which has no active sensor. Among satellite retrievals, ISCCP generally corresponds to in situ observations; however, in winter, it underestimates the measurements in the European region and overestimates them at TAT. The CloudSat-CALIPSO 1° averaged result is overestimated for winter to spring over TAT. MODIS estimates are consistent with the in situ observations at TAT, although the estimates at PAY are larger by 0.1 to 0.2 than the visual and radiosonde measurements. The MODIS estimate over LIN is smaller than ceilometer measurements by 0.1. Satellite retrieval has large variability.

Figure 4.3 illustrates fractions of low (CBH is below 2000 m), middle (from 2000 to 6000 m), and high (above 6000 m) clouds estimated by in situ active sensors at LIN and TAT from 2007 to 2009. PAY is not shown because it has no ceilometer or lidar. Low cloud accounts for more than half the cloud at both mid-latitude stations. At TAT, the percentage of low and middle cloud in CF_{Total} is almost constant at 60 to 70%. In contrast, the percentage

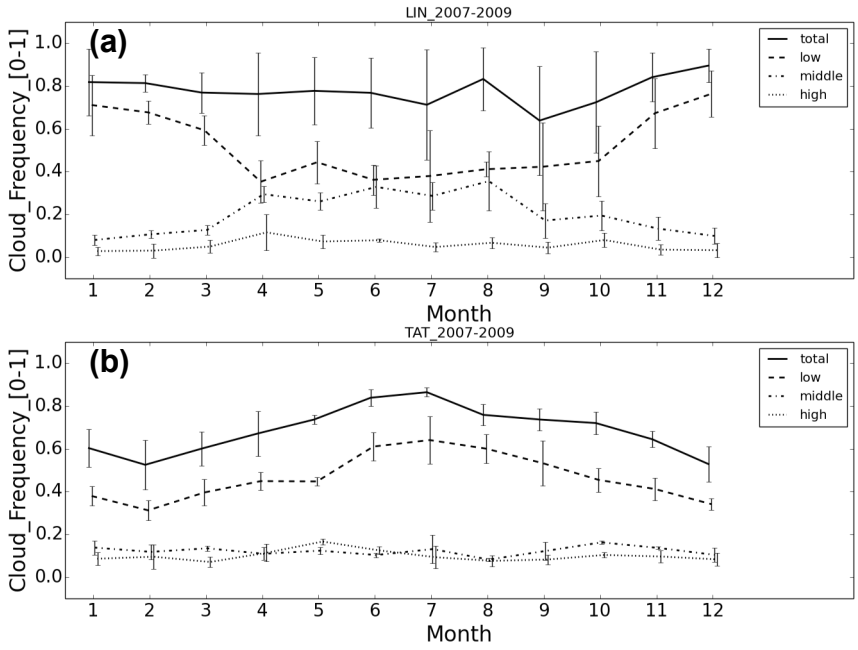

Figure 4.3. Comparison of cloud fraction by lidar/ceilometer at (a) LIN and (b) TAT for 2007 to 2009.

varies with the season at LIN; CF_{Total} in winter increases up to 80% and from spring to autumn falls below approximately 50%.

Low cloud accounts for a large percentage of total cloud and it is important for the surface radiation budget. Figure 4.4 compares the estimated low-middle cloud fraction ($CF_{Low\text{-}Middle}$) at LIN, PAY, and TAT obtained by lidar or ceilometer, visual observation, radiosonde estimation, and CloudSat-CALIPSO. The periods at PAY and TAT are from 2004 to 2006 and from 2007 to 2009, respectively, as in Figure 4.2. At LIN, $CF_{Low\text{-}Middle}$ observations end in March 2003, whereas the ceilometer observations are from June 2003. Therefore, $CF_{Low\text{-}Middle}$ values obtained by visual and ceilometer observations are not compared directly. Figure 4.4 compares visual and radiosonde observations of $CF_{Low\text{-}Middle}$ from 2000 to 2002, and ceilometer and radiosonde observations of $CF_{Low\text{-}Middle}$ from 2004 to 2006.

At LIN, the radiosonde estimations correspond to the ceilometer observations for low and middle cloud. The underestimation of $CF_{Low\text{-}Middle}$ by visual observations is larger than that of CF_{Total}, and thus it is caused by low

and middle cloud. Radiosonde and ceilometer estimations are the same overall, whereas $CF_{Low\text{-}Middle}$ is overestimated by radiosonde compared with the ceilometer estimates.

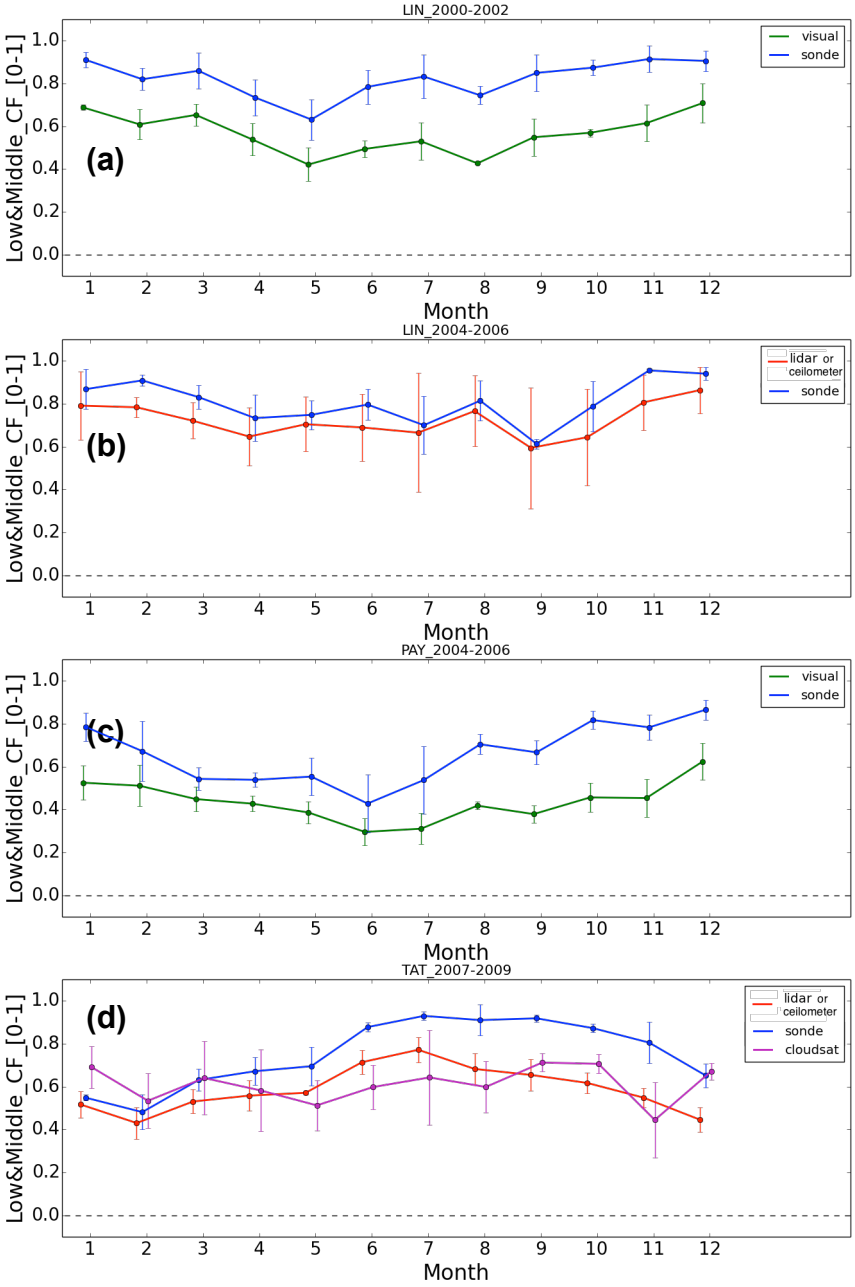

Figure 4.4. Comparison of $CF_{Low\text{-}Middle}$ for lidar/ceilometer, visual observation, radiosonde estimation, and CloudSat-CALIPSO at (a) LIN (2000–2002), (b) LIN (2004–2006), (c) PAY (2004–2006), and (d) TAT (2007–2009).

Figure 4.5 shows the seasonal cycles of CBH estimated by radiosonde, active sensors (LIN and TAT), and CloudSat-CALIPSO (TAT) in mid-latitude regions. At LIN, unlike the ceilometer estimates of CBH, the radiosonde estimates show no large changes and they are underestimated by 1 to 3 km.

For all cloud altitudes, PAY shows good agreement between the radiosonde and visually observed cloud fractions. However, $CF_{Low\text{-}Middle}$ estimated by radiosonde is smaller than that estimated by visual observation by 0.1 to 0.4. PAY has no active sensors and its observations

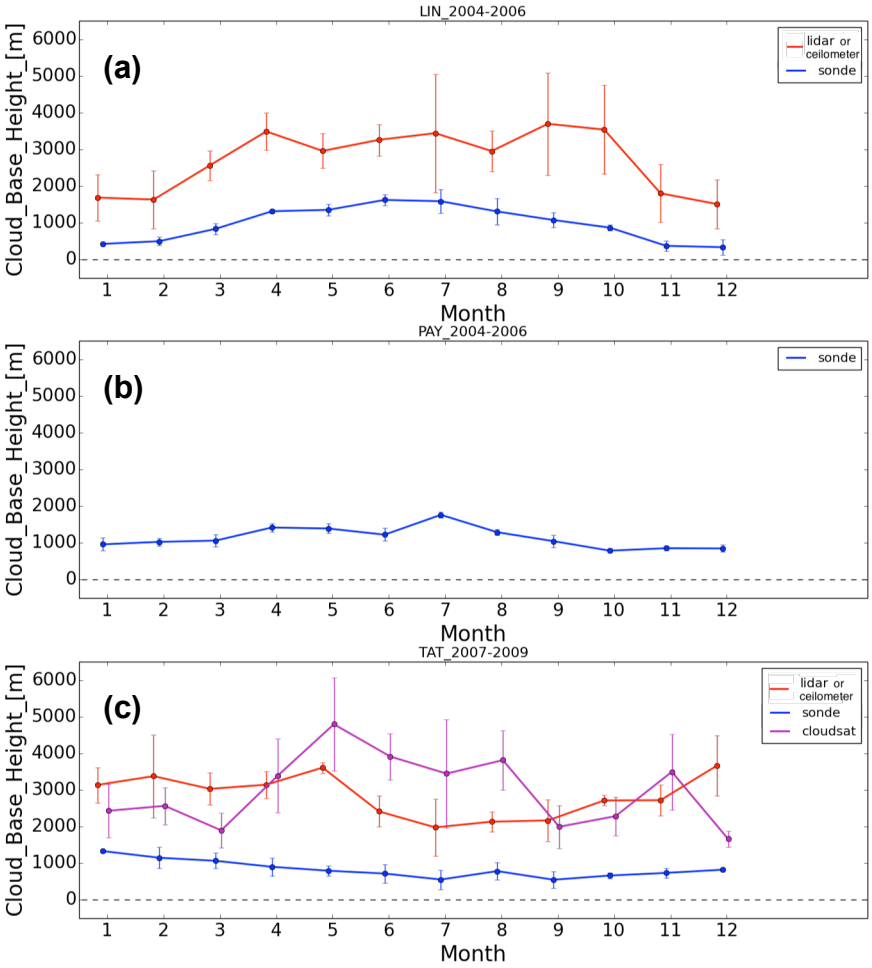

Figure 4.5. Comparison of cloud base height (CBH) between active sensor, radiosonde, and CloudSat-CALIPSO at (a) LIN (2000–002 and 2004–2006), (b) PAY (2004–2006), and (c) TAT (2007–2009).

cannot be compared with the CloudSat-CALIPSO product because of the observation period. The monthly averaged CBH estimated by radiosonde is around 1 km, which may be low because it is underestimated as it is at LIN. CBH is high for spring to summer and low from autumn to winter. $CF_{Low\text{-}Middle}$ was observed visually at TAT for a limited period and cannot be compared with the other estimated $CF_{Low\text{-}Middle}$ values. At TAT, radiosonde overestimates $CF_{Low\text{-}Middle}$ similar to the European continental region.

In general, the seasonal cycles of CF_{Total} estimated from visual and radiosonde observations correspond to lidar or ceilometer observations in the mid-latitude regions. However, visual observation tends to underestimate CF_{Total}, and radiosonde tends to overestimate CF_{Total}. The overestimation of cloud fraction by radiosonde is mainly caused by errors in measuring low or middle cloud.

Figure 4.6 shows the seasonal cycles of cloud radiative contribution (CRC) to L_D, S_D, and T_D in the mid-latitude region. At LIN, CRC to L_D ranges from 6 to 17%. The maximum and minimum are September and January, respectively. The seasonal cycle corresponds to seasonal cycles of T_S, PW, and CF_{Total}. The frequency of CF_{Total} was low from April to September. The cycle of CRC to S_D is slightly different from that of L_D; spring shows a small CRC of around 35%. Based on the ceilometer estimation, the frequency of low cloud decreases from April. The CRC to S_D varies more than the CRC to L_D. CRCs to L_D and S_D at PAY are similar to that at LIN. CF_{Total} reaches a minimum in June, during which the CRC to S_D also reaches minimum.

Compared with LIN and PAY, TAT shows different seasonal CRC cycles. CRC to L_D ranges from 5 to 11%. The minimum of CRC is in August, which corresponds to the largest amount of WV. However, the maximum CRC occurs in March and not in winter because both CF_{Total} and $CF_{Low\text{-}Middle}$ are small from December to February. The effect of cloud amount is more apparent in CRC to S_D; CRC is very small for winter at TAT.

For T_D, CRC is large in winter and small in summer. In the European continental regions, the negative maximum and minimum are found in December and in June, respectively, corresponding to SZA. At TAT, the minimum negative peak is in spring and the variation is weak.

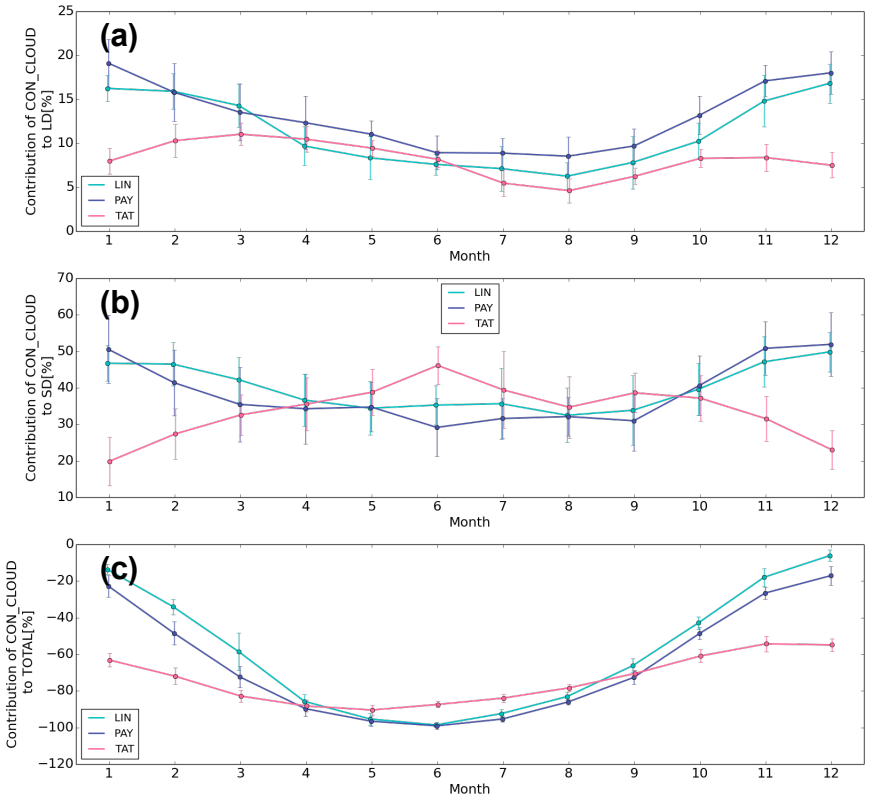

Figure 4.6. Seasonal cycles of CRCs to (a) L_D, (b) S_D, and (c) T_D at LIN, PAY, and TAT.

4.1.2 Inter-annual variations in mid-latitudes

Figure 4.7 shows the inter-annual trends of L_D, S_D, T_D, CRCs, CF_{Total}, $CF_{Low\text{-}Middle}$, T_S, PW, and diffuse and direct shortwave radiation at LIN from 1994 to 2007, PAY from 1996 to 2007, and TAT from 1997 to 2014. CF_{Total} and $CF_{Low\text{-}Middle}$ are estimated by visual observation. $CF_{Low\text{-}Middle}$ at TAT is not shown because of the short operating period. $CF_{Low\text{-}Middle}$ at LIN is only from 1996 to 2003.

4.1.2.1 LIN and PAY mid-latitude continental regions

Tables 4.1 and 4.2 contain the monthly mean trends of L_D, S_D, T_D, CRC, CF_{Total}, $CF_{Low\text{-}Middle}$, CBH, T_S, PW, and diffuse and direct shortwave radiation at LIN from 1994 to 2007 and PAY from 1996 to 2007, respectively. T_S and PW at LIN show an increasing trend of +1.20 K/decade and +0.37 mm/decade,

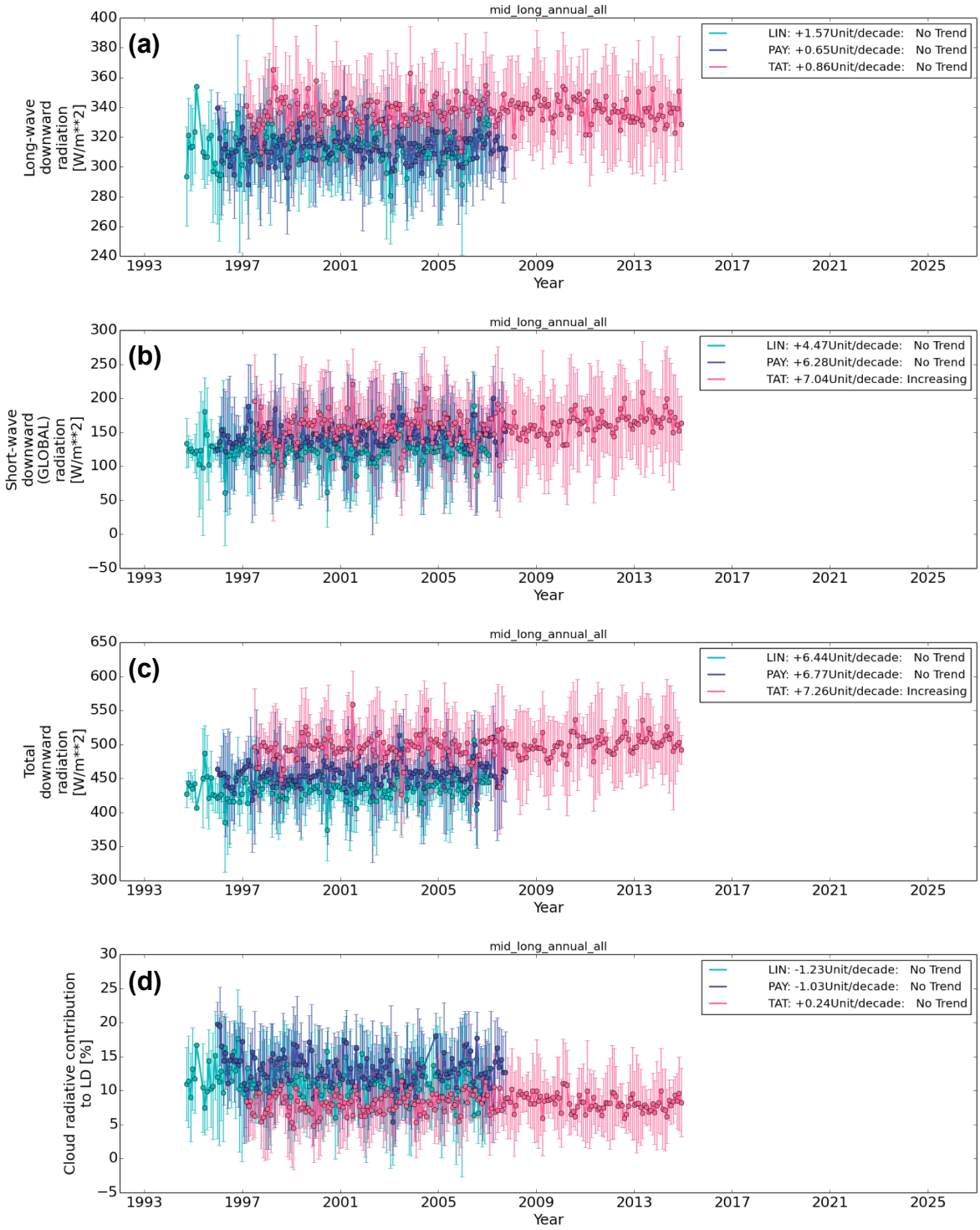

Figure 4.7. Inter-annual trends of (a) L_D, (b) S_D, (c) T_D, (d)–(f) CRCs, (g) CF_{Total}, (h) $CF_{Low-Middle}$, (i) shortwave diffuse, (j) direct, (k) T_S, and (l) PW at LIN, PAY, and TAT.

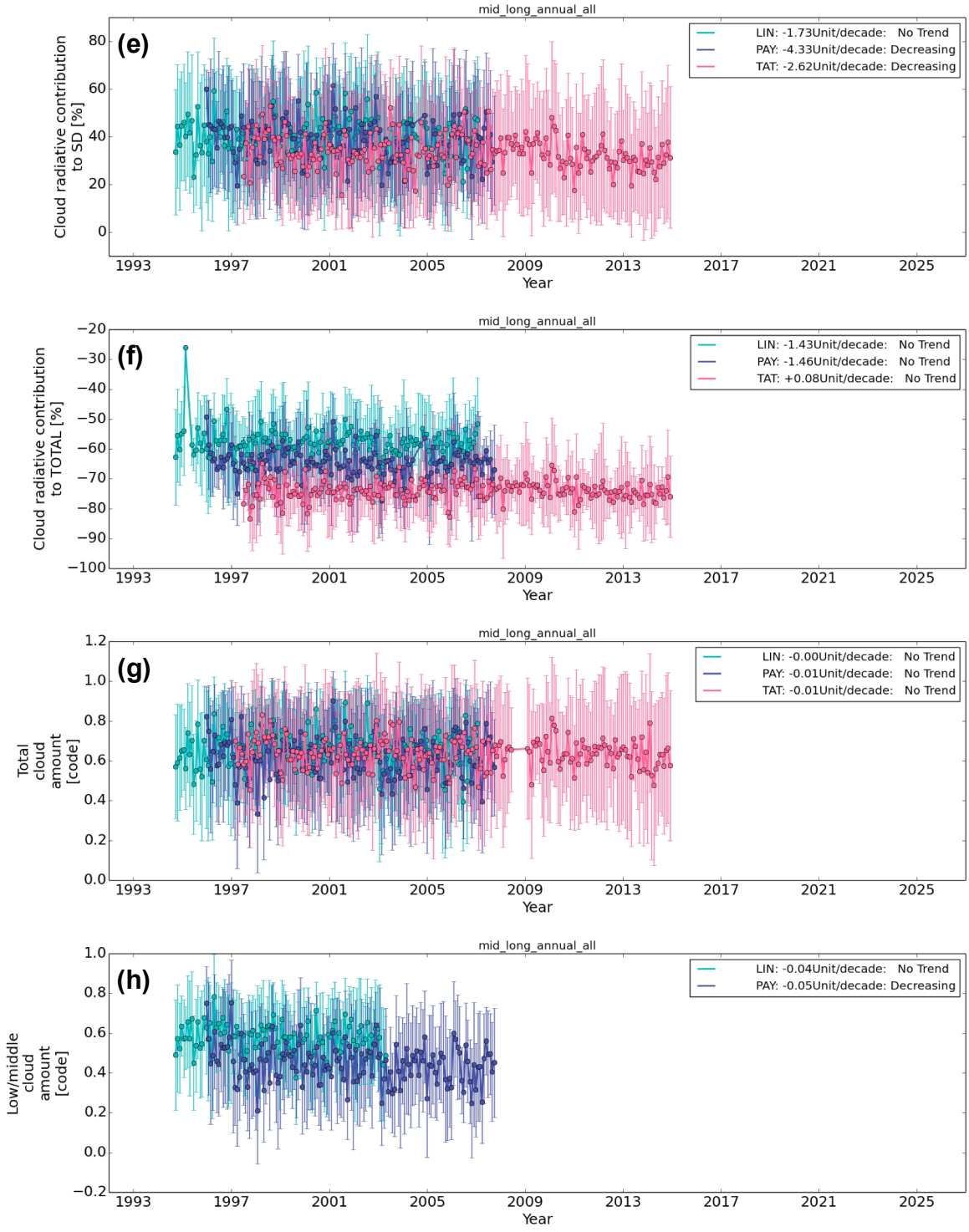

Figure 4.7. Continued.

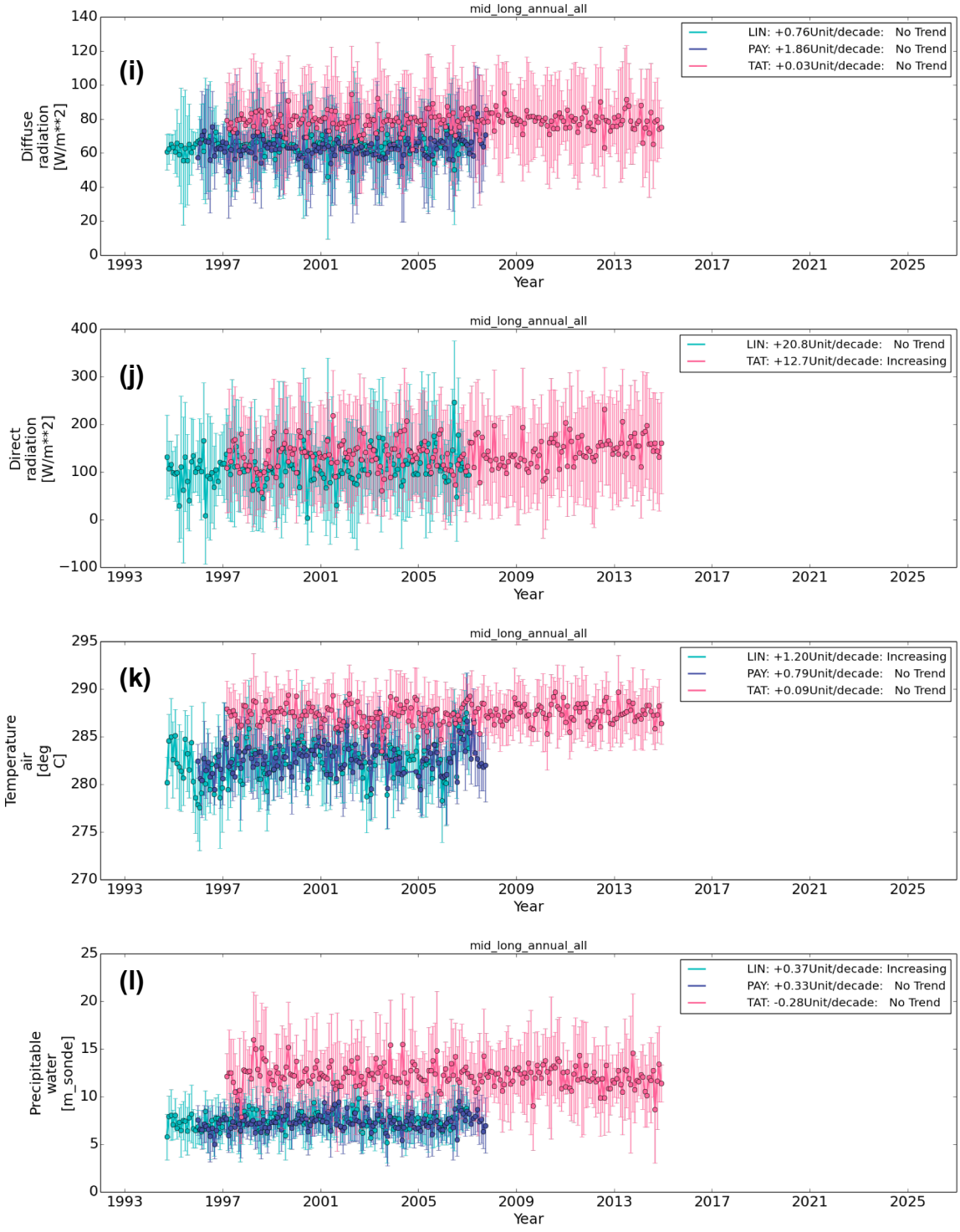

Figure 4.7. Continued.

respectively, for 14 years. These increasing trends satisfy the 95% confidence level. L_D does not show a reliable increasing trend. Because CRC decreases for L_D and S_D, no reliable trend in L_D is caused by decreasing cloud. CF_{Total} shows no significant trend, although the trend in $CF_{Low\text{-}Middle}$ is a small annual decrease, which may reduce L_D.

TTable 4.1. Monthly mean trends (revised seasonal) at LIN from 1994 to 2007 under all-sky conditions [/decade].

		Annual	Spring	Summer	Autumn	Winter
L_D	Flux [W m^{-2}]	+1.57	-1.56	**+6.72**	+1.02	+5.94
	CRC [%]	-1.23	-1.15	+0.30	-3.06	+0.13
S_D	Flux [W m^{-2}]	+4.47	+7.35	-0.29	+9.35	-1.44
	CRC [%]	-1.73	-3.13	+0.82	-5.79	+2.67
T_D	Flux [W m^{-2}]	+6.44	+5.70	-0.41	+10.3	+4.38
	CRC [%]	-1.43	-1.61	+1.68	-2.32	+0.80
CF_{Total} [0-1]	Visual	-0.00	-0.00	+0.01	-0.04	+0.03
	Sonde	+0.02	+0.03	+0.04	-0.01	+0.05
$CF_{Low\text{-}Middle}$ [0-1]	Visual(*1)	-0.04	**-0.16**	-0.00	-0.01	-0.01
	Sonde	+0.02	+0.03	+0.03	-0.01	+0.05
CBH [km]	Sonde	+0.04	+0.20	+0.14	+0.00	-0.07
Temperature [K]		**+1.20**	+0.47	+0.95	+1.91	+1.00
Precipitable Water [mm]		**+0.37**	-0.06	+0.59	+0.64	+0.12
Diffuse [W m^{-2}]		+0.76	+5.33	-0.70	-0.10	-0.00
Direct [W m^{-2}]		+20.8	+9.08	+34.2	+30.2	-1.56

(*1) Only for 1994 to 2003

The decreasing trend of $CF_{Low\text{-}Middle}$ at LIN is reliable, satisfying the 95% confidence level for spring. Spring shows a large decrease of $CF_{Low\text{-}Middle}$ of -0.16/decade. Changes in S_D of +7.35 W m^{-2}/decade and in CRC of -3.13%/decade in spring are significant. L_D for summer increases, satisfying the 95% confidence level. The significant trend in summer L_D is caused by small increases in T_S and PW. The increases in T_S and PW are not reliable trends, although CF_{Total} and $CF_{Low\text{-}Middle}$ show no apparent changes in

Table 4.2. Monthly mean trends (revised seasonal) at PAY from 1996 to 2007 under all-sky conditions [/decade].

		Annual	Spring	Summer	Autumn	Winter
L_D	Flux [W m^{-2}]	+0.65	+2.19	+3.84	+1.92	-3.92
	CRC [%]	-1.03	-0.27	-0.43	**-2.13**	+1.12
S_D	Flux [W m^{-2}]	+6.28	-2.53	+11.2	**+13.6**	+2.82
	CRC [%]	**-4.33**	+0.33	-3.46	**-10.6**	+2.91
T_D	Flux [W m^{-2}]	+6.77	+0.05	+14.5	**+15.6**	-0.99
	CRC [%]	-1.46	+0.24	-0.78	**-4.19**	+0.72
CF_{Total} [0-1]	Visual	-0.01	+0.02	+0.00	-0.06	-0.06
	Sonde	-0.04	-0.04	-0.00	-0.07	-0.04
$CF_{Low\text{-}Middle}$ [0-1]	Visual	**-0.05**	-0.01	-0.02	-0.09	-0.05
	Sonde	-0.04	-0.05	-0.00	-0.07	-0.04
CBH [km]	Sonde	+0.10	-0.02	+0.28	-0.00	+0.10
Temperature [K]		+0.79	+0.53	+0.95	+1.22	-0.58
Precipitable Water [mm]		+0.33	+0.25	+0.42	+0.69	-0.37
Diffuse [W m^{-2}]		+1.86	+0.52	-0.41	+4.66	+2.43
Direct [W m^{-2}]		NaN	NaN	NaN	NaN	NaN

summer, unlike other seasons. Therefore, L_D in summer shows a significant increase. For autumn and winter, there is no significant trend in the surface downward radiation and cloud fraction. Overall, T_D and CRC increase and decrease, respectively. However, the trends in T_D and the CRC do not satisfy the 95% confidence level.

T_S and PW at PAY increase annually, similar to LIN. The increasing trends of T_S and PW do not satisfy the 95% confidence level. A negligible increase in L_D and a decrease in the CRC are also observed at LIN. In contrast to LIN, the effect of changes in $CF_{Low\text{-}Middle}$ is clearer; $CF_{Low\text{-}Middle}$ and CRC to S_D decrease by -0.05/decade and -4.33%/decade, respectively, in the annual means. These trends satisfy the 95% confidence level. The trends are significant for autumn, during which the decrease in the CRC to L_D and S_D are reliable. Downward radiation and the CRC do not show a significant trend for the other seasons.

In summary, T_S and PW at both of the European continental stations show increasing trends. However, L_D does not show an increasing trend satisfying the 95% confidence level. The decrease in $CF_{Low\text{-}Middle}$ suppresses the increase in L_D, and there is also no significant trend in CF_{Total}. The inter-annual change in cloud cools the surface cool at PAY.

4.1.2.2 TAT in East Japan

4.1.2.2.1 Twenty-year trend for BSRN

Table 4.3 shows the monthly mean trends of L_D, S_D, T_D, CRC, CF_{Total}, $CF_{Low\text{-}Middle}$, CBH, T_S, PW, and diffuse and direct shortwave radiation at TAT from 1997 to 2014. L_D, T_S, and PW at TAT do not show strong annual trends. However, S_D increases and the CRC decreases, satisfying the 95% confidence level. The large changes in S_D and the CRC are +7.04 W m^{-2}/decade and -2.62%/decade, respectively. Because of the large change in CRC to S_D, the increase in S_D may be caused by decreasing cloud. However, CF_{Total} does not show a significant trend. $CF_{Low\text{-}Middle}$ was only observed for a limited period at TAT, which is not sufficient to evaluate trends. The direct observation increases satisfy the 95% confidence level, which indicates a decrease in the

cloud amount.

The decrease in S_D satisfies the 95% confidence level in autumn, but the rate of increase reaches a maximum in spring. Direct shortwave radiation increases strongly in spring by +21.4 W m^{-2}/decade. PW in spring decreases satisfying the 95% confidence level and T_S shows a slight decrease. Overall, the increase in T_D satisfies 95% confidence level with the annual average, but the CRC does not show a significant trend.

Table 4.3. Monthly mean trends (revised seasonal) at TAT from 1997 to 2014 under all-sky [/decade].

		Annual	Spring	Summer	Autumn	Winter
L_D	Flux [W m^{-2}]	+0.86	-2.66	+2.67	+3.63	-0.23
	CRC [%]	+0.24	+0.07	-0.42	+0.31	+0.95
S_D	Flux [W m^{-2}]	**+7.04**	+12.6	+6.93	**+5.74**	+2.11
	CRC [%]	**-2.62**	-3.46	-2.47	-2.52	-1.71
T_D	Flux [W m^{-2}]	**+7.26**	+6.94	+12.4	**+8.81**	+0.55
	CRC [%]	+0.08	-1.16	-0.20	+0.68	+0.39
CF_{Total} [0-1]	Visual	-0.01	-0.04	-0.00	-0.00	-0.00
	Sonde	-0.00	-0.03	+0.04	+0.01	-0.04
$CF_{Low-Middle}$ [0-1]	Visual	NaN	NaN	NaN	NaN	NaN
	Sonde	-0.00	-0.03	+0.04	+0.01	-0.04
CBH [km]	Sonde	+0.01	-0.04	+0.06	-0.07	+0.14
Temperature [K]		+0.09	-0.22	+0.46	+0.26	-0.22
Precipitable Water [mm]		-0.28	**-0.87**	+0.14	-0.13	-0.34
Diffuse [W m^{-2}]		+0.03	-2.09	+2.07	-0.25	-0.35
Direct [W m^{-2}]		**+12.7**	**+21.2**	+11.2	+12.6	+7.30

4.1.2.2.2 Fifty-five year trend for L_D from Aerological Data of Japan

The radiative transfer calculation of L_D by mstrnX and radiosonde estimations of the vertical distributions of air temperature and humidity show good agreement with observations under clear-sky and overcast conditions. In this section, we analyze calculated L_D and its contributions over 55 years from 1957 to 2011 at TAT under clear-sky and overcast conditions. Radiosonde data is obtained from the Aerological Data of Japan from 1957 to 1996 and BSRN from 1997 to 2011. The data time is 00UTC (local time 9 AM). For the 55-year analysis, we use only data in January, April, July, and October as typical values for winter, spring, summer, and autumn, respectively. January 1957 and October 1965 are missing. To consider the effect of the upper atmospheric temperature, we use the

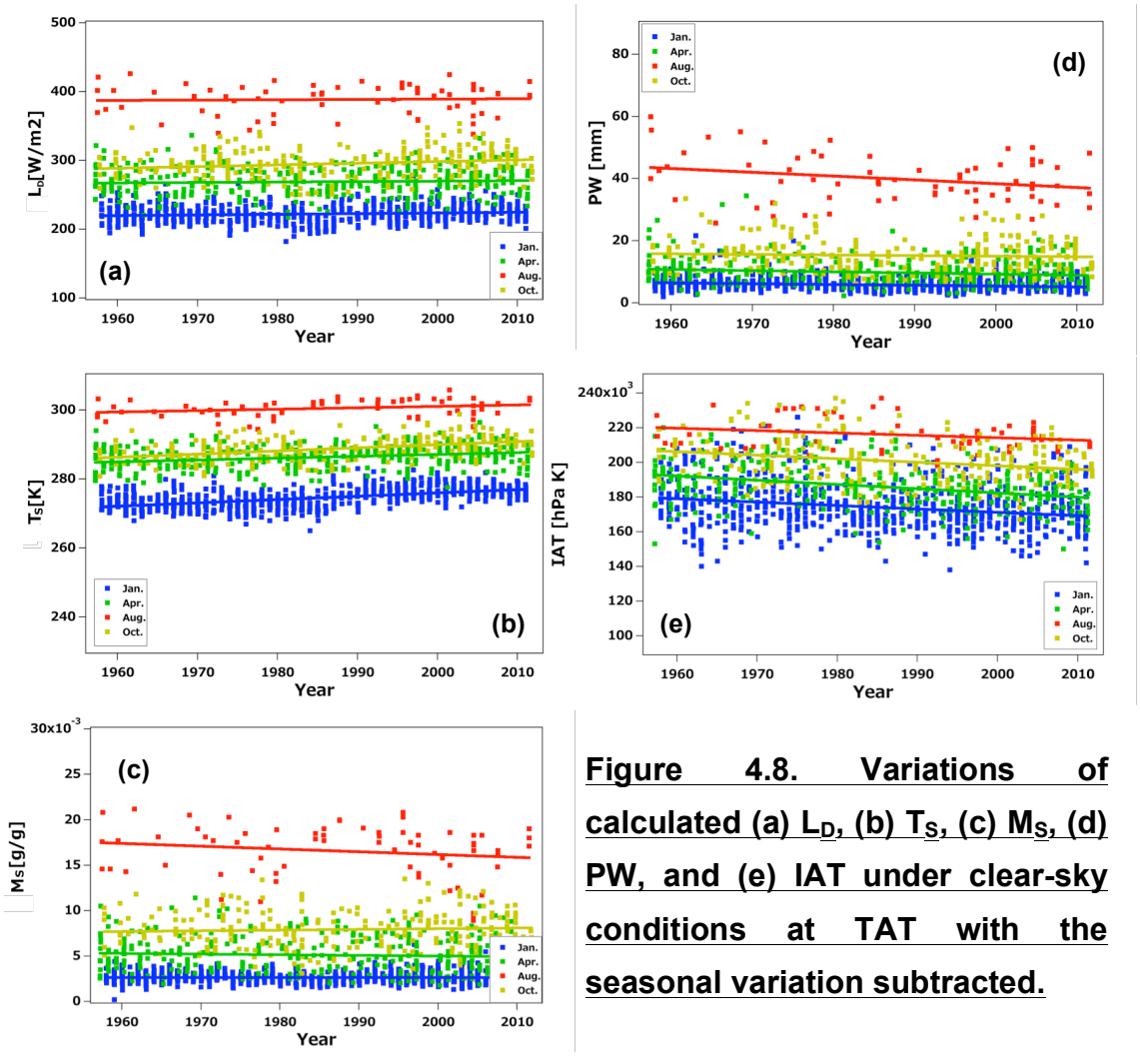

Figure 4.8. Variations of calculated (a) L_D, (b) T_S, (c) M_S, (d) PW, and (e) IAT under clear-sky conditions at TAT with the seasonal variation subtracted.

integrated air temperature (IAT), defined in Eq. (2.1).

Figure 4.8 shows the variations and averages of L_D, T_S, M_S, PW, and IAT (Tables 4.4 and 4.5). The average values in the tables are the mean values from the four months (four seasons). L_D increases in all seasons, and the increase in the four seasons average is approximately 1.1 W m^{-2}/decade. The months with the first and second largest increases are October and January, respectively, and only these months satisfy the 95% confidence level. April and July show large variability. T_S also increases for all seasons, and the increases satisfy the 95% confidence level. October and January show large increases of approximately 0.9 K/decade, similar to L_D. PW shows a decreasing trend for all seasons, and the trends in January and October satisfy the 95% confidence level. The mean average of the variation is -0.5 mm/decade. M_S does not show a significant trend. The largest decrease is -3.0 g/g/decade in July, when the decrease in PW is significant. In October, when the variability of PW is smallest, M_S shows a weak increase, unlike other seasons. Based on the results, the inter-annual change of M_S generally corresponds to PW. M_S sometimes increases because it is affected by an increase in T_S at the surface, and L_D increases significantly. T_S increases, although IAT decreases in all seasons and satisfies the 95% confidence level,

Table 4.4. Fifty-five year averages of L_D, T_S, M_S, PW, and IAT under clear-sky conditions at TAT.

Month	L_D	T_S	M_S	PW	IAT	Number of data
January	222.1 ±12.2	274.5 ±2.9	2.6 ±0.6	5.7 ±2.0	1.74 ±0.14	773
April	268.7 ±20.5	286.3 ±3.3	5.1 ±2.0	9.8 ±4.3	1.86 ±0.13	333
July	388.3 ±21.9	300.5 ±2.6	16.6 ±2.9	39.8 ±7.6	2.16 ±0.09	68
October	295.3 ±20.3	288.8 ±3.3	7.9 ±2.0	15.2 ±5.1	2.01 ±0.13	262
Average	293.7	287.5	8.0	17.6	1.90	
	[W m^{-2}]	[K]	[mm]	[10^{-3} g/g]	[10^5hPaK]	

Table 4.5. Fifty-five-year variations of L_D, T_S, M_S, PW, and IAT under clear-sky conditions. Orange and teal indicate reliability at the 95% confidence level for positive and negative trends, respectively.

Month	L_D	T_S	M_S	PW	IAT	Number of data
January	+0.95	+0.95	-0.00	-0.25	-0.02	773
April	+0.65	+0.52	-0.07	-0.37	-0.02	333
July	+0.47	+0.41	-0.30	-1.21	-0.02	68
October	+2.37	+0.90	+0.08	-0.19	-0.01	262
Average	+1.11	+0.69	-0.07	-0.50	-0.02	
	[W m^{-2}/decade]	[K/decade]	[10^{-3} g/g /decade]	[mm/decade]	[10^5hPaK /decade]	

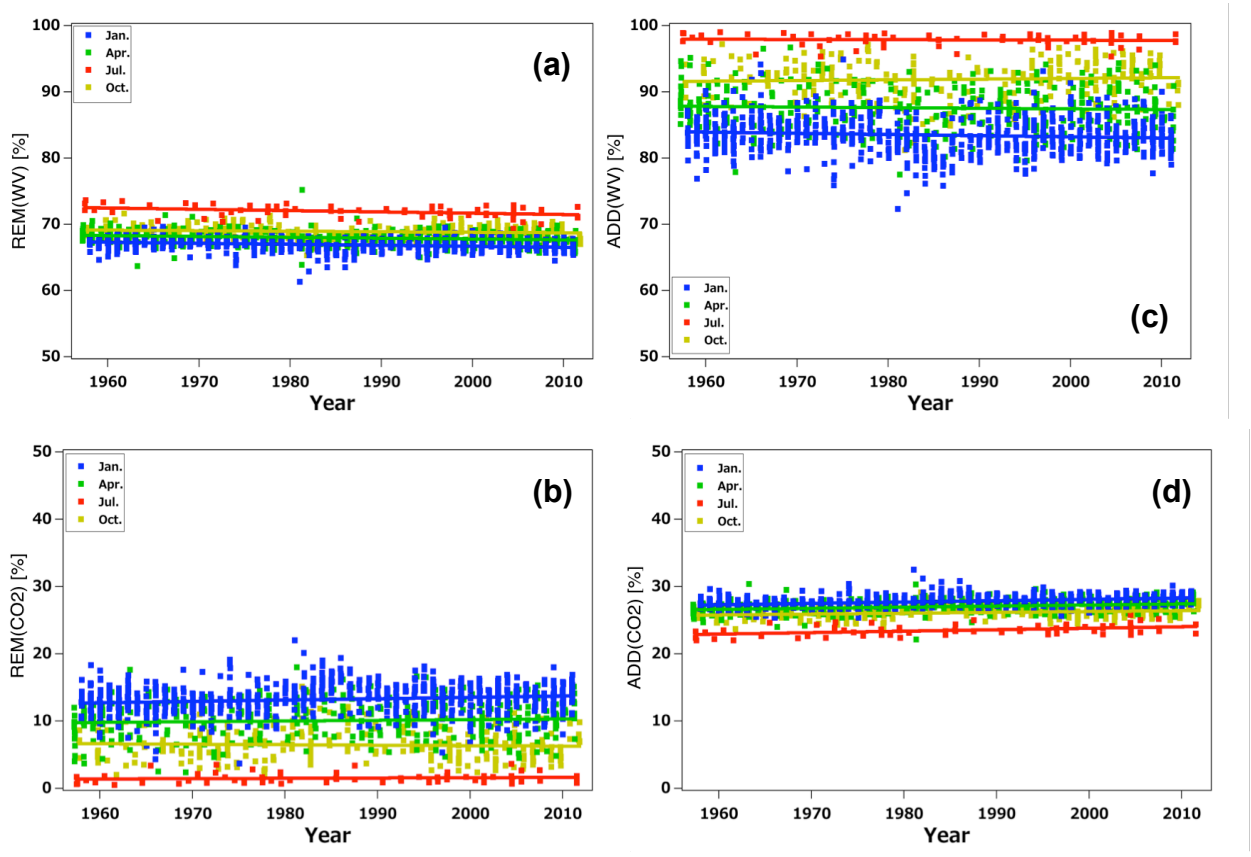

Figure 4.9. Contributions calculated by the (a), (b) removal and (c), (d) addition methods for (a), (c) WV and (b), (d) CO_2 under clear-sky conditions at TAT with the seasonal variation subtracted.

Table 4.6. Fifty-five-year variations of the contributions of WV and CO_2 under clear-sky condition. Orange and teal indicate reliability at the 95% confidence level for positive and negative trends.

Month	REM_{WV}	ADD_{WV}	REM_{CO2}	ADD_{CO2}	Number of data
January	**-0.14**	**-0.18**	**+0.20**	**+0.20**	773
April	**-0.12**	-0.09	+0.10	**+0.16**	333
July	**-0.20**	-0.04	+0.04	**+0.22**	68
October	-0.08	+0.11	-0.06	**+0.13**	262
Average	-0.13	-0.05	+0.07	+0.18	
	[%/decade]	[%/decade]	[%/decade]	[%/decade]	

except for July, when clear-sky conditions are infrequent. The results indicate surface warming and cooling in the upper atmosphere.

Figure 4.9 shows the inter-annual variations of the radiative contributions of WV and CO_2 under clear-sky conditions. Table 4.6 shows the increasing percentage of the contributions and the reliability. The CO_2 contribution increases, and the WV contribution decreases. The average of the change in the percentage contribtion of REM_{WV} is -0.13%/decade. The decreasing trends satisfy the 95% confidence level, except in October, where PW shows a smaller decrease. The increase in the percentage contribution of L_D in October is larger than other months. The decrease in the percentage contribution of REM_{WV} reaches a maximum in July of -0.2%/decade. The contribution of WV estimated by the addition method (ADD_{WV}) does not show a significant trend, except for in January.

REM_{CO2} also shows no significant trend, except for in January. The increases in ADD_{CO2} satisfy the 95% confidence level for all seasons, and the mean percentage increase is +0.18%/decade. The significant trends in the radiative contributions of WV and CO_2 in January may be caused the large amount of clear-sky data and the small amount of WV magnifying the increase in CO_2.

Figure 4.10 shows the inter-annual variations of L_D, T_S, M_S, PW, IAT, and CBH under overcast conditions. CBH is estimated by radiosonde.

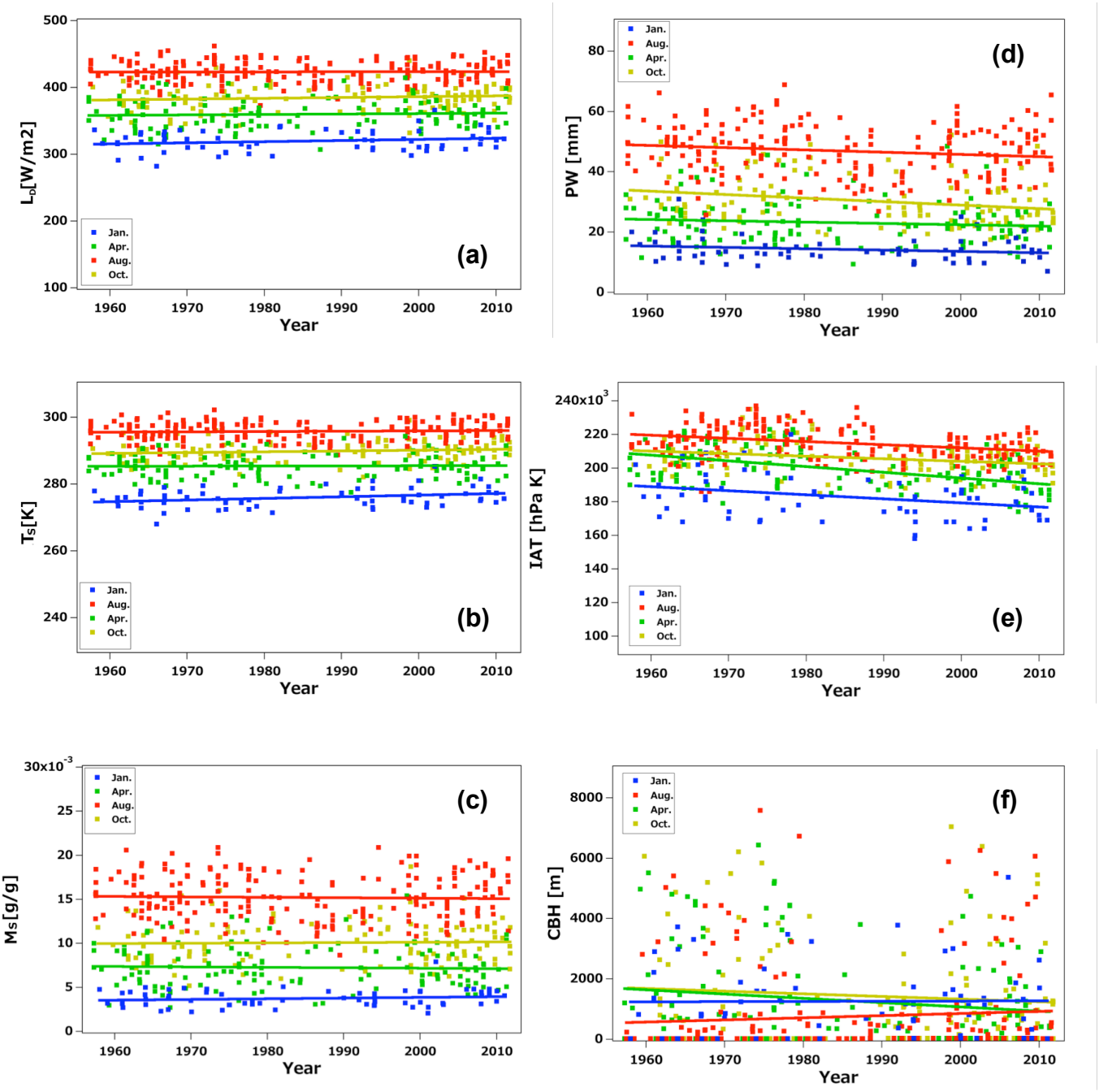

Figure 4.10. Variations of (a) L_D, (b) T_S, (c) M_S, (d) PW, (e) IAT, and (f) CBH under overcast conditions at TAT with seasonal changes subtracted.

Fifty-five-year averages of L_D, T_S, M_S, PW, IAT, and CBH are presented in Table 4.7, and their variability and credibility are shown in Table 4.8. Because the number of overcast days is small and cloud is variable, there are fewer reliable trends than under clear-sky conditions. L_D and T_S show

increasing trends, and PW shows a decreasing trend. Similar to clear-sky conditions, the increase in the contribution of L_D is significant in January and October. The average over four seasons of the increase in the L_D contribution is +0.9 W m^{-2}/decade. PW shows a reliable decreasing trend satisfying the 95% confidence level in October. The average over four seasons of the change in PW is -0.4 mm/decade, and the average over four seasons of the increase in T_S is +0.22 K/decade and is smaller than under clear-sky

Table 4.7. Fifty-five year averages of L_D, T_S, M_S, PW, IAT, and CBH under overcast conditions.

Month	L_D	T_S	M_S	PW	IAT	CBH	Number of data
January	319.6 ±15.4	275.9 ±2.9	3.7 ±9.6	14.9 ±4.3	2.06 ±0.09	1256 ±1190	64
April	359.7 ±21.6	288.3 ±3.4	7.3 ±2.3	23.3 ±7.1	2.00 ±0.12	1307 ±1604	131
July	423.0 ±15.4	295.8 ±2.8	15.2 ±2.6	47.6 ±9.7	2.15 ±0.09	739 ±1494	217
October	384.6 ±19.2	289.8 ±2.9	10.1 ±2.3	30.5 ±8.0	1.83 ±0.13	1432 ±1739	121
Average	371.7	287.5	9.0	28.9	2.00	1180	
	[W m^{-2}]	[K]	[10^{-3} g/g]	[mm]	[10^5hPaK]	[m]	

Table 4.8. Fifty-five-year variations of L_D, T_S, M_S, PW, IAT, and CBH under overcast conditions. Orange and teal indicate reliability at the 95% confidence level.

Month	L_D	T_S	M_S	PW	IAT	CBH	Number of data
January	+1.66	+0.04	+0.07	-0.32	-0.02	+7	64
April	+0.68	+0.10	-0.05	-0.36	-0.03	140	131
July	+0.09	+0.48	-0.05	-0.87	-0.02	+68	217
October	+1.21	+0.24	+0.04	-0.11	-0.02	-86	121
Average	+0.911	+0.22	+0.02	-0.41	-0.02	-151	
	[W mW m^{-2} /decade]	[K /decade]	[10^{-3} g/g /decade]	[mm /decade]	[10^5hPa /decade]	[m /decade]	

conditions. M_S shows large variability and no significant trend. Unlike temperature and humidity, IAT shows a decreasing trend satisfying the 95% confidence level for all seasons, the same as under clear-sky conditions. The average over four seasons of the change in IAT is -0.023×10^5 hPa K/decade, which is a stronger trend than under clear-sky conditions. CBH shows large variability. CBH shows decreasing trends in April and October, whereas that in July shows an increasing trend satisfying the 95% confidence level.

Figure 4.11 shows the inter-annual variations in the contributions to L_D of WV, CO_2, and cloud under overcast conditions. The trends are shown in Table 4.9. The cloud contributions of REM_{Cloud} and ADD_{Cloud} increase, except for in July. The variability is large and does not satisfy the 95% confidence level. These results show that it is difficult to estimate the change in cloud over 55 years.

Because of the large contribution of cloud, the contribution of WV shows a decreasing trend with large variation. However, some months show an increasing trend. The CO_2 contribution shows an increasing trend for all months calculated by the addition method.

Under overcast conditions, CBH shows large variability. In July, CBH increases by approximately +70 m/decade, and the trend is reliable, satisfying the 95% confidence level. Because of the effect of CBH, the cloud contribution in July decreases, although the other months show increasing trend in cloud contribution.

The four seasonal mean variations of L_D, T_S, and PW under clear-sky conditions are +1.1 W m^{-2}/decade, +0.7 K/decade, and -0.5 mm/decade, respectively. Under overcast conditions, the mean variations of L_D, T_S, and PW are +0.9 W m^{-2}/decade, +0.2 K/decade, and -0.4 mm/decade, respectively. Because radiative transfer calculated by mstrnX corresponds to the observed values under clear-sky and overcast conditions, we evaluate the 55-year variations of L_D. The calculated and observed L_D values are different because of observation errors and insufficient parameters in the model. The differences between the calculated and observed L_D values at TAT are -5.38 ± 3.90 W m^{-2} under clear-sky conditions and $+4.12 \pm 10.68$ W m^{-2} under overcast conditions.

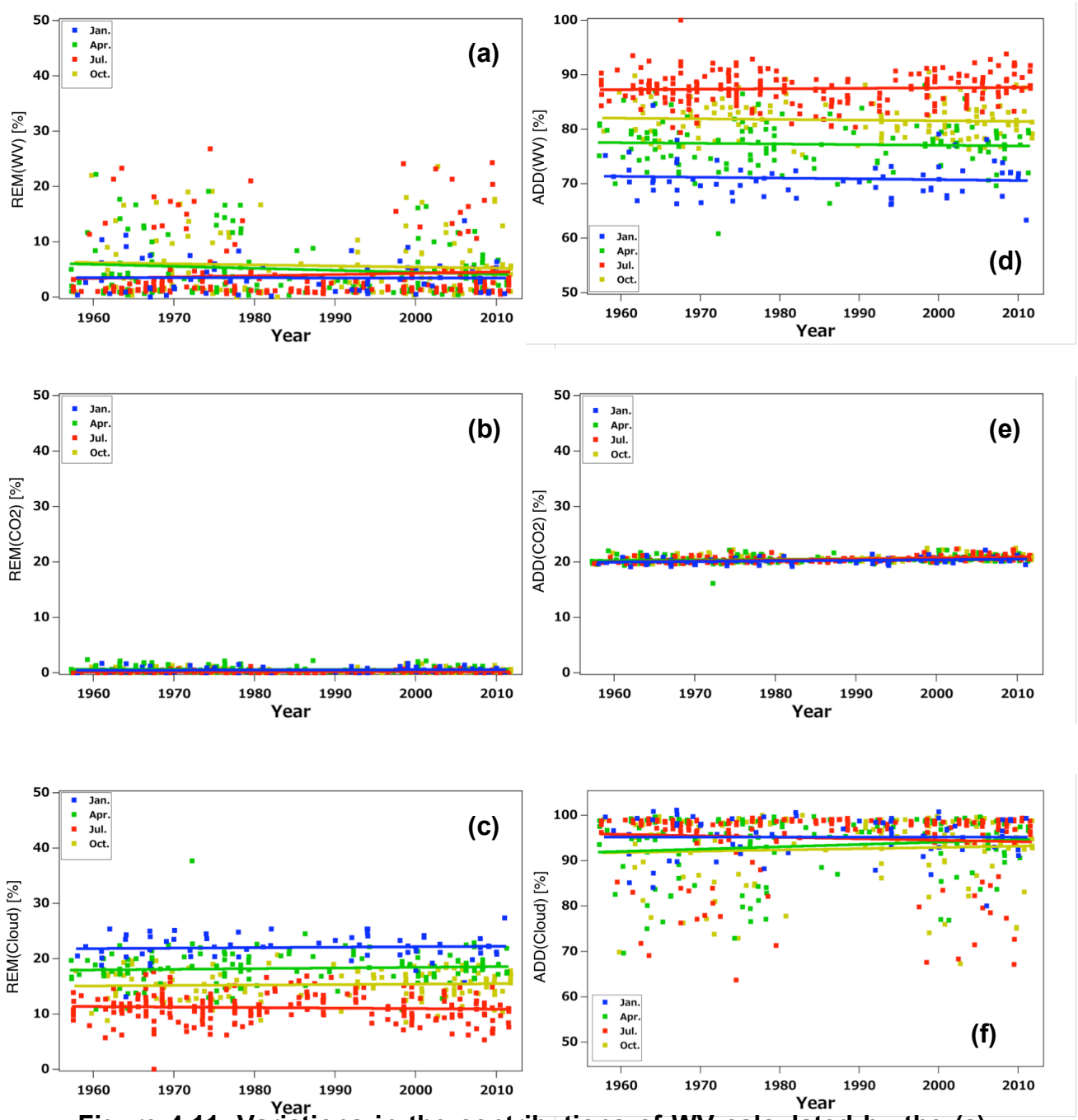

Figure 4.11. Variations in the contributions of WV calculated by the (a) removal and (d) addition methods, CO_2 calculated by the (b) removal and (e) addition methods, and cloud calculated by the (c) removal and (f) addition methods under overcast conditions at TAT with the seasonal changes subtracted.

Table 4.9. Fifty-five year variations of contributions of WV, CO_2, and cloud under overcast conditions. Orange and teal indicate reliability at the 95% confidence level

Month	REM_{WV}	ADD_{WV}	REM_{CO2}	ADD_{CO2}	REM_{Cloud}	ADD_{Cloud}	Number of data
January	-0.19	+0.03	+0.18	**+0.10**	+0.08	+0.06	64
April	-0.35	-0.03	-0.11	**+0.08**	+0.11	+0.51	131
July	+0.23	+0.01	+0.08	**+0.17**	-0.09	-0.31	217
October	-0.19	+0.01	-0.12	**+0.13**	+0.08	+0.27	121
Average	-0.13	+0.01	+0.10	+0.12	+0.05	+0.13	
	[%/decade]	[%/decade]	[%/decade]	[%/decade]	[%/decade]	[%/decade]	

In this study, the increase in L_D (ΔL_D), is defined as the slope of the linear approximation. If it is assumed that the slope is equal to the yearly variations, ΔL_D is expressed by Eq. (4.1) as

$$\begin{aligned} \Delta L_D &\approx \overline{\Delta L_{D,i}} \\ &= \frac{\sum_{i=1}^{n} \Delta L_{D,i}}{n}, \end{aligned} \tag{4.1}$$

where $\Delta L_{D,i}$ is the increase over a year and is the difference in L_D between the current year and the previous year. $\Delta L_{D,i}$ can be written as Eq. (4.2).

$$\Delta L_{D,i} = L_{D,i} - L_{D,(i-1)}. \tag{4.2}$$

If the errors and standard deviations of $L_{D,i}$ are separate and random, the differences in $\Delta L_{D,i}$ are calculated by the sum of squares. Thus, the error of ΔL_D ($\delta\Delta L_D$) is expressed by Eq. (4.3).

$$
\begin{aligned}
\delta\Delta L_D &\approx \frac{\sum_{i=1}^{n} \delta\Delta L_{D,i}}{n} \\
&= \frac{1}{n} * n * \delta\Delta L_{D,i} \\
&= \delta\Delta L_{D,i} \\
&= \sqrt{\left(\delta L_{D,i}\right)^2 + \left(\delta L_{D,(i-1)}\right)^2} \\
&= \sqrt{2}\delta L_{D,i}.
\end{aligned}
\tag{4.3}
$$

From Eq. (4.3), the error of the whole trend is equal to the √2 times the error (standard deviation). Because the increase of +6.1 W m^{-2} over 55 years under clear-sky conditions is larger than √2 times the error of L_D of 5.5 W m^{-2} at TAT, the increase is reliable. However, the increase under overcast conditions is not reliable because the increase of +5 W/m^2 is smaller than √2 times the L_D error of 15.1 W m^{-2} at TAT.

The all-sky values are calculated based on the weighted average. The all-sky variations of L_D, T_S, and PW are +1.05 W m^{-2}/decade +0.56 K/decade, and -0.58 mm/decade, respectively. The increase in L_D by 1.05 W m^{-2} is reported as approximately half the global mean value of +2.2. W m^{-2}/decade by Wang and Liang (2009) under all-sky conditions. The increase of +1.05 W/m^2/decade is also smaller than that reported by Prata (2008), who evaluated the global mean increase of L_D as +1.67 W m^{-2}/decade ignoring the effects of cloud.

In general, an increase in air temperature causes an increase in PW. The global mean T_S and PW evaluated by Prata (2008) show increasing trends. In contrast, the present study shows a decreasing trend in PW. The PW trend is reliable satisfying the 95% confidence level in January and April under clear-sky conditions and in October under overcast conditions. Therefore, the difference in ΔL_D between the present and previous studies is caused by the difference in PW trends. To evaluate the effect of air temperature and humidity, effective emissivity (EE) is defined by Eq. (4.4).

$$EE = {L_D}/{\sigma * {T_S}^4}. \quad (4.4)$$

Figure 4.12 shows the variation of EE under clear-sky and overcast conditions. Tables 4.10 and 11 show the averages and variations for each season. In Table 4.11, orange and teal indicate trends with reliability at the 95% confidence level. The variation of EE under clear-sky and overcast conditions is approximately -0.004/decade for the average over four seasons. The variation is not reliable under overcast conditions, whereas clear-sky conditions satisfy the 95% confidence level except for October. Because PW does not satisfy the 95% confidence level variation only in October, the low reliability of the decrease in EE in October is caused by the decrease in PW and emissivity.

From the definition

$$L_D = \sigma EE {T_S}^4, \quad (4.5)$$

L_D is $L_D(EE, T_S)$, and the increases in T_S (ΔT_S) and EE (ΔEE) when L_D increases by ΔL_D are expressed by Eqs. (4.6) and (4.7).

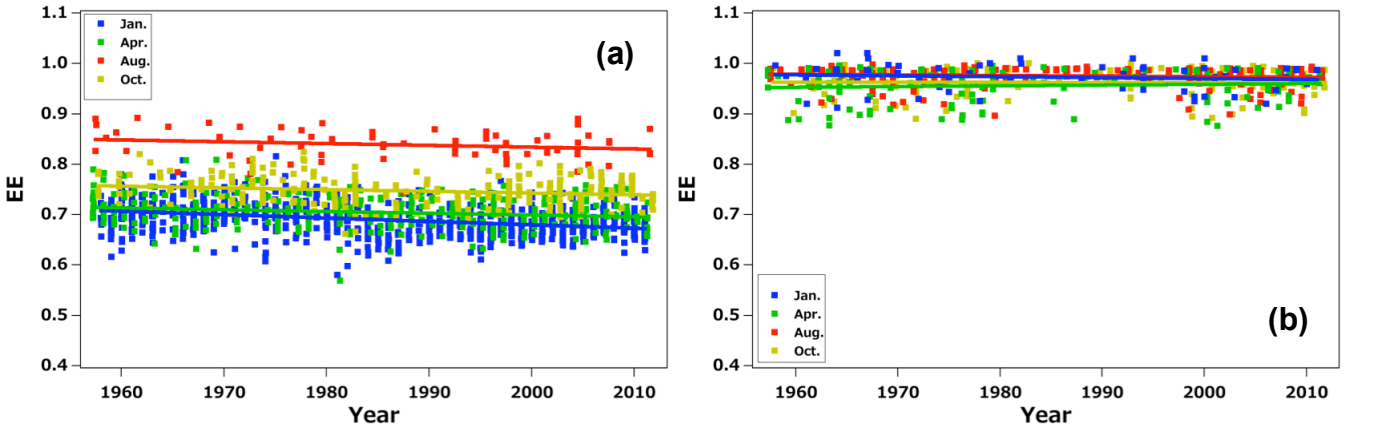

Figure 4.12. Inter-annual variations of EE under (a) clear-sky and (b) overcast conditions.

Table 4.10. Fifty-five-year mean EE at TAT under clear-sky and overcast conditions.

Month	Clear-sky	Number of data	Overcast	Number of data
Jan.	0.69±0.04	773	0.97 ±0.03	64
Apr.	0.71±0.04	333	0.96 ±0.03	131
Jul.	0.87±0.12	68	0.98 ±0.02	217
Oct.	0.74±0.04	262	0.96 ±0.03	121
Average	0.753		0.968	

Table 4.11. Fifty-five-year variations of EE at TAT under clear-sky and overcast conditions. Orange and teal indicate reliability at the 95% confidence level.

Month	Clear-sky	Number of data	Overcast	Number of data
Jan.	**-6.64**	789	01.76	94
Apr.	**-3.43**	358	+1.37	197
Jul.	**-3.50**	66	-1.05	297
Oct.	-3.33	258	-0.08	213
Average	-4.23	1471	+0.38	801
	[10^{-3}/decade]		[10^{-3}/decade]	

$$
\begin{aligned}
L_D + \Delta L_D &= \sigma(EE + \Delta EE)(T_S + \Delta T_S)^4 \\
&= \sigma(EE + \Delta EE){T_S}^4 \left(1 + \frac{\Delta T_S}{T_S}\right)^4 \\
&\approx \sigma(EE + \Delta EE){T_S}^4 \left(1 + 4\frac{\Delta T_S}{T_S}\right) \\
&= \sigma EE{T_S}^4 + \sigma{T_S}^3(4EE\Delta T_S + T_S\Delta EE),
\end{aligned} \tag{4.6}
$$

$$
\Delta L_D = \sigma{T_S}^3(4EE\Delta T_S + \Delta T_S\Delta EE). \tag{4.7}
$$

The weighted average T_S and EE under all-sky conditions are 287.5 K and 0.81, respectively. For ΔT_S = 0.56 K/decade and ΔEE = -0.00319 /decade, the annual average of ΔL_D of +1.05 W m^{-2}/decade and $\delta T_S(4EE\Delta T_S + T_S\Delta EE)$ of 1.24 W m^{-2}/decade are similar. Therefore, the increase T_S outweighs the decrease of PW and increases L_D. To increase L_D, the ratio of the contributions of the absolute values of T_S and EE is 2:1. The effect of T_S variation is twice that of the emissivity caused by variations in WV and CO_2.

Therefore, the 55-year variation of L_D of 1.05 W m^{-2}/decade at TAT in the present study is much smaller than global mean values of the previous studies, because the difference is caused by the decrease of PW, which increases compared with the global average. The A1B scenario of the Special Report on Emission Scenarios, the Intergovernmental Panel on Climate Change (IPCC) 4th Assessment predicted that the amount of precipitation in summer for 2090 to 2099 will increase by 5 to 20% compared with 1980 to 1990 (IPCC, 2007). Iwashima and Yamamoto (1993) compared the amounts of precipitation at 55 Japan Meteorological Agency stations in Japan over 100 years from the 1890s. They reported an increase in the number of high rainfall days. However, the amount of rainfall does not show a monotonic increase. A simulation of East Asian atmospheric circulation in the Model for Interdisciplinary Research On Climate version 3.2 (K-1 Model Developer, 2004) by Kimoto (2005) showed a decrease in the difference in the temperature between sea and land for winter for 2071 to 2100 compared with 1971 to 2000. However, the difference in the temperature for summer increases. The differences in temperature between land and ocean weakened the winter monsoon and precipitation. For summer, the monsoon and precipitation were increased. Kimoto et al. (2005) predicted an increase in the frequencies of strong precipitation (≧30 mm/day) and no precipitation days (<1 mm/day), and a decrease in low precipitation days (1 to 20 mm/day) by using the same model as Kimoto (2005).

Similar to previous studies, precipitation increased in summer and decreaed in winter, although the initial precipitation amounts were small. Because we examined only clear-sky and overcast conditions without rainy days in this section, the results are not affected by the rainfall and they show

a decrease in PW for all seasons. In summer, monsoons affect the precipitation and the decreasing trend is weak.

4.2 Polar regions

4.2.1 Seasonal cycles in polar regions

Figure 4.13 shows the seasonal cycles of L_D, S_D, T_D, T_S, PW, and CF_{Total} in NYA, SYO, and GVN. Because SYO (69.005°S, 39.589°E) and GVN (70.65°S, 8.25°W) are close, the seasonal cycles of S_D and PW are similar. L_D at SYO is large from March to July (autumn to winter) and small from November to January (late spring to early summer), which is mainly caused by the variations in T_S and CF_{Total}. CF_{Total} at SYO from March to July is much larger than at GVN and cloud increases L_D. However, CF_{Total} at GVN from November to January is larger than at SYO. In the months with a small difference in CF_{Total}, larger T_S contributes to increasing L_D at SYO. Summer S_D is slightly larger than at GVN. The larger S_D is caused by the small amount of cloud. Overall, downward radiation is similar, although it is larger at SYO from autumn to winter.

At NYA in the Arctic coastal region, T_S and PW are larger, resulting in a much larger L_D than in the Antarctic region that reaches more than 300 W m^{-2} in July at mid-summer. Although shortwave radiation should be mainly controlled by the solar zenith angle (SZA), S_D in June shows very small difference from May. Although NYA is at a higher latitude (78.925°N, 11.93°E), S_D for summer at NYA is smaller than at GVN and SYO. The small S_D at NYA is caused by the melting snow and decreasing albedo in summer. Snow melting at NYA starts in June and the size of the albedo decreases by 0.2 from May with the monthly mean averages (Figure 4.14). On the snow surface, the shortwave upward radiation makes a large contribution to S_D from the multiple scattering between the snow surface and the cloud or atmosphere. Surface albedo contributes to S_D by about 10% in polar regions with a large surface albedo (Section 3.2). Summer with low SZA at NYA shows a small albedo because of melting snow reducing upward shortwave

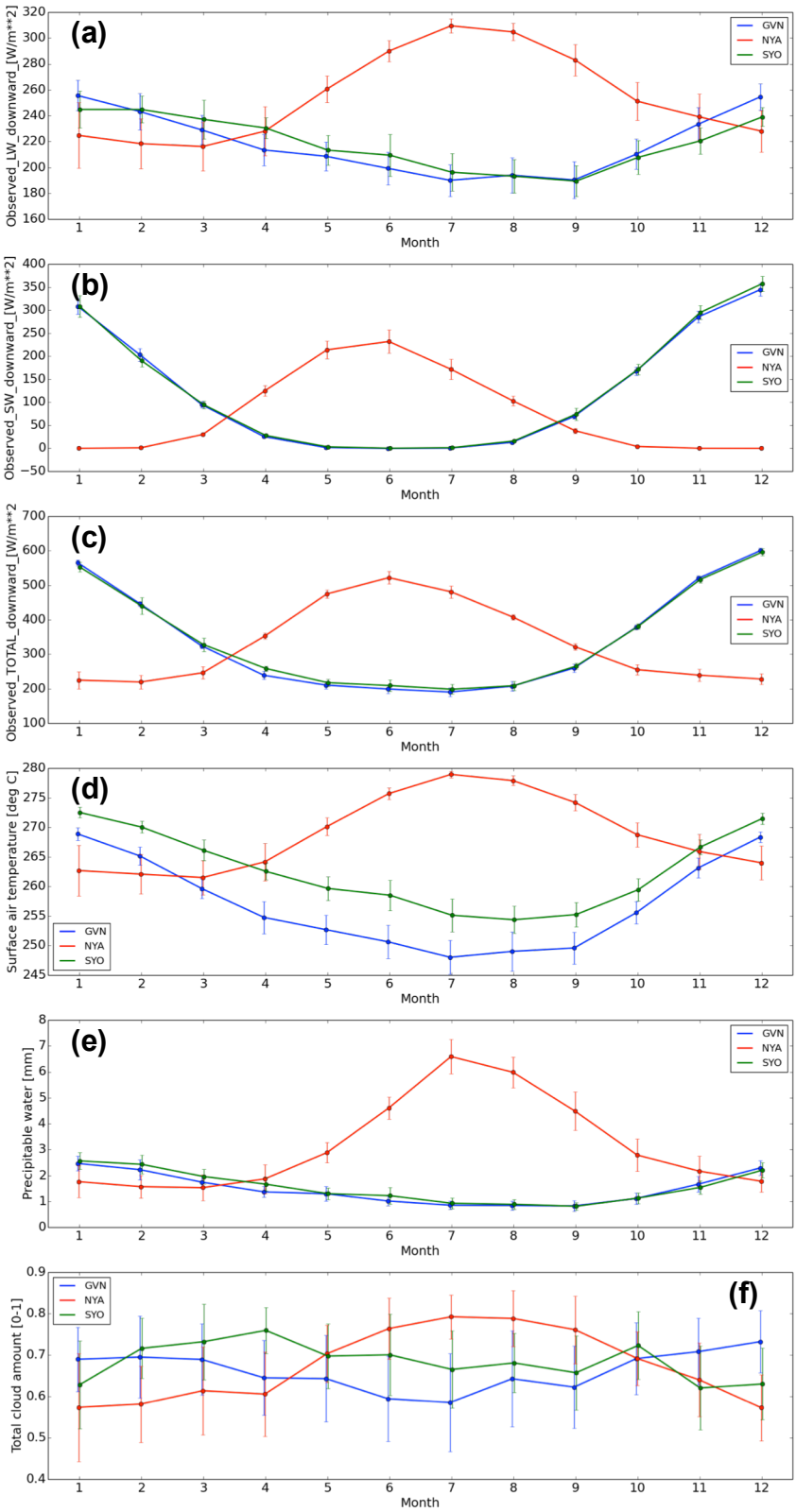

Figure 4.13. Seasonal cycles of L_D (a), S_D (b), T_D (c), T_S (d), PW (e), and (f) CF_{Total} at NYA, SYO, and GVN.

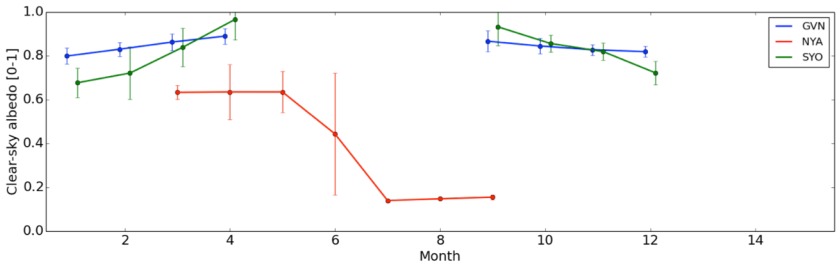

Figure 4.14. Clear-sky albedo estimated from the in situ observed upward shorwave radiation and S_D under clear-sky conditions.

radiation and S_D.

Seasonal cycles of longwave and shortwave radiation at GVN and SYO are similar. The small difference in L_D at GVN compared with SYO is slightly larger in summer (November to January) by 8 to 15 W m^{-2} and smaller in autumn and winter (March to July) by 5 to 17 W m^{-2} with monthly mean averages. The monthly mean T_S is from 249 to 269 K at GVN and 254 to 273 K at SYO. Both stations record maximum temperatures from December to January of 268 to 269 K at GVN and 271 to 273 K at SYO, and minimum temperatures from July to September of 248 to 250 K at GVN and 254 to 255 K at SYO. Seasonal cycles of PW are similar at GVN and SYO. PW at GVN and SYO are 0.8 to 2.5 and 0.8 to 2.7 mm, respectively. The maximum and minimum PW values are recorded in January and September, respectively.

Figure 4.15 compares the estimation of CF_{Total} over NYA, SYO, and GVN for 2007 to 2009. Active sensors (ceilometer or lidar) provide similar seasonal cycles to visual observations. CF_{Total} obtained by visual observation is larger by about 0.1, which suggests that it is also caused by the small amount of sunlight. Radiosonde observations also provide a similar seasonal cycle for CF_{Total}, except from June to July, when the cloud fraction obtained by lidar and visual observations decrease from the previous month. CF_{Total} obtained by radiosonde observations in June and July increases from May. In general, CF_{Total} at NYA estimated by in situ observations (visual, lidar, radiosonde, and camera) shows similar seasonal cycles, that is, an increase in summer

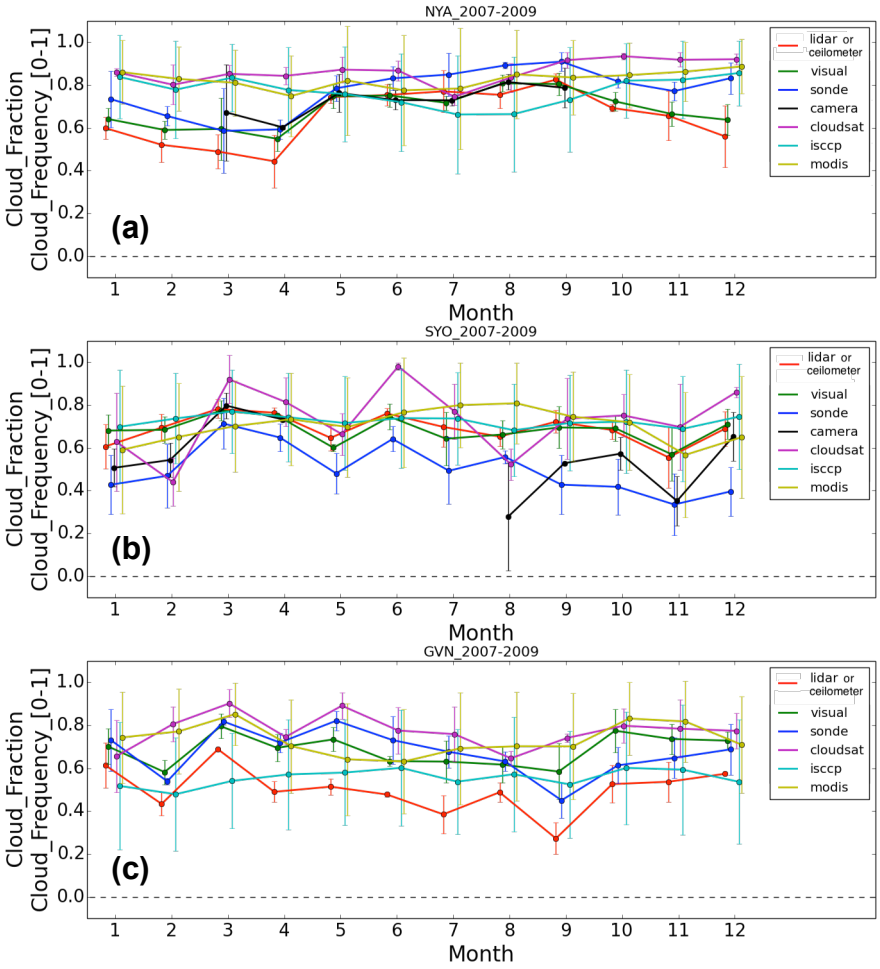

Figure 4.15. Comparison of CF_{Total} obtained by lidar/ceilometer, visual observations, radiosonde estimation, camera retrieval, CloudSat-CALIPSO, ISCCP, and MODIS at (a) NYA, (b) SYO, and (c) GVN for 2007 to 2009.

and a decrease in winter. However, the satellite retrievals show different seasonal cycles, which are large and constant at 0.7–0.9 and decrease in summer.

At SYO, CF_{Total} estimated by micro pulse lidar (MPL) varies from 0.6 to 0.8. The maximum and minimum of CF_{Total} are found in March and November, respectively. The visual observations correspond to the lidar observations. The other in situ estimations, namely camera and radiosonde estimations, underestimate CF_{Total} by 0.1 to 0.2. MODIS and ISCCP retrievals are generally consistent with visual and lidar estimations,

although some months in winter or spring show small overestimations. CloudSat-CALIPSO shows a large difference compared with the other instruments.

Because the range of the ceilometer at GVN is limited to below 3600 m and it detects only low and lower-middle clouds, CF_{Total} estimated by the ceilometer is smaller than that estimated by the other in situ instruments. Apart from the underestimation of the active sensor, the seasonal cycles of the in situ estimations of CF_{Total} are similar; the maximum is in March and the minimum is in September. Variations in CF_{Total} in the other months are weak. Visual observation and radiosonde estimates show good agreement from summer to autumn. Visual observations overestimate CF_{Total} in winter and spring because of the uncertainty caused by the small amount of sunlight, as at SYO. CF_{Total} evaluated by MODIS and ISCCP retrievals are larger than for the visual observations, and the CloudSat-CALIPSO product shows a similar seasonal cycle, although in January and September it shows a large overestimation of 0.1 to 0.3 compared with visual observations.

The frequencies of low, middle, and high clouds estimated by active sensors at NYA, SYO, and GVN are shown in Figure 4.16. Low, middle, and high clouds are defined as clouds with altitudes less than 2000, 6000, and 12,000 m, respectively. In NYA, the proportion of low cloud is larger than half the total cloud, and the seasonal cycle of total cloud is mainly caused by changes in low cloud. Low cloud reaches a maximum in May with a cloud fraction of 0.6, which is 75% of total cloud. From June to September, the cloud frequency of low cloud decreases from May by 0.1 to 0.2. Middle and high clouds increase in this season, and total cloud frequency is similar to that of May. Therefore, CF_{Total} obtained by lidar reaches a maximum in September, not in May.

Low cloud is also dominant at SYO. The percentage of low cloud is 50 to 70% of total cloud. Middle cloud increases for winter up to a cloud fraction of 0.2. The high cloud fraction is larger than 0.1 from winter to spring. Because the GVN ceilometer is limited to below 3600 m, it estimates a large low cloud frequency.

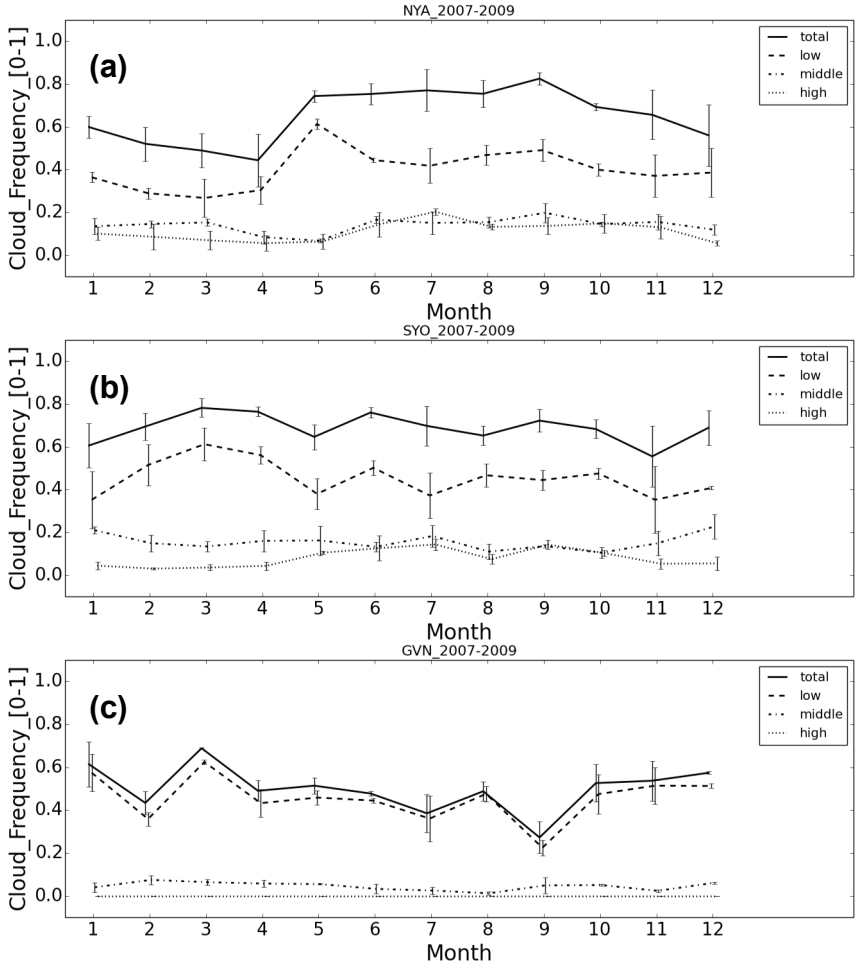

Figure 4.16. Seasonal cycle of cloud fraction for the low, middle, high, and total cloud by lidar at (a) NYA, (b) SYO, and (c) GVN.

Based on these results, the seasonal change of CF_{Total} is mainly controlled by low cloud. Figure 4.17 compares $CF_{Low\text{-}Middle}$ obtained by lidar or ceilometer, visual observation, radiosonde estimation, and CloudSat-CALIPSO. At NYA, visual and lidar observations agree well. The visual observation for winter shows a small underestimation. $CF_{Low\text{-}Middle}$ obtained by visual observation is similar to that obtained by lidar from spring to autumn. The seasonal cycle is similar, whereas radiosonde $CF_{Low\text{-}Middle}$ overestimates the low and middle clouds by 0.1 to 0.3. $CF_{Low\text{-}Middle}$ retrieved by CloudSat-CALIPSO shows different seasonal cycles.

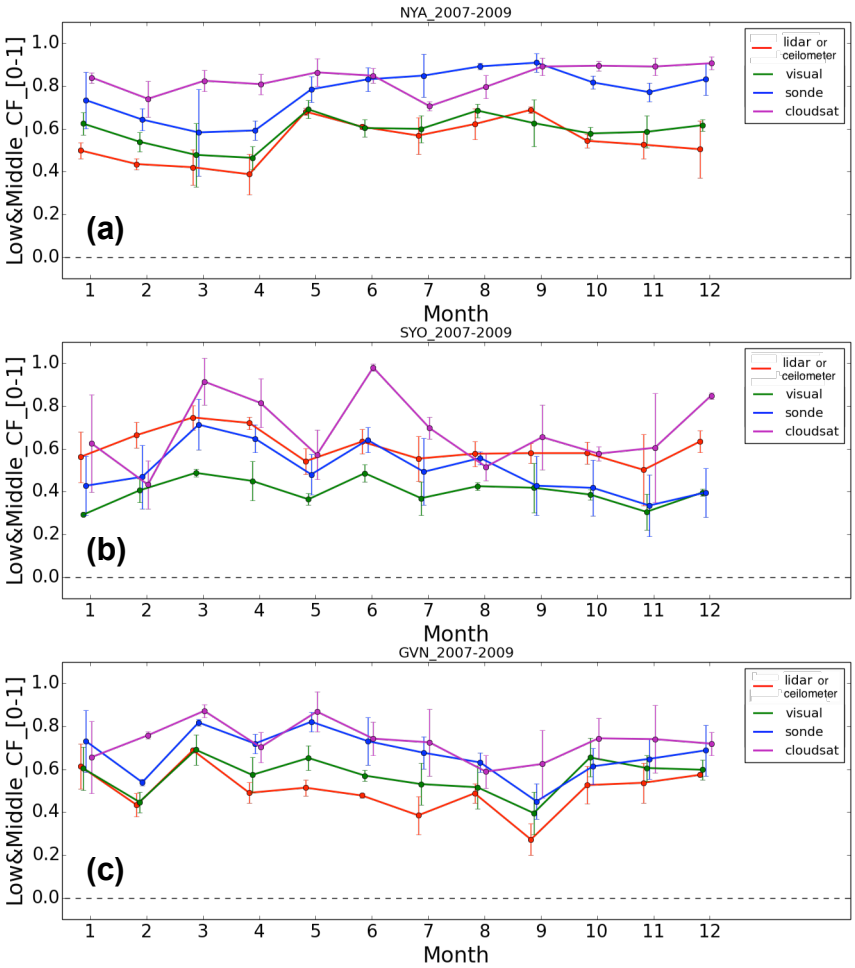

Figure 4.17. Comparison of $CF_{Low\text{-}Middle}$ obtained by lidar/ceilometer, visual observation, radiosonde estimation, camera retrieval, CloudSat-CALIPSO, ISCCP, and MODIS at (a) NYA, (b) SYO, and (c) GVN for 2007 to 2009.

Compared with lidar, visual observation underestimates $CF_{Low\text{-}Middle}$ at SYO. However, CF_{Total} values obtained by visual observation and lidar are similar. It is likely that visual observation overestimates high cloud. Radiosonde observation agrees with lidar from March to August. In summer, visual observations underestimate CF_{Total} by about 0.2. Because CF_{Total} obtained by radiosonde is also smaller than CF_{Total} obtained by lidar for all seasons, radiosonde misses cloud all cloud types and it is frequently for low cloud.

At GVN, $CF_{Low\text{-}Middle}$ estimated by ceilometer, which can detect only below 3600 m, varies from 0.2 to 0.7. Visual observation shows good agreement with ceilometer measurements in summer. In the other seasons, CF_{Total} is underestimated by visual observation by around 0.1. The underestimation may be caused by the missing middle cloud with altitudes higher than 3600 m, and by the long nights in the Antarctic winter preventing precise observations. CloudSat-CALIPSO overestimates $CF_{Low\text{-}Middle}$ substantially, in the same way as CF_{Total}.

Figure 4.18 compares CBH estimated by lidar or ceilometer, radiosonde, and CloudSat-CALIPSO at NYA, SYO, and GVN. CBHs estimated by active

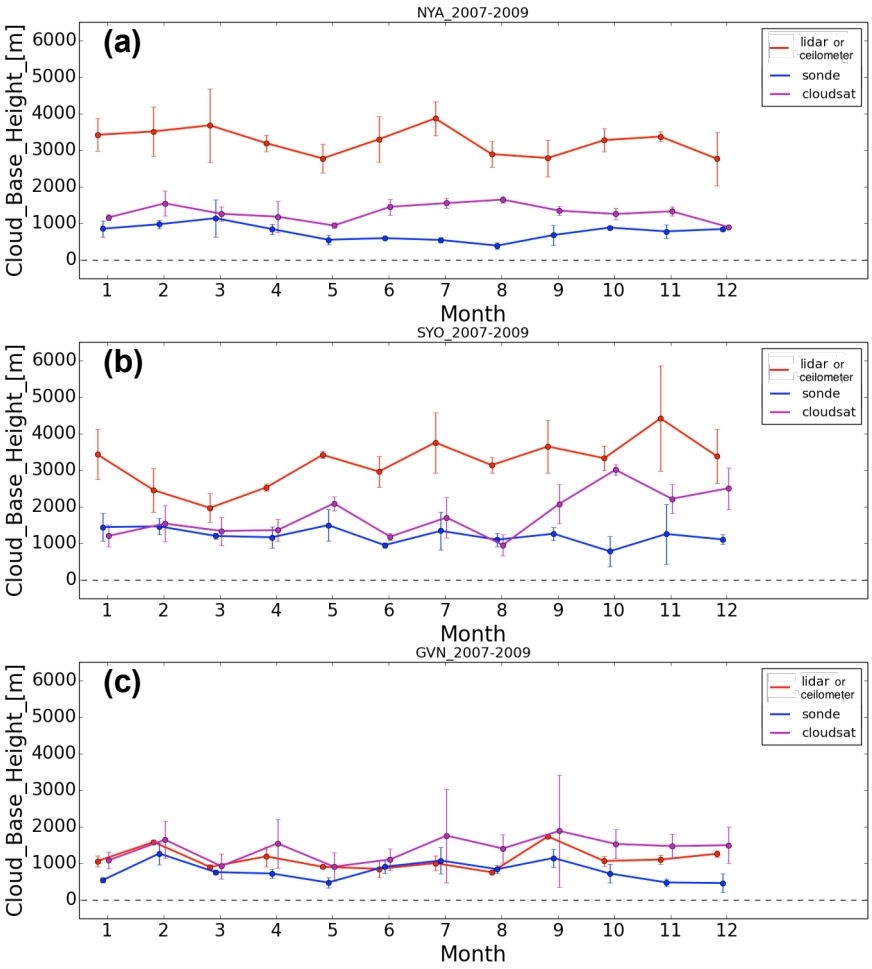

Figure 4.18. Comparison of $CF_{Low\text{-}Middle}$ obtained by lidar/ceilometer, visual observation, radiosonde estimation, camera retrieval, CloudSat-CALIPSO, ISCCP, and MODIS at (a) NYA, (b) SYO, and (c) GVN for 2007 to 2009.

sensors are higher than radiosonde and CloudSat-CALIPSO retrievals except for at GVN, which uses an LD-WHX ceilometer with a limited range. At NYA, the seasonal average obtained by lidar shows a higher CBH for late winter to early spring and for summer. Compared with surface lidar observations, CBHs estimated by radiosonde and CloudSat-CALIPSO are lower by 2000 to 3000 m. The seasonal cycle of CBH obtained by radiosonde agrees with the lidar observations in early spring and autumn. CBH estimated by radiosonde is high for summer. However, CBH estimated by CloudSat-CALIPSO for summer is smaller than for the other seasons. The seasonal cycle of CBH in estimating CloudSat-CALIPSO does not agree with that of lidar in early spring and autumn.

At SYO, the monthly mean cloud base height is observed from 2000 to 4500 m by MPL. The maximum and minimum CBH occur in November and March, which correlate to the minimum and maximum cloud frequencies. Similar to GVN, cloud estimated by radiosonde is mostly low cloud, and the CBH is different from the lidar CBH. CBH evaluated by CloudSat-CALIPSO is underestimated by 100 to 3000 m and the seasonal cycle does not correspond to that obtained by lidar. CBH estimated by radiosonde does not correspond to that obtained by lidar.

Monthly mean CBH obtained by ceilometer is lower than 2000 m in all months at GVN because of the limited range. Radiosonde estimation underestimates CBH by 500 to 1000m compared with lidar observations, although the seasonal cycles are similar. The CloudSat-CALIPSO product shows good agreement with the seasonal variation of the ceilometer CBH except in July and September, when the measurements have a large standard deviation.

In summary, in polar regions, cloud fraction obtained by visual observation is generally consistent with that obtained by lidar observation despite the small overestimation or underestimation in winter for total and low-middle cloud. Radiosonde estimation tends to overestimate cloud fraction and underestimate CBH. Camera retrieval agrees with active sensor observations for summer. Satellite retrievals do not agree, in contrast to mid-latitude regions.

Figure 4.19 shows the seasonal cycles of CRC to L_D, S_D, and T_D in polar regions. At NYA, CRC to L_D remains at 16 to 18% and the seasonal cycle is weak. The maximum CRC to L_D is in May, which corresponds to the maximum CF_{Total} and CF_{Low} obtained by lidar. The minimum CF_{Total} obtained by lidar is in April. CRC to S_D at NYA ranges from 27 to 50%.

CRC to L_D at SYO ranges from 12 to 19%, and shows a large seasonal change; CRC in the Antarctic summer is at a minimum and the other seasons show a relative large CRC, which corresponds to the low frequency of CF_{Total} in November and January. Seasonal changes in CF_{Total} also affect S_D. Although S_D in the Antarctic summer is large, CRC to S_D is at a minimum of 11% in December. CRC to S_D ranges from 11 to 32%. The month

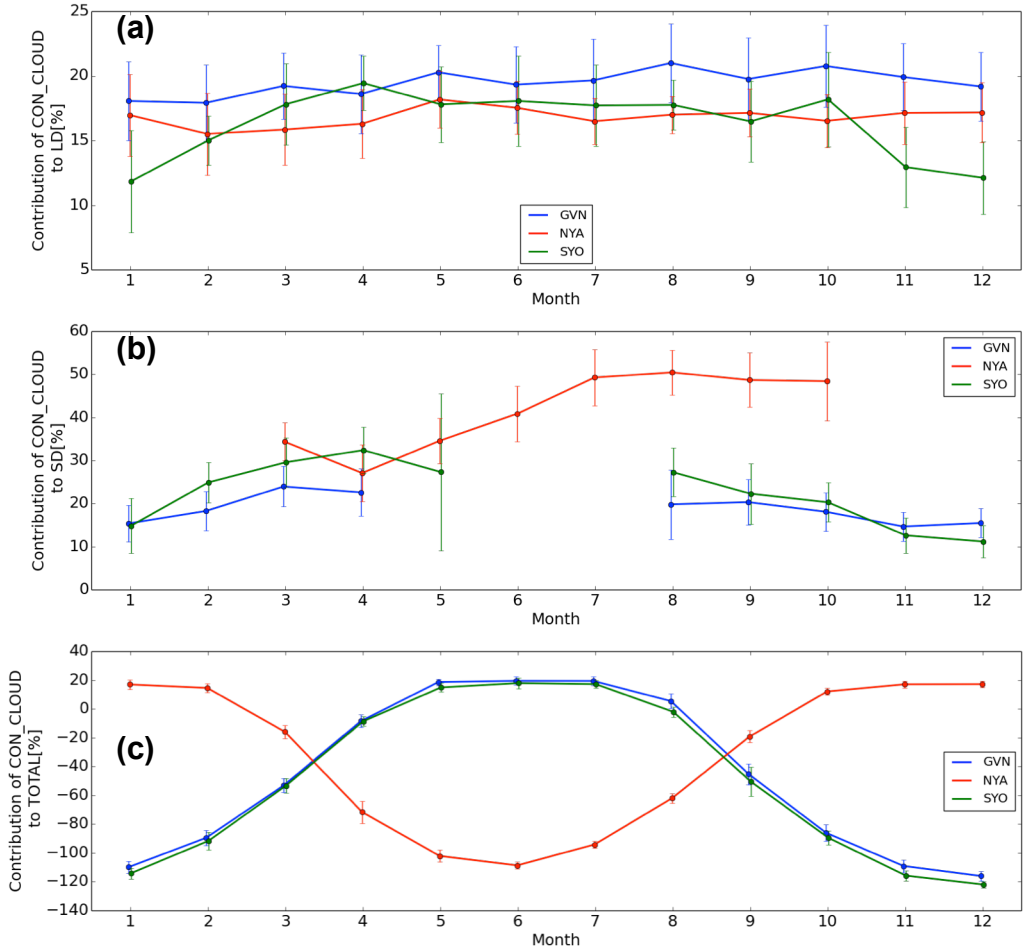

Figure 4.19. Seasonal mean CRC for (a) L_D, (b) S_D, and (c) T_D at GVN, NYA, and SYO.

when the maximum CRC to S_D occurs is different from that of the maximum CF_{Total}, but the same as that of the maximum CRC to L_D.

Seasonal changes in CRC to L_D and S_D at GVN are smaller than those at SYO. CRC to L_D is 18 to 21% and CRC to S_D is 15 to 24% at GVN; thus, the CRC to L_D at GVN is larger than at SYO. CF_{Total} at GVN is smaller than at SYO, although low temperatures and small amounts of PW reduce the effect of cloud. However, CRC to S_D at GVN is smaller than at SYO, except for summer, when the amount of cloud over SYO decreases.

In the polar region, the monthly mean averages of L_D range from 10 to 20%. For S_D, CRC at NYA ranges from 30 to 50%, and the Antarctic region ranges from 10 to 30%. For T_D, CRC ranges from -120 to +20%, and the positive maximum is in summer and the negative maximum is in winter. The difference in CRC to T_D between GVN and SYO is small.

4.2.2 Inter-annual variations in polar regions

Figure 4.20 shows the inter-annual trends of L_D, S_D, T_D, CRC, CF_{Total}, $CF_{Low\text{-}Middle}$, CBH, T_S, PW, and diffuse and direct shortwave radiation with seasonal change subtracted at GVN from 1992 to 2013, NYA from 1994 to 2014, and SYO from 1998 to 2013.

4.2.2.1 NYA, Arctic coastal region

Table 4.12 shows the monthly mean trends of L_D, S_D, T_D, CRC, CF_{Total}, $CF_{Low\text{-}Middle}$, CBH, T_S, PW, and shortwave diffuse and direct radiation with seasonal correction at NYA from 1994 to 2014. The L_D increases satisfy the 95% confidence level, and the increase rate is 5.54 W m^{-2}/decade. CF_{Total} estimated visually and by radiosonde increase. However, the trend in CF_{Total} obtained by visual observation satisfies the 95% confidence level. Moreover, the cloud fraction estimated by radiosonde is unreliable in the polar region.

The increase in L_D is not caused by the increase in cloud amount because both the CRC and CF_{Total} obtained by visual observation do not show significant increasing trends. T_S and PW show increasing trends satisfying the 95% confidence level. The increase rates of 1.30 K/decade and 0.26

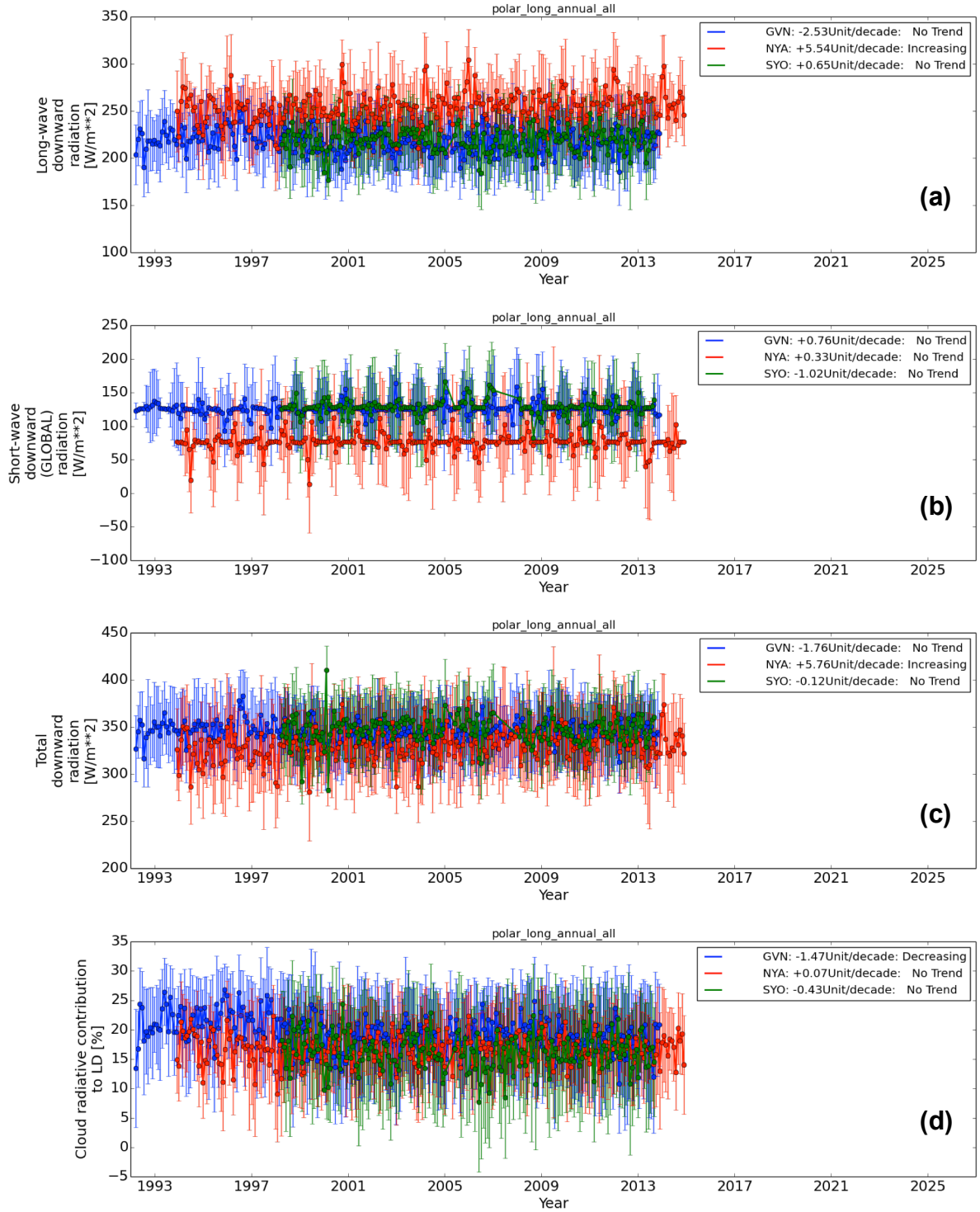

Figure 4.20. Monthly means of (a) L_D, (b) S_D, (c) T_D, (d–f) CRC, (g) CF_{Total}, (h) $CF_{Low\text{-}Middle}$, (i) shortwave diffuse, (j) direct, (k) T_S, and (l) PW at GVN, NYA, and SYO with seasonal effects subtracted.

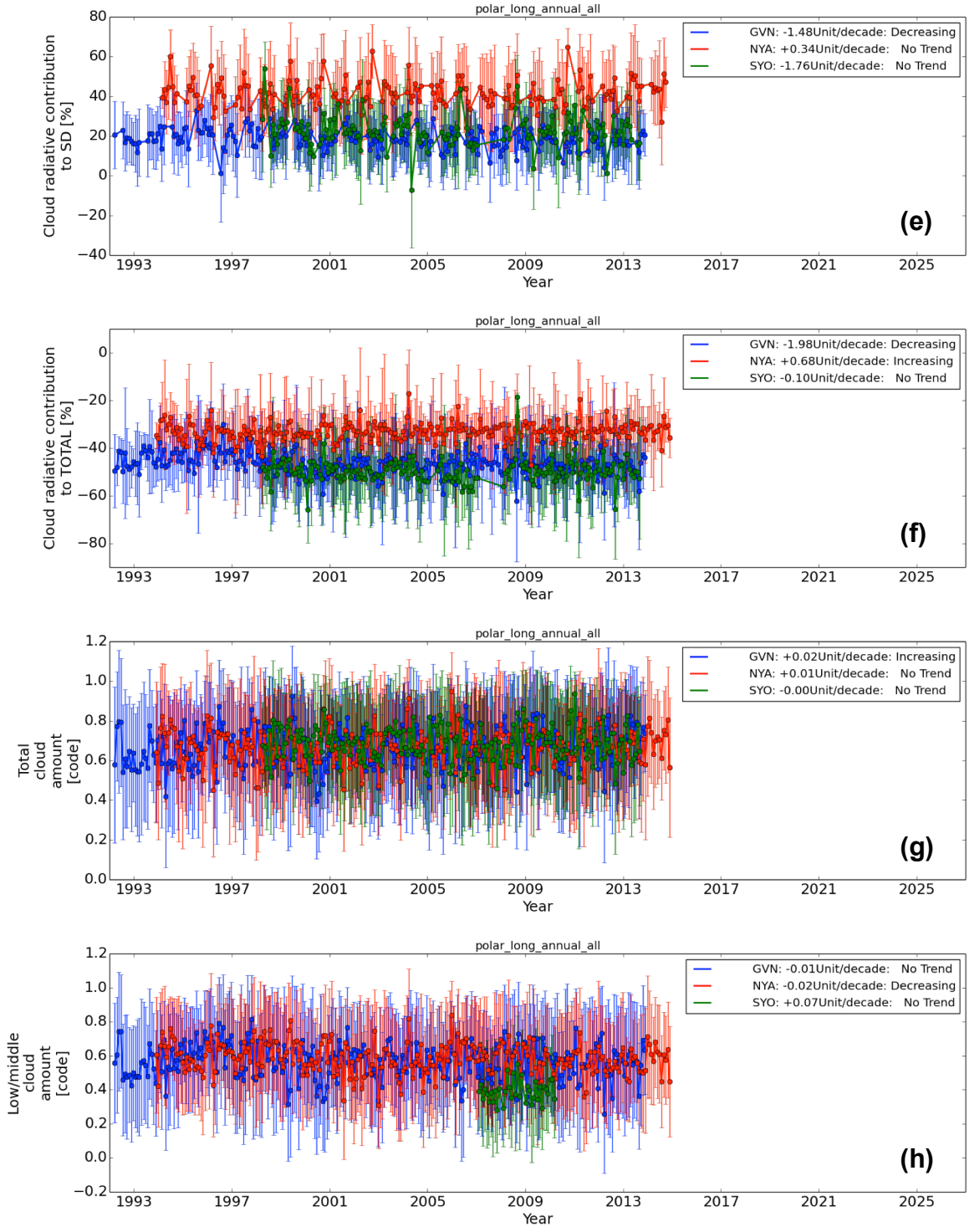

Figure 4.20. Continued.

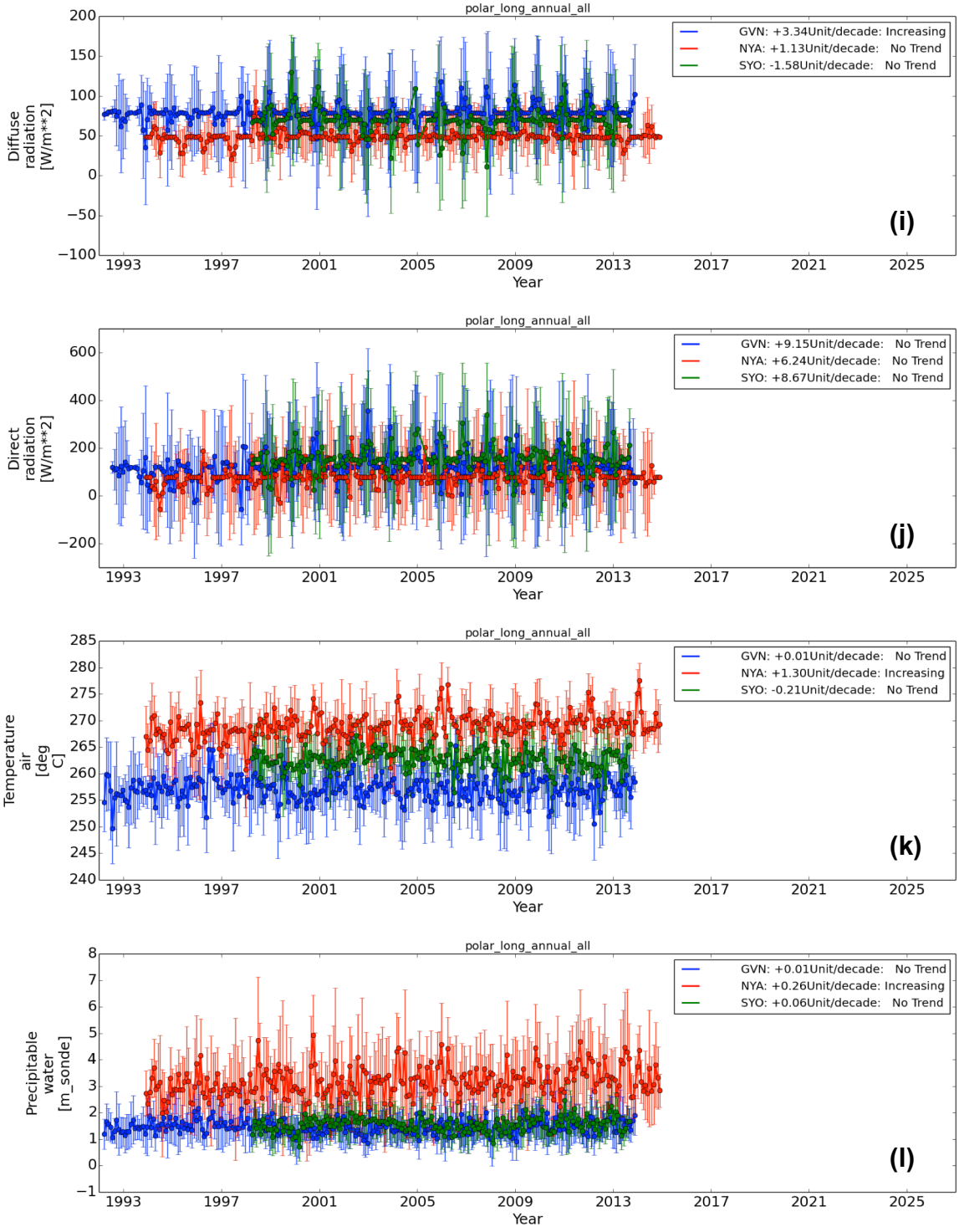

Figure 4.20. Continued.

mm/decade contribute to an increase in L_D of 75% under clear-sky conditions and 66% under all-sky conditions, respectively, in the radiative transfer model. The large increases in temperature and amount of WV cause an increase in L_D with decreasing $CF_{Low\text{-}Middle}$.

Eastman and Warren (2010) investigated the inter-annual change of cloud in Arctic regions by using records from the 638 synoptic stations from 1971 to 2007 over land and 1954 to 2008 over sea. They showed an increase in precipitation low cloud over land, but a decrease in precipitation cloud

Table 4.12. Monthly mean trends (revised seasonal) at NYA from 1994 to 2014 under all-sky conditions [/decade].

		Annual	Spring	Summer	Autumn	Winter
L_D	Flux [W m^{-2}]	**+5.54**	+1.21	-1.11	+6.14	**+13.4**
	CRC [%]	+0.07	+0.22	**-1.24**	+0.47	+0.46
S_D	Flux [W m^{-2}]	+0.33	-4.98	+7.47	-1.18	-0.02
	CRC [%]	+0.34	**+2.11**	**-2.74**	+2.70	NaN
T_D	Flux [W m^{-2}]	**+5.76**	-3.94	+6.35	+4.75	**+13.4**
	CRC [%]	+0.68	+1.04	-1.39	**+1.46**	+0.46
CF_{Total} [0-1]	Visual	+0.01	+0.01	-0.02	+0.01	+0.03
	Sonde	**+0.13**	**+0.15**	+0.04	**+0.11**	**+0.20**
$CF_{Low\text{-}Middle}$ [0-1]	Visual	**-0.02**	-0.01	**-0.06**	**-0.03**	+0.00
	Sonde	**+0.13**	**+0.15**	+0.04	**+0.11**	**+0.20**
CBH [km]	Sonde	+0.05	**+0.12**	+0.00	+0.01	+0.05
Temperature [K]		**+1.30**	+0.64	**+0.49**	+0.85	**+2.93**
Precipitable Water [mm]		**+0.26**	+0.08	+0.26	**+0.29**	**+0.33**
Diffuse [W m^{-2}]		+1.13	+0.93	+3.65	-0.23	+0.07
Direct [W m^{-2}]		+6.24	-6.05	**+31.4**	+0.19	-0.18

over sea. In the present study, NYA in the Arctic coastal region shows a decrease in low or middle cloud except for in winter. Therefore, the climate over NYA is strongly affected by the sea.

Although $CF_{Low\text{-}Middle}$ shows a reliable decreasing trend, S_D and CRC do not show significant trends in the annual mean. $CF_{Low\text{-}Middle}$ decreases significantly from summer to autumn (Table 4.12). In summer, the significant decrease in $CF_{Low\text{-}Middle}$ increases S_D by +7.47 W m^{-2}/decade and decreases the CRC to S_D by -2.74%/decade. The decrease in CRC to S_D satisfies the 95% confidence level. S_D and the CRC for autumn show no significant trends because of the smaller amount of sunlight.

4.2.2.2 GVN and SYO, Antarctic coastal region

Tables 4.13 and 4.14 show the inter-annual changes of L_D, S_D, T_D, CF_{Total}, $CF_{Low\text{-}Middle}$, CBH, T_S, PW, and direct and diffuse shortwave radiation at GVN from 1992 to 2013 and at SYO from 1998 to 2013. Monthly means of L_D and S_D do not show clear trends at the Antarctic coastal stations.

The decrease in L_D is -2.53 W m^{-2}/decade and the increase in S_D is +0.76 W m^{-2}/decade at GVN. The rates of change are small and the trends do not satisfy the 95% confidence level. However, CRCs to L_D and S_D show reliable trends satisfying the 95% confidence level, with rates of change of -1.47 and -1.48%/decade, respectively, for the full year. However, the inter-annual variation of CF_{Total} obtained by visual observation increases, with the 95% confidence level. The trend in CF_{Total} shows the opposite effect on the surface radiative fluxes because the increasing amount of cloud should increase the CRC. The opposite effect of CRC on CF_{Total} is caused by decreasing $CF_{Low\text{-}Middle}$.

The decrease in $CF_{Low\text{-}Middle}$ obtained by visual observation is -0.01/decade and is small in the annual means. $CF_{Low\text{-}Middle}$ for winter shows a large decrease of -0.04/decade. Winter also shows reliable trend of decreasing CRC to L_D of -2.57 W m^{-2}/decade. The trend for CRC to S_D does not satisfy the 95% confidence level because of insufficient shortwave

radiation in winter, although the decrease in CRC to S_D is very large. Based on these results, the decreasing CRC throughout the year at GVN, in the northern Antarctic coastal region, is mainly caused by decreases in low and middle clouds for winter. Although CF_{Total} increases, the effect of the trend on the surface radiative flux trend is small. Because CBH estimated by radiosonde shows an increasing trend with the 95% confidence level, the decrease in $CF_{Low\text{-}Middle}$ corresponds to the increase in CF_{Total}. However, the

Table 4.13. Monthly mean trends (with seasonal correction) at GVN from 1992 to 2013 under all-sky conditions [/decade].

		Annual	Spring	Summer	Autumn	Winter
L_D	Flux [W m^{-2}]	-2.53	-2.82	-3.55	+2.75	-4.99
	CRC [%]	**-1.47**	-1.40	-1.32	-0.06	**-2.57**
S_D	Flux [W m^{-2}]	+0.76	+0.49	+1.20	+0.03	+0.27
	CRC [%]	**-1.48**	-0.73	-0.96	-0.95	-5.25
T_D	Flux [W m^{-2}]	-1.76	-2.17	-2.44	+2.60	-4.70
	CRC [%]	**-1.98**	-2.01	-0.64	-0.74	**-3.04**
CF_{Total} [0-1]	Visual	**+0.02**	+0.01	+0.00	**+0.05**	+0.01
	Sonde	**+0.04**	+0.01	+0.05	**+0.06**	+0.05
$CF_{Low\text{-}Middle}$ [0-1]	Visual	-0.01	-0.00	-0.00	+0.00	-0.04
	Sonde	**+0.04**	+0.01	+0.04	**+0.06**	+0.05
CBH [km]	Sonde	**+0.31**	**+0.30**	**+0.23**	**+0.25**	**+0.45**
Temperature [K]		+0.01	-0.03	+0.28	+0.50	-0.56
Precipitable Water [mm]		+0.01	+0.02	-0.00	**+0.10**	-0.00
Diffuse [W m^{-2}]		**+3.34**	+4.44	**+9.86**	+0.98	-0.30
Direct [W m^{-2}]		+9.15	+13.5	+10.0	+1.27	+3.11

accuracy of CBH obtained by radiosonde is not validated at GVN because the active sensor at GVN detects only low cloud and some middle cloud. At the other stations, radiosonde tends to underestimate CBH in the polar regions.

Similar to GVN, L_D and S_D show no reliable trends at SYO in the annual means, and the CRC shows a decreasing trend. However, there are no reliable trends in CRC, CF_{Total}, and CBH at SYO. $CF_{Low\text{-}Middle}$ is observed for only a limited period that is not sufficient to evaluate the trend. CRC to L_D

Table 4.14. Monthly mean trends (revised seasonal) at SYO from 1998 to 2013 under all-sky conditions [/decade].

		Annual	Spring	Summer	Autumn	Winter
L_D	Flux [W m^{-2}]	+0.65	-3.41	+6.75	-4.35	+0.84
	CRC [%]	-0.43	**-2.61**	+0.55	-1.00	+0.34
S_D	Flux [W m^{-2}]	-1.02	+2.52	-5.09	+0.16	-0.38
	CRC [%]	-1.76	-1.99	+0.44	-2.82	+4.89
T_D	Flux [W m^{-2}]	-0.12	-0.24	-0.77	-1.48	+0.54
	CRC [%]	-0.10	-3.02	+1.61	-1.30	+0.89
CF_{Total} [0-1]	Visual	-0.00	-0.06	+0.02	-0.00	+0.01
	Sonde	+0.03	-0.01	+0.07	+0.03	+0.03
$CF_{Low\text{-}Middle}$ [0-1]	Visual	NaN	NaN	NaN	NaN	NaN
	Sonde	+0.03	-0.01	+0.07	+0.03	+0.03
CBH [km]	Sonde	-0.07	-0.00	-0.05	-0.11	-0.04
Temperature [K]		-0.21	+0.36	+0.47	**-1.09**	-0.02
Precipitable Water [mm]		+0.06	+0.04	+0.31	-0.02	-0.13
Diffuse [W m^{-2}]		-1.58	-7.97	+0.95	**+2.82**	+0.31
Direct [W m^{-2}]		-8.67	**+51.1**	-19.8	+10.3	-0.72

only in spring shows a decreasing trend satisfying the 95% confidence level, and the rate of change is -2.61%/decade. For the season, the decrease in CF_{Total} obtained by visual observation is larger by -0.06 and the direct shortwave radiation increases satisfying the 95% confidence level.

The increase in L_D in summer at SYO is +6.75 W m^{-2}/decade, which is large. Because of the small change of CF_{Total} and the large increase in PW by +0.31 mm/decade, the large increase in L_D in summer is caused by the increase in WV resulting from the humid wind. Figure 4.21 shows the 2D histograms of wind direction for wind speed and PW at SYO from 1998 to 2013. SYO is affected by the two types of wind. The wind from 45 to 90° is fast, humid, and from the ocean, whereas the wind from 90 to 210° is dry and calm. Recently, the wind from 45–90° has been more humid than during the second half of 1990s at SYO (Figure 4.22). The circulation changes with humidity and wind arise from the Southern Hemisphere Annular Mode (Thompson and Solomon, 2002; Gillett and Thompson, 2003), which is caused by stratospheric ozone depletion.

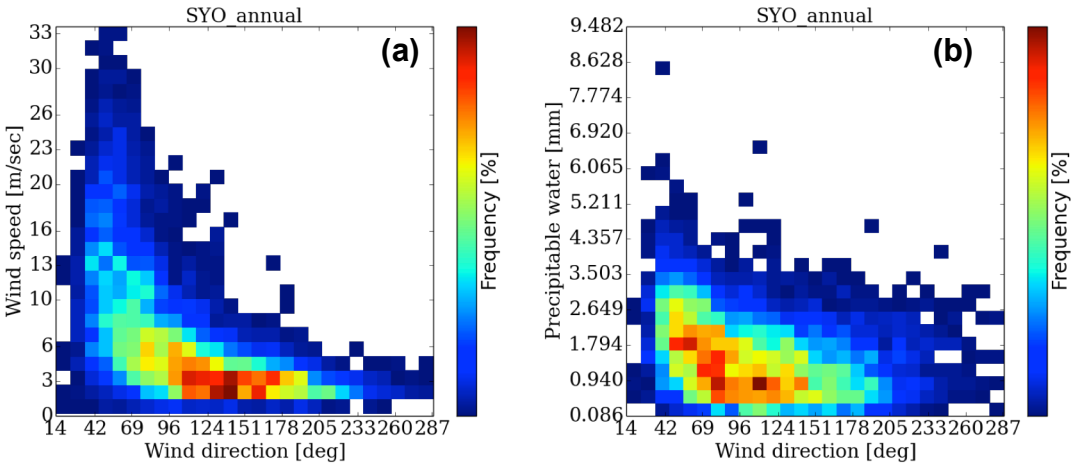

Figure 4.21. Frequencies of wind direction for (a) wind speed and (b) PW at SYO from 1998 to 2013.

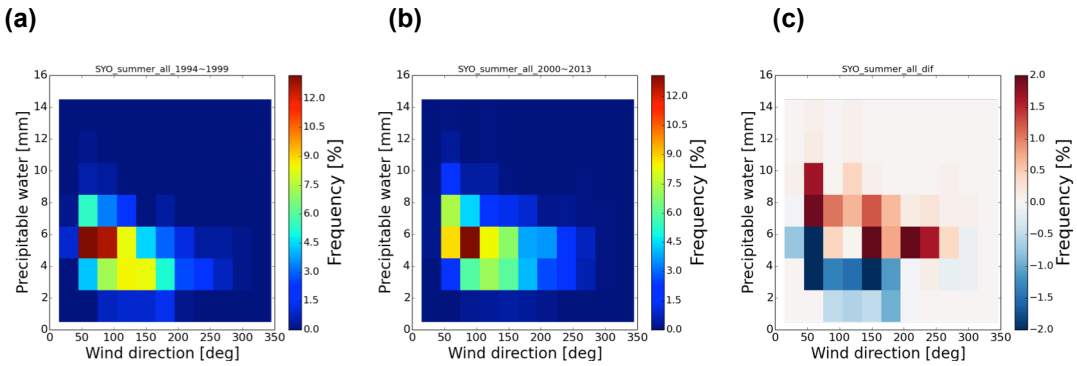

Figure 4.22. Frequencies between wind direction and PW at SYO from (a) 1994 to 1999 and from (b) 2000 to 2013, and (c) is the difference between (a) and (b).

4.3. Comparison of mid-latitude and polar regions

The inter-annual trend in downward radiation has been investigated in previous studies. Wang and Liang (2009) compared L_D between in situ observed values at 36 observatories and calculated values for 1996 to 2007. They used a parameterization method adapted from Brunt (1932) and Brusaert (1975), which uses the T_S and water vapor pressure. They considered the cloud effect by using the method reported by Crawford and Duchon (1992). They concluded that this method showed good agreement with observations. They evaluated the global mean L_D with the Brunt method by parameterizing 3200 observations for 1973 to 2008. The increasing trend is +2.2 W m^{-2}/decade for the monthly mean average. Prata (2008) calculated L_D with MODTRAN-3 (Berk et al., 1989) by using the monthly mean vertical profiles of air temperature and WV assuming clear-sky conditions at 136 observatories belonging to the National Center for Atmospheric Research. They showed that the global mean T_S, PW, and L_D increase by 0.22 K/decade, 0.29 mm/decade, and 1.67 W m^{-2}/decade, respectively. The increasing trend is larger in the equator region than at the mid latitude and polar regions. Wild et al. (2008) estimated the mean

increase in global L_D from 1992 to 2000 from observed data at 12 BSRN stations as 2.6 W m^{-2}/decade.

Gilgen et al. (1998) estimated the trend in the surface S_D by using the observed value of the Global Energy Balance Archive for the monthly mean and they found that the average decrease is approximately -2%/decade. Hatzianastassiou et al. (2005) evaluated the increase of S_D at the surface for 17 years (1984 to 2000) on the monthly average by radiative transfer calculations with 2.5° resolution. The input data is long-term climatological data from ISCCP-D2. S_D showed a significant increase of 2.4 W m^{-2}/decade for 1984 to 2000.

In the present study, we investigated the inter-annual variability of L_D, S_D, and T_D at six observatories in the European continental (LIN and PAY), East Asia coastal (TAT), Arctic coastal (NYA), and Antarctic coastal regions (SYO and GVN) with observation periods longer than ten years. The European continental, East Asia coastal, and Arctic coastal regions show increasing trends for L_D. These trends, except for in the Arctic coastal region, do not satisfy the 95% confidence level. The increase in the Arctic coastal region is +5.54 W m^{-2}/decade and is much larger than the global average from previous studies. The reason for the significant increase in L_D in the Arctic is discussed by comparison with the trend in the mid-latitude region.

The main reason for the significant increase in L_D at NYA in the Arctic coastal region is the significant increase in T_S and PW by 1.30 K/decade and 0.26 mm/decade, respectively. If the tropospheric air temperature and PW increase by 1.30 K and 0.26, respectively, in the mstrnX radiative transfer model from the measurements at NYA under clear-sky conditions, L_D increases by 4.4 W m^{-2}. The increase L_D is very near to the increase in the observation at NYA of 5.5 W m^{-2}/decade. T_S and PW at LIN in the European continental region also show increases that satisfy the 95% confidence level. The increases are 1.20 K/decade for T_S and 0.37 mm/decade for PW, which are large. If tropospheric air temperature and PW increase by 1.20 K and 0.37 mm, respectively at LIN under clear-sky conditions, L_D increases by 4.9 W m^{-2}. The calculated increase is much larger than the observed value. Calculations cannot reproduce the observed value at LIN assuming clear-sky

conditions, because one of the reasons that there is no significant increase in L_D is cloud.

In the European and Arctic regions, $CF_{Low\text{-}Middle}$, an important absorber of longwave radiation, decreases at the 95% confidence level. The decrease in low or middle cloud should decrease L_D. The Arctic shows a significant annual increase in L_D. A weak decreasing trend of $CF_{Low\text{-}Middle}$ is mainly found in summer. In winter, when the low-middle cloud does not decrease, the increasing trend of L_D is dominant.

Only GVN in the Antarctic coastal region shows a decreasing trend in L_D, which is caused by decreases in low or middle cloud in summer or winter. In summer, SYO shows increasing trends in L_D and PW, caused by humid sea wind, whereas GVN does not. In Antarctica, the surface warming is large in west Antarctica (Turner et al., 2005). Both of the target stations in Antarctica in our study are located in east Antarctica, and the result is consistent with the previous study. The surface radiation budget in east Antarctica is mainly controlled by changes in cloud.

S_D shows only weak trends both in the Arctic and Antarctica, even if $CF_{Low\text{-}Middle}$ shows a decreasing trend satisfying the 95% confidence level. Low or middle cloud show changes from autumn to spring, and the long nights reduce the effect of cloud on S_D. In the mid-latitude region, S_D increases because of a decrease in cloud.

Chapter 5

Summary

To investigate the variation of the surface downward radiation and the contributing factors, such as cloud, water vapor (WV), and carbon dioxide (CO_2), the present study calculated downward longwave (L_D) and shortwave radiation (S_D) using radiosonde observation data from the Baseline Surface Radiation Network (BSRN). Radiative transfer was calculated with the vertical air temperature and humidity profiles obtained from radiosonde observations, aerosol optical thickness from the reanalysis product, and the surface albedo estimated by in situ radiation measurements and satellite retrieval. L_D obtained from in situ observations and from the radiative transfer calculations show good agreement with observations, both under clear-sky and overcast conditions. The calculations of S_D are not consistent with the observations under overcast conditions because of insufficient cloud optical thickness. To evaluate the contribution of individual factors, the target factor was removed from the normal atmospheric conditions and the calculated value was compared with the observed value (removal method). The other method for evaluating the radiative contribution is the addition method. The addition method is applied by removing all factors except the target factor from the normal conditions. The radiative contribution obtained by the addition method is calculated for only L_D to evaluate the effect of the overlap of the absorbing factors. The seasonal and inter-annual variations are evaluated precisely and quantitatively, and the results help to clarify the radiation budget and to improve satellite retrieval or numerical climate models.

The results can be summarized as follows.

(1) Under clear-sky conditions, the radiative contribution of WV to L_D

calculated by the removal method (REM_{WV}) ranges from 60% to 71%. The contribution shows strong correlations with surface air temperature (T_S), surface mixing ratio (M_S), and precipitable water (PW). PW shows the strongest correlation with REM_{WV}. The contribution of CO_2 to L_D calculated by the removal method (REM_{CO2}) is small and is 3% to 27% under clear-sky condition. Except for dry, low-temperature conditions, such as those in polar regions, the contribution of REM_{CO2} to L_D is below 20%. The radiative contribution of WV to L_D calculated by the addition method (ADD_{WV}) is very large and ranges from 73% to 97%. The contributions of WV to L_D change little in humid conditions such as in mid-latitude and sub-tropic regions. WV has a large effect on L_D and S_D under clear-sky conditions. REM_{WV} to S_D ranges from 3% to 29%, which is larger than the contribution of aerosols ($REM_{Aerosol}$) by 5% to 7%. The contribution of albedo calculated by the removal method (REM_{Albedo}) is negative, and is up to -10% because a large albedo increases the upward shortwave radiation and S_D in polar and desert regions.

(2) Under overcast conditions, optically thick cloud has a dominant effect on L_D. The radiative contributions of WV and CO_2 to L_D under overcast conditions become much smaller than under clear-sky conditions. The contribution of cloud to L_D calculated by the addition method (ADD_{Cloud}) is frequently near 100%, even in humid sub-tropic or mid-latitude regions. Under overcast conditions, the contributions of WV and cloud are dominant. ADD_{WV} and REM_{Cloud} are related to T_S or PW, whereas REM_{WV} and ADD_{Cloud} correlate with the difference in temperatures between the surface air and cloud base because of large effect of cloud.

(3) Under all-sky conditions without precipitation, the cloud radiative contribution (CRC) to L_D shows large variability with PW, total cloud fraction (CF_{Total}), and cloud base height (CBH). CRC to L_D ranges from -2% to 28%. Even if CF_{Total} is very small, cloud in dry, cold regions has an effect larger than 25%. CRC to S_D ranges from -5% to +85% and the variation depends mainly on CF_{Total}. Overall, CRC ranges from -71% to +27%. The

warming effect of cloud on the surface is larger in polar and desert regions except under near-overcast conditions. The cooling effect is stronger than the warming effect in near-tropic and mid-latitude regions.

(4) The long-term trends in surface radiation, air temperature, humidity, and cloud fraction for polar and mid-latitude regions are compared. Increasing trends in L_D, T_S, and PW at Ny-Ålesund (NYA) in the Arctic coastal area over the last 20 years are dominant. Low-middle cloud fraction ($CF_{Low\text{-}Middle}$) decreases at NYA, although the effect on L_D and S_D is small. Trends in T_S, PW, and $CF_{Low\text{-}Middle}$ at Lindenberg (LIN) and Payerne (PAY) in Europe are similar to NYA; T_S and PW increase and $CF_{Low\text{-}Middle}$ decrease, although increases in L_D at LIN and PAY are negligible. The trend in cloud fraction at Georg von Neumayer Station (GVN) in Antarctica is significant mainly in autumn. The trend affects L_D and S_D. However, the trends in cloud and surface radiation at the other Antarctic station, Syowa (SYO), are not significant in the annual average. Only summer shows a large amount of WV from wind blowing from the sea and L_D increases. The increase in WV during summer at SYO is caused by the circulation change, whereas GVN does not show this trend. The surface radiation budget is more strongly affected by the trend in cloud than by the change in circulation.

References

Anderson, G. P., Clough, S. A., Kneizys, F. X., Chetwynd, J. H., and Shettle, E. P. (1986): "AFGL atmospheric constituent profiles (0.120 km) (No. AFGL-TR-86-0110)", *Technical Report AFGL-TR-86-0110, AFGL (OPI),* Hanscom AFB, MA. 01736.

Alados-Arboledas, L. and Jimenez, J. I. (1988): "Day-night differences in the effective emissivity from clear skies", *Bound.-Layer Meteor*, **45(1-2)**, 93-101.

Berk, A., Bernstein, L. S., and Robertson, D. C. (1987): "MODTRAN: A moderate resolution model for LOWTRAN (No. SSI-TR-124)", *Final Report GL-TR-89- 0122, Geophysics Laboratory*, U.S. Air Force Systems Command, Hanscomb AFB, Massachusetts, USA.

Berk A, Anderson GP, Bernstein Ls, Acharya PK, Dothe H, Matthew MW, Adler-Golden SM, Chetwynd JH Jr., Richtsmeier SC, Pukall B, Allred CL, Jeong LS, and Hoke ML. (1996): "MODTRAN4 Radiative Transfer Modeling for Atmospheric Correction", *SPIE Proceeding, Optical pectroscopic Techniques and Instrumentation for Atmospheric and Space Research* Ⅲ, 3756.

Brunt, D. (1932): "Notes on radiation in the atmosphere", *Quart. J. Roy. Meteor. Soc.*, **58**, 389−418.

Brutsaert, W. (1975): "On a derivable formula for long - wave radiation from clear skies", *Water Resour. Res.*, ***11*(5)**, 742-744.

Crawford, T. M. and C. E. Duchon, (1999): "An improved parameterization for estimating effective atmospheric emissivity for use in calculating daytime downwelling longwave radiation", *J. Appl. Meteorol.*, **38**, 474–480.

Cronin, M. F., Meinig, C., Sabine, C. L., Ichikawa, H., and Tomita, H. (2008): "Surface mooring network in the Kuroshio Extension", *IEEE Syst. J.*, ***2*(3)**, 424-430.

Deacon, E. L. (1970): "The derivation of Swinbank's longwave radiation formula", *Q. J. Roy. Meteor. Soc.*, ***96*(408)**, 313-319.

Dong, X., Xi, B., Crosby, K., Long, C. N., Stone, R. S., and Shupe, M. D. (2010): "A 10 year climatology of Arctic cloud fraction and radiative forcing at Barrow, Alaska", *J. Geophys. Res.-Atmos.*,**115(D17)**.

Doyle, J. G., Lesins, G., Thackray, C. P., Perro, C., Nott, G. J., Duck, T. J., et al. (2011): "Water vapor intrusions into the High Arctic during winter", *Geophys. Res. Lett.*, **38(12).**

Eastman, R., & Warren, S. G. (2010): “Arctic cloud changes from surface and satellite observations”, *J. Climate*, ***23*****(15)**, 4233-4242.

Ebita A, Kobayashi S, Ota Y, Moriya M, Kumabe R, Onogi K et al (2011): “The Japanese 55-year Reanalysis “JRA-55” an interim report”, *Sola*, **7,** 149-152.

Gaffen, D. J. (1994): “Temporal inhomogeneities in radiosonde temperature records”, *J. Geophys”, Res.-Atmos.*, ***99*****(D2)**, 3667-3676.

Gillett, N. P., & Thompson, D. W. (2003): “Simulation of recent Southern Hemisphere climate change. *Science*, ***302*****(5643)**, 273-275.

Gilgen, H., Wild, M., & Ohmura, A. (1998): “Means and trends of shortwave irradiance at the surface estimated from global energy balance archive data”, *J. Climate*, **11(8)**, 2042-2061.

Grant, H. D. (1944). *Cloud and weather atlas*. *Hugh Duncan Gran*t.

Hahn, C. J., Warren, S. G., & London, J. (1995): “The effect of moonlight on observation of cloud cover at night, and application to cloud, climatology”, *J. Climate*, **8(5)**, 1429-1446.

Han, Q., Rossow, W. B., Lacis, A. A. (1994): “Near-global survey of effective droplet radii in liquid water clouds using ISCCP data”, *J Climate*, **7(4)**, 465-497

Han, Q., Rossow, W. B., Chou, J., Kuo, K. S., Welch, R. M. (1999): “The effects of aspect ratio and surface roughness on satellite retrievals of ice-cloud properties”, *J. Quant. Spectrosc. Ra.*, **63(2)**, 559-583

Hatzianastassiou, N., Matsoukas, C., Fotiadi, A., Pavlakis, K. G., Drakakis, E., Hatzidimitriou, D., & Vardavas, I. (2005): “Global distribution of Earth's surface shortwave radiation budget”, *Atmos. Chem. Phys.*, **5(10)**, 2847-2867.

Henderson, D. S., L’Ecuyer, T., Stephens, G., Partain, P., & Sekiguchi, M. (2013): “A multisensor perspective on the radiative impacts of clouds and aerosols”, *J. Appl. Meteorol.*, **52(4)**, 853-871.

Hess, M., Koepke, P., and Schult, I. (1998): “Optical properties of aerosols and clouds: The software package OPAC”, *Bull. Amer. Meteor. Soc.*, ***79*****(5)**, 831-844.

Hirano, J. and Matsumoto, J. (2011): “Secular and seasonal variations of winter monsoon weather patterns in Japan since the early 20th century”, *Int. J. Climatol.*, ***31*****(15)**, 2330-2337.

Hänel, G. (1976): “The properties of atmospheric aerosol particles as functions of the relative humidity at thermodynamic equilibrium with the surrounding moist air”, *Adv. Geophys.*, ***19*****,** 73-188.

Inness, A., Baier, F., Benedetti, A., Bouarar, I., Chabrillat, S., Clark, H., et al. (2013): “The MACC reanalysis: an 8 yr data set of atmospheric composition”, *Atmos. Chem. Phys.*, ***13***, 4073-4109.

Inoue, T. (1987): “A cloud type classification with NOAA 7 split−window measurements”, *J. Geophys. Res.-Atmos*, ***92*****(D4)**, 3991-4000.

Intrieri, J. M., Fairall, C. W., Shupe, M. D., Persson, P. O. G., Andreas, E. L., Guest, P. S., and Moritz, R. E. (2002a): “An annual cycle of Arctic surface cloud forcing at SHEBA”, *J. Geophys. Res.-Oceans*, **107(C10)**, SHE-13.

Intrieri, J. M., Shupe, M. D., Uttal, T., and McCarty, B. J. (2002b): “An annual cycle of Arctic cloud characteristics observed by radar and lidar at SHEBA”, *J. Geophys. Res.-Oceans*, **107(C10)**, SHE-5.

Intrieri, J. M. and Shupe, M. D. (2004): “Characteristics and radiative effects of diamond dust over the western Arctic Ocean region”, *J. Climate*, **17(15)**, 2953-2960.

Ishida, H., Hayasaka, T., Kajikawa, M., Kikuchi, K., Uyeda, H., Asuma, Y., and Inoue, Y. (1998): “Observations of liquid water, water vapor, and downward flux of infrared radiation in the Arctic region with a microwave radiometer and a pyrgeometer”, *Polar Meteorol. Glaciol.*, ***12***, 10-18.

IPCC (2007): “Summary for Policymakers. In: Climate Change 2007: The Physical Science Basis. Contribution of Working Group I to the Fourth Assessment Report of the Intergovernmental Panel on Climate Change [Solomon, S., D. Qin, M. Manning, Z. Chen, M. Marquis, K.B. Averyt, M.Tignor and H.L. Miller (eds.)]”, Cambridge University Press, Cambridge, United Kingdom and New York, NY, USA.

Iwashima, T., Yamamoto, R., and YAMAMOTO, R. (1993): “A statistical analysis of the extreme events: Long-term trend of heavy daily precipitation”, *J. Meteorol. Soc. Jpn.*, ***71*****(5)**, 637-640.

Jhun, J. G. and Lee, E. J. (2004): “A new East Asian winter monsoon index and associated characteristics of the winter monsoon”, *J. Climate*, ***17*****(4)**, 711-726.

Katsaros, K. B. and Devault, J. E. (1986): “On irradiance measurement errors at sea due to tilt of pyranometers”, *J. Atmos. Ocean. Tech.*, **3(4)**, 740-745.

Kawai, Y. and Kawamura, H. (2005): “Validation and improvement of satellite-derived surface solar radiation over the northwestern Pacific Ocean”, *J. Oceanogr.*, ***61*****(1)**, 79-8

Kay, J. E., L'Ecuyer, T., Gettelman, A., Stephens, G., and O'Dell, C. (2008): “The contribution of cloud and radiation anomalies to the 2007 Arctic sea ice extent minimum”, *Geophys. Res. Lett.*, **35(8)**.

Keeling, R. F., Piper, S. C., Bollenbacher, A. F., and Walker, S. J. (2009): “Atmospheric CO2 values (ppmv) derived from in situ air samples collected at Mauna Loa, Hawaii, USA”, *Scripps Institution of Oceanography (SIO), University of California, La Jolla, California USA*.

Kendall, M. G. (1948): “Rank correlation methods”.

Kiehl, J. T., Hack, J. J., Bonan, G. B., Boville, B. A., and Briegleb, B. P. (1996): “*Description of the NCAR Community Climate Model (CCM3)”, Technical Note*(No. PB--97-131528/XAB; NCAR/TN--420-STR). National Center for Atmospheric Research, Boulder, CO (United States). Climate and Global Dynamics Div..

Kiehl, J. T. and Trenberth, K. E. (1997) :”Earth's annual global mean energy budget”, *Bull. Amer. Meteor. Soc.*, **78(2)**, 197-208.

Kipp&Zonen (2006): “CGR4 Pyrgeometer Instruction Mannual”.

Kimoto, M. (2005): “Simulated change of the East Asian circulation under global warming scenario”, *Geophys. Res. Lett.*, ***32*(16)**.

Kimoto, M., Yasutomi, N., Yokoyama, C., and Emori, S. (2005): “Projected changes in precipitation characteristics around Japan under the global warming”, *Sola*, ***1***, 85-88.

King, J. C. (1996): “Longwave atmospheric radiation over Antarctica”, *Antarct. Sci.*, ***8*(01)**, 105-109.

Kubota, M., Iwabe, N., Cronin, M. F., and Tomita, H. (2008): “Surface heat fluxes from the NCEP/NCAR and NCEP/DOE reanalyses at the Kuroshio Extension Observatory buoy site”, *J. Geophys. Res.-Oceans*, ***113*(C2)**.

Kupfer, H., Herber, A., and König-Langlo, G. (2006): “Radiation Measurements and Synoptic Observations at Ny Aalesund, Svalbard”, *Reports on Polar Research, Alfred Wegener Institute for Polar and Marine Research, Bremerhaven*, *538*.

Lanconelli, C., Busetto, M., Dutton, E. G., König-Langlo, G., Maturilli, M., Sieger, R., et al. (2011): “Polar baseline surface radiation measurements during the International Polar Year 2007–2009”, *ESSD.*, **3(1)**, 1-8.

Lee, H. S., Hwang, I. H., Spinhirne, J. D., and Scott, V. S. (1997): “Micro pulse lidar for aerosol and cloud measurement”, *In Advances in Atmospheric Remote Sensing with Lidar (pp. 7-10)*. Springer Berlin Heidelberg.

Loeb, N. G., Kato, S., Su, W., Wong, T., Rose, F. G., Doelling, D. R., .et al. (2012): “Advances in understanding top-of-atmosphere radiation variability from satellite observations”, *Surv. Geophys.*, ***33*(3-4)**, 359-385.

Long, C. N. and Ackerman, T. P. (2000): “Identification of clear skies from broadband

pyranometer measurements and calculation of downwelling shortwave cloud effects", *J. Geophys. Res.-Atmos.*, **105(D12)**, 15609-15626.

Mace, G. G., Zhang, Q., Vaughan, M., Marchand, R., Stephens, G., Trepte, C., and Winker, D. (2009): "A description of hydrometeor layer occurrence statistics derived from the first year of merged Cloudsat and CALIPSO data", *J. Geophys. Res.-Atmos.*, **114(D8)**.

Mace, G. G. and Zhang, Q. (2014): "The CloudSat radar - lidar geometrical profile product (RL - GeoProf): Updates, improvements, and selected results", *J. Geophys. Res.-Atmos.*, **119(15)**, 9441-9462.

MacWhorter, M. A. and Weller, R. A. (1991): "Error in measurements of incoming shortwave radiation made from ships and buoys", *J. Atmos. Ocean. Tech.*, **8(1)**, 108-117.

Mann, H. B. (1945): "Nonparametric tests against trend", *Econometrica*, 245-259.

Marty, C., Philipona, R., Delamere, J., Dutton, E. G., Michalsky, J., Stamnes, K., et al. (2003): "Downward longwave irradiance uncertainty under arctic atmospheres: Measurements and modeling", *J. Geophys. Res.-Atmos.*, **108(D12)**.

Matsui, N., Long, C. N., Augustine, J., Halliwell, D., Uttal, T., Longenecker, D., et al. (2012): "Evaluation of Arctic broadband surface radiation measurements", *Atmos. Meas. Tech.*, **5**, 429-438.

McArthur, L. J. B. (2005): "World Climate Research Programme: Baseline Surface Radiation Network (BSRN) Operations Manual Version 2.1", *WCRO-121*, **WNI/TD-No.1274**.

Medovaya, M., Waliser, D. E., Weller, R. A. and McPhaden, M. J. (2002): "Assessing ocean buoy shortwave observations using clear−sky model calculations", *J. Geophys. Res.-Oceans*, ***107*(C2)**, 6-1.

Meloni, D., Di Biagio, C., Di Sarra, A., Monteleone, F., Pace, G., and Sferlazzo, D. M. (2012): "Accounting for the solar radiation Influence on downward longwave irradiance measurements by pyrgeometers", *J. Atmos. Ocean. Tech.*, **29(11)**, 1629-1643.

Michalsky, J., Dutton, E., Rubes, M., Nelson, D., Stoffel, T., Wesley, M., et al. (1999): "Optimal measurement of surface shortwave irradiance using current instrumentation", *J. Atmos. Ocean. Tech.*,**16(1)**, 55-69.

Morimoto, S., Nakazawa, T., Aoki, S., Hashida, G., and Yamanouchi, T. (2003): "Concentration variations of atmospheric CO2 observed at Syowa Station, Antarctica from 1984 to 2000", *Tellus B*, ***55*(2)**, 170-177.

Morimoto, S., Aoki, S., Nakazawa, T., and Yamanouchi, T. (2006): “Temporal variations of the carbon isotopic ratio of atmospheric methane observed at Ny Ålesund, Svalbard from 1996 to 2004”, *Geophys. Res. Lett.*, ***33*****(1)**.

Nakajima, T. and Tanaka, M. (1986): “Matrix formulations for the transfer of solar radiation in a plane-parallel scattering atmosphere”, *J. Quant. Spectrosc. Radiat. Transf.*, ***35*****(1)**, 13-21.

Nakajima, T. and Tanaka, M. (1988): “Algorithms for radiative intensity calculations in moderately thick atmospheres using a truncation approximation”, *J. Quant. Spectrosc. Radiat. Transf.*, ***40*****(1)**, 51-69.

Nakazawa, T., Aoki, S., Murayama, S., Fukabori, M., Yamanouchi, T., Murayama, H., et al. (1991): “The concentration of atmospheric carbon dioxide at the Japanese Antarctic Station, Syowa”, *Tellus B*, ***43*****(2)**, 126-135.

Nast, P. M. (1983): “Measurements on the accuracy of pyranometers”, *Sol. Energy*, ***31*****(3)**, 279-282.

Niu, X., Pinker, R. T., and Cronin, M. F. (2010): “Radiative fluxes at high latitudes”, *Geophys. Res. Lett.*, ***37*****(20)**.

Ohmura, A., Gilgen, H. J., and Wild, M. (1989): “*Global Energy Balance Archive”, GEBA*. Verlag der Fachvereine; Geographisches Institut, Eidgenössische Technische Hochschule Zürich.

Ohmura, A., Gilgen, H., Hegner, H., Müller, G., Wild, M., Dutton, E. G., et al. (1998): “Baseline Surface Radiation Network (BSRN/WCRP): New precision radiometry for climate research”, *Bull. Amer. Meteor. Soc.*, ***79*****(10)**, 2115-2136.

Ohtake, Takeshi, K. O. L. F. Jayaweera, and Ken-Ichi Sakurai. (1982): “Observation of ice crystal formation in lower Arctic atmosphere”, *J. Atmos. Sci.*, **39.12**, 2898-2904.

Onogi, K., Tsutsui, J., Koide, H., Sakamoto, M., Kobayashi, S., Hatsushika, H., et al. (2007): “The JRA-25 reanalysis”, *J. Meteorol. Soc. Jpn.*, **2**, 85(3), 369-432

Pascal, R. W. and Josey, S. A. (2000): “Accurate Radiometric Measurement of the Atmospheric Longwave Flux at theSea Surface”, *J. Atmos. Ocean. Tech.*, ***17*****(9)**, 1271-1282.

Payne, R. E. (2004): “An all-thermistor pyrgeometer”, Woods Hole Oceanographic Institution.

Pérez, M. and Alados-Arboledas, L. (1999): “Effects of natural ventilation and solar radiation on the performance of pyrgeometers”, *J. Atmos. Ocean. Tech.*, ***16*****(1)**, 174-180.

Philipona, R., Fröhlich, C., and Betz, C. (1995): “Characterization of pyrgeometers and the accuracy of atmospheric long-wave radiation measurements”, *Applied Optics*, ***34*****(9)**, 1598-1605.

Philipona, R., Dutton, E. G., Stoffel, T., Michalsky, J., Reda, I., Stifter, A., et al. (2001):

"Atmospheric longwave irradiance uncertainty - Pyrgeometers compared to an absolute sky-scanning radiometer, atmospheric emitted radiance interferometer, and radiative transfer model calculations", *J. Geophys. Res.-Atmos.*, **106**, 28.

Philipona, R., Dürr, B., and Marty, C. (2004): "Greenhouse effect and altitude gradients over the Alps–by surface longwave radiation measurements and model calculated LOR", *Theor. Appl. Climatol.*, **77(1-2)**, 1-7.

Phillpot, H. R. and Zillman, J. W. (1970): "The surface temperature inversion over the Antarctic continent", *J. Geophys. Res.*, ***75*(21)**, 4161-4169.

Pinker, R. T., Wang, H., and Grodsky, S. A. (2009): "How good are ocean buoy observations of radiative fluxes?", *Geophys. Res. Lett.*, ***36*(10)**.

Prata, F. (2008): "The climatological record of clear-sky longwave radiation at the Earth's surface: evidence for water vapour feedback?", *Int. J. Remote. Sens.*, **29**, 5247-5263.

Raddatz, R. L., Galley, R. J., Candlish, L. M., Asplin, M. G., and Barber, D. G. (2013): "Water vapour over the western maritime Arctic: Surface inversions, intrusions and total column", *Int. J. Climatol.*, **33(6)**, 1436-1443.

Redler, R., Valcke, S., and Ritzdorf, H. (2010): "OASIS4–a coupling software for next generation earth system modelling", *Geosci. Model Dev.*, ***3*(1)**, 87-104.

Rossow, W. B. and Zhang, Y. C. (1995): "Calculation of surface and top of atmosphere radiative fluxes from physical quantities based on ISCCP data sets: 2. Validation and first results", *J. Geohys. Res.*, **100(D1)**, 1167-1197

Schanz, L. C. and Schlüssel, P. (1997): "Atmospheric back radiation in the tropical pacific: Intercomparison of in-situ measurements, simulations and satellite retrievals", *Meteorol. Atmos. Phys.*, ***63*(3-4)**, 217-226.

Schmidt, G. A., Ruedy, R. A., Miller, R. L., and Lacis, A. A. (2010): "Attribution of the present day total greenhouse effect", *J. Geophys. Res.-Atmos.*, ***115*(D20)**.

Sekiguchi, M. and Nakajima, T. (2008): "A k-distribution-based radiation code and its computational optimization for an atmospheric general circulation model", *J. Quant. Spectrosc. Radiat. Transfer*, ***109*(17)**, 2779-2793.

Serra, Y. L., A'hearn, P., Freitag, H. P., and McPhaden, M. J. (2001): "ATLAS Self-Siphoning Rain Gauge Error Estimates", *J. Atmos. Ocean. Tech.*, ***18*(12)**, 1989-2002.

Shimizu, A., Sugimoto, N, and Matsui, I, (2010): "Detailed Description of Data Processing System for Lidar Network in East Asia", *25th International Laser Radar Conference*, St. Petersburg, Russia, 911-913.

Shiobara, M., Yabuki, M., and Kobayashi, H.. (2003): “A polar cloud analysis based on Micro-pulse Lidar measurements at Ny-Alesund, Svalbard and Syowa, Antarctica”, *Phys. Chem. Earth*, **28**, 1205-1212.

Shupe, M. D. and Intrieri, J. M. (2004): “Cloud radiative forcing of the Arctic surface: The influence of cloud properties, surface albedo, and solar zenith angle”, *J. Climate*, ***17*(3)**, 616-628.

Solomon, S., D. Qin, M. Manning, M., Marquis, K. Averyt, M. M. B. Tignor, H. L. Miller, Jr., and Z. Chen (2007): “Climate Change 2007 The Physical Science Basis Frequently Asked Questions and Selected Technical Summary Boxes”, *Part of the Working Group 1 contribution to the Fourth Assessment Report of the Intergovernmental Panel on Climate Change.*

Spinhirne, James D. (1993): “Micro pulse lidar”, *IEEE Trans. Geosci. Remote Sens.,* **31.1**, 48-55.

Steig, E. J., Schneider, D. P., Rutherford, S. D., Mann, M. E., Comiso, J. C., and Shindell, D. T. (2009): “Warming of the Antarctic ice-sheet surface since the 1957 International Geophysical Year”, *Nature*, **457(7228)**, 459-462.

Stephens, G. L., Wild, M., Stackhouse Jr, P. W., L'Ecuyer, T., Kato, S., and Henderson, D. S. (2012): “The global character of the flux of downward longwave radiation”, *J. Climate*, ***25*(7)**, 2329-2340.

Stone, R. S. (1993): “Properties of austral winter clouds derived from radiometric profiles at the South Pole”, *J. Geophys. Res.-Atmos.*, ***98*(D7)**, 12961-12971.

Su, W., Dutton, E., Charlock, T. P., and Wiscombe, W. (2008): “Performance of commercial radiometers in very low temperature and pressure environments typical of polar regions and of the stratosphere: A laboratory study”, *J. Atmos. Ocean. Tech.*, ***25*(4)**, 558-569.

Sugi, M. (1990): “Description and performance of the JMA operational global spectral model (JMA-GSM88)”, *Geophys. Mag.*, **43**, 105-130

Swinbank, W. C. (1963): “Longwave radiation from clear skies”, *Q. J. Roy. Meteor. Soc.*, ***89*(381)**, 339-348.

Tanahashi, S., Kawamura, H., Matsuura, T., Takahashi, T., and Yusa, H. (2001): “A system to distribute satellite incident solar radiation in real-time”, *Remote Sens. Environ.*, ***75*(3)**, 412-422.

Trenberth, K. E., Fasullo, J. T., and Kiehl, J. (2009): “Earth's global energy budget”, *Bull. Amer. Meteor. Soc.*, **90(3)**, 311-323.

Thompson, D. W. and Solomon, S. (2002): “Interpretation of recent Southern Hemisphere climate change”, *Science*, ***296*****(5569)**, 895-899.

Town, M. S., V. P. Walden, and S. G. Warren (2005): “Spectral and Broadband Longwave Downwelling Radiative Fluxes Radiative Fluxes, Cloud Radiative Forcing, and Fractional Cloud Cover over the South Pole”, *J. Climate.*, **18**, 4235-4252.

Turner, J., Colwell, S. R., Marshall, G. J., Lachlan-Cope, T. A., Carleton, A. M., Jones, P. D., et al. (2005): “Antarctic climate change during the last 50 years”, *Int. J. Climatol.*, **25(3)**, 279-294.

Udo, S. O. (2000): “Quantification of solar heating of the dome of a pyrgeometer for a tropical location: Ilorin, Nigeria”, *J. Atmos. Ocean. Tech.*, **17(7)**, 995-1000.

Waliser, D. E., Weller, R. A., and Cess, R. D. (1999): “Comparisons between buoy - observed, satellite - derived, and modeled surface shortwave flux over the subtropical North Atlantic during the Subduction Experiment”, *J. Geophys. Res.-Atmos.*, **104(D24)**, 31301-31320.

WANG, B., and HO, L. (2002): “Rainy season of the Asian-Pacific summer monsoon”, *J. Climate*, ***15*****(4)**, 386-398.

Wang, J., and Rossow, W. B. (1995): “Determination of cloud vertical structure from upper-air observations”, *J. Appl. Meteorol.*, **34(10)**, 2243-2258.

Wang, K. C. and S. L. Liang (2009): “Global atmospheric downward longwave radiation over land surface under all-sky 15 conditions from 1973 to 2008”, *J. Geophys. Res.*, **114**, D19101.

Wang, H. and Pinker, R. T. (2009): “Shortwave radiative fluxes from MODIS: Model development and implementation”, *J. Geophys. Res.-Atmos.*, ***114*****(D20)**.

Wang, K. and Dickinson, R. E. (2013): “Global atmospheric downward longwave radiation at the surface from ground−based observations, satellite retrievals, and reanalyses”, *Reviews of Geophysics*, ***51*****(2)**, 150-185.

Welton, E. J., and Campbell, J. R. (2002): “Micropulse lidar signals: Uncertainty analysis”, *J. Atmos. Ocean. Tech.*, ***19*****(12)**, 2089-2094.

Wild, M., Grieser, J., and Schär, C. (2008): “Combined surface solar brightening and increasing greenhouse effect support recent intensification of the global land−based hydrological cycle”, *Geophys. Res. Lett.*, **35(17)**.

Wild, M., Folini, D., Schär, C., Loeb, N., Dutton, E. G., and König-Langlo, G. (2013): “The global energy balance from a surface perspective”, *Clim. Dynam.*, **40(11-12)**, 3107-3134.

Winker, D. M., Pelon, J., Coakley Jr, J. A., Ackerman, S. A., Charlson, R. J., Colarco, P. R., et al. (2010): “The CALIPSO mission: A global 3D view of aerosols and clouds”.

Yabuki, M., Shiobara, M., Nishinaka, K., and Kuji, M. (2014): “Development of a cloud detection

method from whole-sky color images", *Polar Sci.*, **8(4)**, 315-326.

Yamada, K., Hayasaka, T., and Iwabuchi, H. (2014): "Variation in Radiative Contribution by Clouds to Downward Longwave Flux", *J. Meteorol. Soc. Jpn.*, ***92*(0)**, 125-140.

Yamada, K. and Hayasaka, T. (2016): "Evaluation of the accuracy of downward radiative flux observations at the sea surface", *J. Oceanogr.*, 1-13.

Yamamoto, G. (1952): "On the Radiation Chart".

Yamamoto, G. and T. Sasamori (1954): "Measurement of Atmospheric Radiation", *Sci. Rep. Tohoku Univ. Ser. 5, Geophys.*, **6**, 19−31.

Yamanouchi, T. and Kawaguchi, S. (1984): "Longwave radiation balance under a strong surface inversion in the katabatic wind zone, Antarctica", *J. Geophys. Res.-Atmos.*, **89(D7)**, 11771-11778.

Zhang, Y., Rossow, W. B., Lacis, A. A., Oinas, V., and Mishchenko, M. I. (2004): "Calculation of radiative fluxes from the surface to top of atmosphere based on ISCCP and other global data sets: Refinements of the radiative transfer model and the input data", *J. Geophys. Res.-Atmos.*, **109(D19)**.